TESIS DE LA UNIVERSIDAD
DE ZARAGOZA
2015
62

Fabián Riveros Moyano

Passive biomechanics of abdominal aortic aneurysms

Departamento
Ingeniería Mecánica

Director/es
Rodríguez Matas, José Félix

http://zaguan.unizar.es/collection/Tesis

ISSN 2254-7606

Prensas de la Universidad
Universidad Zaragoza

© Universidad de Zaragoza
Servicio de Publicaciones

ISSN 2254-7606

Tesis Doctoral

PASSIVE BIOMECHANICS OF ABDOMINAL AORTIC ANEURYSMS

Autor

Fabián Riveros Moyano

Director/es

Rodríguez Matas, José Félix

UNIVERSIDAD DE ZARAGOZA
Ingeniería Mecánica

2015

Repositorio de la Universidad de Zaragoza – Zaguan http://zaguan.unizar.es

Universidad
Zaragoza
1542

TESIS DOCTORAL

Passive biomechanics of Abdominal Aortic Aneurysms

Autor

Fabián Riveros Moyano

Director

José Félix Rodríguez Matas

Posgrado en Ingeniería Mecánica y de Materiales
Doctorado en Mecánica Computacional
2015

ABSTRACT

The passive biomechanics of abdominal aortic aneurysms (AAA) is studied, seeking to deepen in its knowledge and with the aim of providing better decision criteria to undergo surgical intervention for AAA repair.

Biomechanical parameters as the peak wall stress (PWS) or the peak wall rupture risk (PWRR) have shown to be a feasible and promising alternative that can be used to better ascertain the risk of rupture. In addition, the understanding of the passive biomechanics of AAA allows obtaining a more accurate stress assessment, which can be done by using appropriate material models for the tissues along with accurate geometric models and more realistic boundary conditions for the lesion.

This thesis presents a novel iterative algorithm to determine the zero-pressure geometry of a patient-specific AAA that overcomes limitations on existing methodologies and allows a better estimation of the stresses. The importance of this algorithm lays in that patient-specific AAA models are generated from gated CT (Computer Tomography) medical images in which the artery is under pressure (diastolic), therefore the identification of the AAA zero pressure geometry would allow for a more realistic estimate of the aneurysmal wall mechanics. The methodology allows considering the anisotropic hyperelastic behavior of the aortic wall, its thickness and accounts for the presence of the intraluminal thrombus (ILT). The results on twelve patient-specific AAA geometric models indicate that the procedure is computational tractable and efficient, and preserves the global volume of the model. In addition, a comparison of the peak wall stress computed with the zero pressure and CT-based geometries during systole indicate that computations using CT-based geometric models underestimate (significantly) the peak wall stress for both, isotropic and anisotropic material models of the arterial wall. In addition, based on the reported experimental results for aneurysmal and aortic wall mechanics, no significant differences among isotropic and anisotropic material models have been found.

With respect to the ILT, which is a pseudo-tissue that develops from coagulated blood and it is found in most AAAs of clinically relevant size, a number of studies have suggested that ILT mechanical characteristics may be related to AAA risk of rupture, even though there is still great controversy on this regard. This thesis investigates how ILT constitution and topology influence the magnitude and location of PWS. ILT is isotropic and inhomogeneous and may appear as a soft (single-layered) or stiff (multilayered fibrotic) tissue. An extended study was conducted involving twenty-one patient-specific AAAs (diameter: 4.2-5.4 cm) which were reconstructed from CT images and biomechanically analyzed using the proposed methodology. Results indicated that PWS correlated stronger with ILT volume ($\rho=0.44$, $p=0.05$) and the minimum thickness of the ILT layer ($\rho=0.73$, $p=0.001$) than with maximum AAA diameter ($\rho=0.05$, $p=0.82$). In average PWS was 20% (SD 12%) higher for FE models that used a soft instead of stiff ILT models ($p<0.001$). PWS location strongly correlated with sites of minimum ILT thickness in the section of maximum AAA diameter and was independent from the ILT stiffness. In addition, ILT heterogeneity, i.e. the spatial composition of soft and stiff thrombus tissue, can considerably influence the stress in the AAA wall.

The present study is limited to the identification of influential biomechanical factors, and how its findings translate to an AAA rupture risk assessment remains to be explored by clinical studies.

RESUMEN

En esta tesis se estudia la respuesta elástica de aneurismas aórticos abdominales (AAA), buscando ahondar en su conocimiento y con la finalidad de proveer un mejor criterio de decisión para la realización, o no, de una intervención quirúrgica para la reparación de la lesión.

Parámetros biomecánicos como la tensión pico de la pared arterial (singlas en inglés: PWS) o el riesgo de ruptura de la pared arterial (siglas en inglés: PWRR) han mostrado ser una alternativa posible y prometedora a ser utilizada para determinar el riesgo de ruptura. De la misma manera, el entender la biomecánica pasiva de los AAA permite realizar una evaluación más correcta de las tensiones, lo que se puede realizar mediante el uso de modelos de material adecuados para los tejidos junto con modelos geométricos fiables en los que se apliquen condiciones de frontera realistas.

Esta tesis presenta un novedoso algoritmo iterativo para determinar la geometría cero-presión de un AAA para pacientes específicos, la cual supera las limitaciones de las metodologías existentes y permite una mejor estimación de las tensiones. La importancia de este algoritmo se debe a que los modelos de AAA de pacientes específicos son generados a partir de imágenes médicas de CT (tomografía axial computarizada) sincronizadas en las cuales la arteria está bajo presión, por lo tanto la identificación de la geometría cero-presión de AAAs permite una estimación más realista de la respuesta mecánica de la pared arterial. La metodología permite considerar el comportamiento hiperelástico anisótropo de la pared arterial, su espesor y la presencia del trombo intraluminal (ILT). Resultados en doce geometrías de de AAAs, paciente específico, indican que el algorítmo es computacionalmente tratable y eficiente, a la vez que preserva el volumen global del modelo. Adicionalmente, una comparación de resultados de PWS calculados usando geometría cero-presión y geometría basada en CT al aplicar la presión sistólica indica que los resultados a partir de geometría CT subestiman (significativamente) la tensión pico de la pared arterial en casos de modelos isótropo y anisótropo de la pared arterial. Adicionalmente, en base a los resultados experimentales publicados para la pared arterial del aneurisma y aorta sana, los resutados de esta tesis no

encuentran diferencias significativas entre el uso de un modelo de material isótropo o anisótropo.

Con respecto al ILT, el cual es un pseudo-tejido que se desarrolla a partir de sangre coagulada y se encuentra en la mayor parte de los AAAs de tamaño relevante, algunos estudios sugieren que las características mecánicas del ILT pueden estar relacionadas con el riesgo de ruptura del AAA, aunque existe una gran controversia en este respecto. Esta tesis investiga como la constitución y topología del ILT influye en la magnitud y localización de las tensiones pico en la pared arterial. El ILT, isótropo y no homogéneo, puede aparecer como un tejido flexible (una capa) o rígido (fibrótico multicapa). El estudio se extendió a 21 AAAs, pacientes específicos, (diámetro: 4.2-5.4 cm) que fueron reconstruidos a partir de imágenes CT y analizados numéricamente empleando el algoritmo de tirón propuesto para identificar la geometría cero presión. Los resultados indican que la PWS está mayormente correlacionada con el volumen de ILT ($\rho=0.44$, $p=0.05$) y con el espesor de capa mínimo de ILT ($\rho=0.73$, $p=0.001$) que con el diámetro máximo de AAA ($\rho=0.05$, $p=0.82$). En promedio la PWS fue un 20% (desv estándar 12%) más alta para modelos en los que se usaron modelos suaves de ILT en lugar de modelos rígidos de ILT ($p<0.001$). La localización del PWS está altamente correlacionada con los puntos de menor espesor de ILT, en las secciones de máximo diámetro del AAA, y esto fue independiente de la rigidez del ILT. Adicionalmente, la heterogeneidad del ILT, i.e. la composición espacial de trombo suave o rígido, puede influenciar sustancialmente la tensión de la pared arterial.

El presente estudio está limitado a identificar la influencia de factores biomecánicos, el cómo estos resultados se trasladan a la evaluación del riesgo de ruptura de AAA debe ser desarrollado a partir de estudios clínicos.

ACKNOWLEDGMENTS

I would like to extend my deepest gratitude to my doctoral advisor, Dr Jose Felix Rodriguez. Thank you for guiding me, for expending long hours of your time in helping me understand complicated mathematics and physics, advising me in programing, worrying about my professional and personal development and helping bring out the best in me during the four years of this investigation. I have enjoyed learning and expanding my mind and knowledge with you.

Thanks to Dr Christian Gasser from the Royal Institute of Technology (KTH) who collaborated with us when the findings of this investigation were published in international journals. He provided us with AAA models and advised us on how to focus this investigation.

To my wife Marcela who supported and encouraged me although I had to work during many weekends and late nights. Not wrongly you nick-named me “The Calculator”. I love you.

I dedicate this manuscript to the memory of my parents, every day I wish you were here and especially on the days of such great achievements in my life. Also to the memory of my grandmother who until our last conversation cared about how my PhD was progressing, well, it´s done.

TABLE OF CONTENTS

1. INTRODUCTION 19
  1.1. DEMOGRAPHICS 20
  1.2. BIOLOGICAL FACTORS 21
    1.2.1. Proteolytic degradation of the AAA wall 22
    1.2.2. Matrix-Metallo-Proteinases (MMPs) 22
    1.2.3. Tissue Inhibitors of Metalloproteinases (TIMP) 23
    1.2.4. Macrophage and lymphocyte presence 23
    1.2.5. Reactive Oxigen Species (ROS) 24
    1.2.6. C-Reactive Proteine (CPR) 25
    1.2.7. Genetic Aspects 25
    1.2.8. Miscellaneous factors 26
  1.3. GEOMETRIC FACTORS 27
    1.3.1. Maximum diameter 27
    1.3.2. Shape Effect 28
    1.3.3. Presence of Intra-luminal thrombus 29
    1.3.4. Wall thickness 29
    1.3.5. Geometry and Peak Wall Stress 30
  1.4. BIOMECHANICAL FACTORS 33
    1.4.1. Effect of blood flow 34
  1.5. Objectives 37
2. MECHANICAL BEHAVIOR OF THE AAA TISSUES 41
  2.1. Arterial Tissue 41
  2.2. Intraluminal Thrombus 47
3. PATIENT SPECIFIC AAA FINITE ELEMENT MODELS GENERATION 53
  3.1. AAA Models Generation 53
    3.1.1. Surfaces Preparation 54
    3.1.2. Meshing 55
    3.1.3. Labeling 56
    3.1.4. FEM model generation 57
    3.1.5. Direction of ansiotropy 58
  3.2. Material Model Implementation 59
  3.3. Mesh sensitivity analysis 59
4. PULLBACK ALGORITHM 63
  4.1. Zero-pressure geometry algorithm 65
  4.2. Computational Validation 66
    4.2.1. Cylindrical tube 67
    4.2.2. Patient specific AAA geometry 68
    4.2.3. Arterial wall only 69
    4.2.4. Whole model 71
  4.3. Experimental Validation 72
    4.3.1. Material & Methods 73
    4.3.2. Results 75
5. EFFECT OF THE ZERO PRESSURE GEOMETRY ON THE AAA RUPTURE RISK 79
  5.1. Methods 79

        - 5.1.1. Patient specific models 79
        - 5.1.2. Material model and boundary conditions 80
        - 5.1.3. Statistical analysis 82
    - 5.2. Results 82
    - 5.3. Discussion 87
    - 5.4. Conclusions 90
- 6. On the impact of Intraluminal Thrombus mechanical behavior in AAA passive mechanics 95
    - 6.1. Material Models 96
        - 6.1.1. Patient specific models 96
        - 6.1.2. Material models 98
        - 6.1.3. Finite element simulations 98
        - 6.1.4. Statistical analysis 99
    - 6.2. Results 99
    - 6.3. Discussion 109
- 7. CONCLUSION 115
- 8. APPENDIX A 125
- 9. APPENDIX B 139
- 10. APPENDIX C 153
- 11. APPENDIX D 163
- 12. APPENDIX E 169
- 13. REFERENCES 175

LIST OF FIGURES

Figure 1. Abdominal Aortic Aneurysm 19
Figure 2. Localized stresses, fragmented medial proteins, and genetic predisposition, likely attract inflammatory cells into the aortic wall. Released chemokines, cytokines, and reactive oxygen species by these inflammatory cells, results in further influx of leukocytes, and further medial degradation (Ailawadi, 2003). 24
Figure 3. Estimated wall thickness distribution (in mm) in a point cloud resulting from a segmented CT dataset (Shum J. E., 2010). 30
Figure 4. (a) 1-D size indices: maximum diameter (D_{max}), proximal neck diameter ($D_{neck,p}$), distal neck diameter ($D_{neck,d}$), sac height (H_{sac}), neck height (H_{neck}), sac length (L_{sac}), neck length (L_{neck}), bulge height (H_b); (b) 1-D size index: centroid distance at the maximum diameter (dc). 31
Figure 5. Schematic of 2D shape indices providing an approximate measure to construe the global AAA shape: diameter to height ratio (DHr), diameter to diameter ratio (DDr), height ratio (Hr), bulge location (BL), asymmetry (β), and tortuosity (T). 32
Figure 6. Maximum and average principal stress and strain waveforms for a patient-specific AAA obtained using direct FSI, uncouple FSI and transient FEA. The stress and strain follow the inlet velocity waveform rather than the pressure waveform boundary condition. 36
Figure 7. Diagrammatic model of the major components of a healthy elastic artery composed by three layers: Intima, Media and Adventitia (Holzapfel G.A, 2000) 41
Figure 8. Circumferential direction of anisotropy in an AAA 44
Figure 9. Biaxial experimental data from vande Geest et al. (Vande Geest J. P., 2006) versus predicted results by the isotropic SEF Eq. (5) in the (a) circumferential and (b) longitudinal directions. 46
Figure 10. Biaxial experimental data from vande Geest et al. (Vande Geest J. P., 2006) versus predicted results by the anisotropic SEF Eq. (6) in the (a) circumferential and (b) longitudinal directions. 46
Figure 11. Intraluminal thrombus (ILT) 47
Figure 12. Cauchy stress versus stretch curves for the ILT material models considered in the study 49
Figure 13. Comparison of luminal ILT’s elastic behavior under uniaxial elongation according to two different constitutive models characterized using uniaxial test data (Gasser T. C., 2008) and biaxial test data (Vande Geest J. P., 2006). 50
Figure 14. Internal, external and lumen surfaces of an AAA 3D model 54
Figure 15. Surfaces modelling in Rhinoceros 3D. (a) Planes to cut the surfaces (b) upper cover between external and internal surfaces (c) lower cover between external and internal surfaces for each of the iliac bifurcations 55
Figure 16. Lines extracted from the areas. (a) Geometry in ANSYS-ICEM (b) extracted lines from top cover 55
Figure 17. Mesh setup in ANSYS-ICEM 56
Figure 18. Labeled AAA mesh in ABAQUS 57
Figure 19. Displacement restraints applied to AAA models. (a) Axial displacement restriction (b) restrictions to allow radial displacement 58

Figure 20. Circumferential direction on two typical AAA models. Circumferential directions were obtained according to the procedure proposed in Alastrue et al (Alastrué, 2006.). 59
Figure 21. Finite element meshes for a typical AAA model (inset shows a detail of the wall mesh). 60
Figure 22. ZP and CT based configuration of an AAA with ILT 63
Figure 23. Zero-pressure geometry algorithm. The algorithm continuously updates the reference configuration of the AAA until the difference between the original CT-image and the deformed configuration obtained from the current zero-pressure geometry, $\mathbf{X}defk$, is less than a prescribed tolerance, *tol*. 65
Figure 24. Idealized geometry used to validate the algorithm to compute the zero-pressure geometry. The cylinder in green corresponds to the pressurized geometry used as input information to compute the zero-pressure geometry. The wireframe corresponds to the zero-pressure geometry identified by the algorithm. 67
Figure 25. Convergence plot for the idealized geometry. The algorithm takes five iterations to reach the required tolerance (0.1%). Already, after the second iteration the error is less than 0.2%. 68
Figure 26. Typical AAA model: Geometry and ILT distribution 69
Figure 27. Convergence of the Pull-Back algorithm for the AAA model without the ILT. Maximum and mean nodal distance between the identified and the actual ZP configuration. 69
Figure 28. Evolution of the zero pressure configuration for the AAA model without the ILT. 70
Figure 29. Convergence of the element with maximum error for the AAA model without the ILT. 70
Figure 30. Convergence of the Pull-Back algorithm for the AAA model (whole model): a) Maximum and mean nodal distance between the identified and the actual ZP configuration; b) Evolution of the zero pressure configuration for the AAA model (whole model). 71
Figure 31. Convergence of the element with maximum error for the AAA model (whole model). 72
Figure 32. a) Phantom replica of AAA; b) Schematic diagram of experimental setup for zero pressure algorithm validation; c) Image based computational geometry of AAA phantom with hexahedral mesh used for structural simulations. 73
Figure 33. a) Convergence of ZP algorithm applied to phantom geometries pressurized at 80, 120 and 140 mmHg; b) front view and c) right view of superimposed lumen surfaces of ZP geometry/80mmHg and Phantom@0mmHg; d) spatial distribution of nodal distances between the two surfaces (red represents maximum distance). 75
Figure 34. ZP and CT based configuration of an AAA with ILT for models A1, B2, B7 and B9 models. 82
Figure 35. Maximum principal stress for model B1 (in kPa). (a) Isotropic model based on the CT-based geometry; (b) Anisotropic model based on the CT-based geometry; (c) Isotropic model based on the zero-pressure geometry; (d) Anisotropic model based on the zero-pressure geometry. 83
Figure 36. Predicted peak principal stresses (PWS) in the AAA wall. Results use the CT-based (striped bars) and the zero-pressure (grey bars)

geometries for their stress-free reference configurations. Predictions are based on an isotropic (a) and anisotropic (b) constitutive descriptions of the AAA wall. 84
Figure 37. Peak principal stresses (PWS) in the wall compared to the diameter of AAAs Predictions considered an anisotropic constitutive model for the AAA wall and the zero-pressure geometry as their stress-free reference configuration. The trend line shows a slight increase in the PWS with the maximum AAA diameter. 85
Figure 38. Cross-sections, where the peak principal stress (PWS) in the wall was predicted. Color-coded principal stresses plot (left) and segmented tissues with the ILT in red and the arterial wall in blue (right) are shown. Predictions considered an anisotropic constitutive model for the AAA wall and the zero-pressure geometry as their stress-free reference configuration. 86
Figure 39. Convergence of the algorithm to predict the AAA zero-pressure geometry. Model A2 is considered and the computation used isotropic (circles) and anisotropic (squares) constitutive models for the AAA wall. 87
Figure 40. a) Predicted peak principal stresses in the AAA wall; b) Predicted average principal wall stress in the wall. Results use the zero pressure geometries for their stress-free reference configurations. Predictions are for the type A ILT (light grey bars) and for the type B ILT (dark grey bars). 100
Figure 41. Predicted average von Mises stress in the ILT. Results use the zero pressure geometries for their stress-free reference configurations. Predictions are for the type A ILT (light grey bars) and for the type B ILT (dark grey bars). 101
Figure 42. Predicted maximum principal wall stress (panels a and b) and average maximum principal wall stress (panels c and d) in the AAA wall for both types of ILT material compare to the maximum AAA diameter (panels a and c), and the ILT volume (panels b and d). Results use the zero pressure geometries for their stress-free reference configurations. The trend line shows a slight increase of the PWS with AAA maximum diameter, where as PWS shows a tendency to decrease with ILT volume. The observed tendency is the same for both ILT types. 102
Figure 43. Predicted maximum stress ratio in the AAA wall covered by the ILT due to the presence of the ILT. Predictions are for the type A ILT (light grey bars) and for the type B ILT (dark grey bars). The inset shows the stress ratio profile for model 1. The maximum stress ratio located in the area of maximum ILT thickness. 103
Figure 44. Stress field in the AAA models with asymmetric ILT. The PWS was always located in the side where ILT thickness is minimum. Results correspond to type A ILT. 104
Figure 45. Peak Wall Stress for both ILT types. a) As a function of minimum ILT thickness; b) As a function of the local lumen diameter to wall thickness plus minimum ILT thickness ratio. 105
Figure 46. Average stress for a hypothetical heterogeneous ILT. Heterogeneity is represented as volume percentage of Type A ILT tissue (section in dark grey in the top panel). a) Mean stress in the arterial wall (solid line with solid diamonds) and ILT (solid line with solid squares); b) Mean stress in the ILT (solid line with solid squares) and in the individual ILT components:

Type B ILT (solid line with solid circles) and Type A ILT (solid line with solid triangles). 106
Figure 47. Average stress of Aneurismal Wall for hypothetical heterogeneous ILT for 7 different AAA models. 107
Figure 48. Average stress of the ILT for hypothetical heterogeneous ILT for 7 different AAA models. 108
Figure 49. Average stress of Type A and Type A for hypothetical heterogeneous ILT for 7 different AAA models. 108

LIST OF TABLES

Table 1. Patient demographical data from a random sampling in the US (Huber, 2001) 21

Table 2. Material parameters for the isotropic, Eq. (5), and anisotropic, Eq. (6), aneurysmal wall tissue constitutive models. 45

Table 3. Predicted peak principal stress (PWS) in the AAA wall for the model. Results for different meshes are shown, where NE denotes the number of elements. Change in PWS, $\Delta\mathbf{PWS}$, is computed between two consecutive mesh densities. 59

Table 4. Percentage volume change between the zero pressure and CT-based geometries. 72

Table 5. Characteristics of the twelve patient-specific AAA models. 81

Table 6. Characteristics of AAA models for Intraluminal Thrombus mechanical behavior study. 97

INTRODUCTION

SARAVGVSTANAE ✝ ST
S

1. INTRODUCTION

An abdominal aortic aneurysm (AAA) is an abnormal widening of the aorta, commonly developed below the renal arteries and above the iliac bifurcations as shown in Figure 1. The natural course of aneurysm disease is a progressive aortic enlargement combined with weakening of the wall tissue that may result in aortic rupture (Sakalihasan et al., 2005).

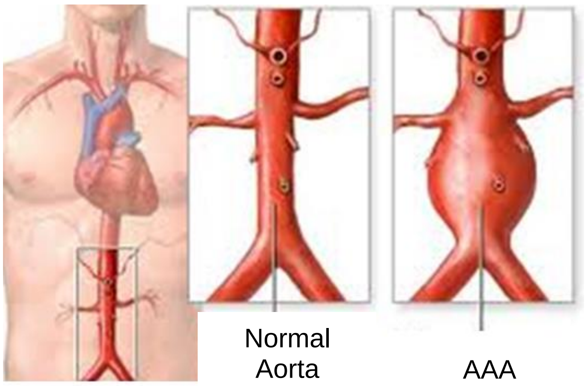

Figure 1. Abdominal Aortic Aneurysm

The underlying cause for the formation of an aneurysm can be either inherited (i.e., Marfan syndrome or Ehlers Danlos syndrome) or acquired, with risk factors including hypertension, atherosclerosis, and smoking among others.

The prevalence of AAA is 8.8% in the population above the age of 65, accounting for more than 15,000 deaths in the US and 8,000 in the United Kingdom every year (Newman et al., 2001). In the Multicenter Aneurysm Screening Study (MASS) (Ashton et al., Nov 2002), 67,800 men in the UK between 65-74 years old were screened using ultrasound examination, during a 10-year period. In these individuals, a 4.9% prevalence of AAA was detected. Another screening study in Australia of 12,200 men between ages 65-83 showed a 7.2% prevalence (Newman et al., 2001).

The indications for aneurysm repair (either surgical or endovascular) are largely based upon the presence of symptoms, aneurysm size, and the rate of expansion. Patients with symptomatic aneurysms should undergo repair, regardless of aneurysm diameter. Patients with asymptomatic aneurysms that reach a diameter of 5.5cm should be considered for repair (Powell et al., 2007). Early repair may be beneficial in patients whose aneurysm increases ≥ 0.5 cm in diameter in six months (Karkos et al., 2000; Limet et al., 1991).

Although the criterion for AAA repair varies in practice, the maximum diameter is the most frequently used clinical AAA repair indication. However, the diameter criterion is under controversial discussion since only 25% of AAAs rupture in a patient´s lifetime (Brown & Powell, 1999). Consequently, small AAAs (<5.5cm) rupture and large AAAs (>5.5cm) remain stable, whereas surgical interventions continue to pose serious risk especially in elder patients (Thompson et al., 2009). Therefore, alternative rupture risk indices have been proposed in order to target patients that require AAA repair. Specifically, biomechanical parameters like peak wall stress (PWS) or peak wall rupture risk (PWRR) have shown to be a feasible an promising alternative that can be used to better ascertain the risk of rupture (Di Martino et al., 1998; Fillinger et al., 2003; Gasser et al., 2010; Heng et al., 2008; Maier et al., 2010; Raghavan & Vorp, 2000; Thubrikar et al., 2001; Truijers et al., 2007; Vande Geest et al., 2006b; Venkatasubramaniam et al., 2004). The computation of such parameters requests: (i) accurate methods for reliable reconstruction of the aortic geometry, (ii) appropriate material properties for the aneurysmatic tissues, (iii) realistic (physiological) boundary conditions, and (iv) along with adequate numerical methods must be developed to solve the biomechanical problem (Gasser, 2012).

1.1. DEMOGRAPHICS

The formation of abdominal aortic aneurysm is primarily a disease of the elder male ages 50 years and above. The incidence of AAA is 4 to 6 times greater in men than women, with this difference dissipating after the 8th decade of life (Cronenwett et al., 5fh ed. ed. 2000,; Vardulaki et al., 2000.) This being said, the annual risk of rupture for females was shown to be 3 times that for males (Brown & Powell, 1999). Aneurysmal disease primarily occurs in the white race, as shown in a study utilizing the Nationwide Inpatient 2 Sample of 1994-1996 (Huber et al., 2001), Table 1. This table also outlines the preference of this disease to the male aged 60 years and above.

Table 1. Patient demographical data from a random sampling in the US (Huber et al., 2001)

Patient Demographics		
Age	Number	
50-50 y	960	(5.8%)
60-69 y	5,228	(31.8%)
70-79 y	7,965	(48.4%)
Male	13,114	(79.7%)
Female	3,340	(20.3%)
White	13,009	(94.7%)
Black	286	(2.1%)
Other race	450	(3.3%)

1.2. BIOLOGICAL FACTORS

The pathogenesis of abdominal aortic aneurysms (AAA) is still relatively unknown. Presence of immune reaction factors such as macrophage and lymphocytes, SMC (smooth muscle cell) apoptosis, degraded extracellular matrix (ECM) and neovascularization, and increased concentration levels of certain types of matrix-metallo-proteinases (MMP), are commonly observed in the aneurysmal aorta. These observations suggest that the remodeling process of the wall is on-going, though not in ideal balanced manner. AAA has also been found to be associated with smoking, familial history, and chronic obstructive pulmonary disease (COPD). Many studies point toward unbalanced ECM turnover as a key factor in the development of aneurysms. In this phenomenon, the ECM is broken down, and subsequent alterations in the ECM composition occur that ultimately results in the localized focal dilatation of aorta. This process, however, is triggered or inhibited by many other factors related to AAA, the exact role and activation details of which are not yet completely understood.

1.2.1. Proteolytic degradation of the AAA wall

Elastin, collagen types I and III, and vascular smooth muscle cells make up the normal aortic wall. Elastin fibers are present in the media and are convey elasticity to the wall, while collagen helps to provide tensile strength.

Histological examination shows a thinned aneurysmal aortic wall with decreased levels of medial elastin; an unbalanced proteolytic degradation of these structural constituents results in AAA. It is known that the loss of elastin is associated with aneurysmal dilation, whereas collagen loss is associated with aneurysmal rupture (Dobrin, 1989). Indeed, experimental studies have shown that treatment with elastases, enzymes that hydrolyze elastin, leads to arterial dilation, while treatment with collagenases, enzymes that hydrolyze collagen, leads to rupture without dilation (Choke et al., 2005).

Out of these, matrix-metallo-proteinases (MMPs) have been widely implicated in AAA pathogenesis and hence are described in detail in the following section.

1.2.2. Matrix-Metallo-Proteinases (MMPs)

MMPs are zinc and calcium dependent endopeptidases of the metzincin superfamily of proteinases that degrade elastin and collagen. MMP-2, 9 and 12 have all been postulated to have a significant role in aneurysm formation. MMP in its non-activated form is called proMMP and is activated by an outside agent. MMP-9, also known as Gelatinase B or 92kD type IV collagenase, is predominantly produced by macrophages and constitutes the major elastase in human AAAs, while minimal amounts are found in normal aortic tissue.

Many investigators have also examined the role that MMP-2 (Gelatinase A or 72 kDa type IV collagenease) plays in the developing aneurysm. MMP-2 is expressed by vascular smooth muscle cells and may facilitate the degradation of both elastin and collagen in the aortic wall. Investigators have found elevated levels of both MMP-2 mRNA and protein levels in aneurysmal tissue when compared with normal tissue and atherosclerotic tissue. It is suggested that MMP-2 is responsible for the initial formation of small aneurysms, while MMP-9 is responsible for the growth in moderate sized aneurysms (5 to 7 cm diameter)

(Freestone et al., 1995; Thompson & Cockerill, 2006). Higher MMP-9 expression in the AAA wall relative to Atherosclerotic Occlusive Disease (AOD) samples has been reported elsewhere (Abisi et al., 2007). It supports the view that AOD and AAA have different pathologies.

Fontaine et al (Fontaine et al., 2002) proposed that intraluminal thrombus absorbs blood components and stores, releases and participates in the activation of proteases involved in aneurysmal evolution. Spontaneous clotting of the blood was found to induce the release of pro-MMP-9 into serum that is 4 folds higher than the paired control plasma and that fibrinolysis progressively releases more MMP-9 in a time dependent manner. They also report that leukocytes are the main source of MMP-9 during clot formation. This is in agreement with the clinically observed fact that patients with previously stable AAAs had a seemingly high rate of early rupture after undergoing an unrelated operation (Swanson et al., 1980).

1.2.3. Tissue Inhibitors of Metalloproteinases (TIMP)

TIMP are predominant inhibitors of MMP activity. In the normal human aorta, a balance in the tissue levels of MMP and TIMP helps to create equilibrium in the ECM between synthesis and degradation. TIMP-1 is a specific inhibitor of MMP-9. Eskandari et al (Eskandari et al., 2005) subjected both TIMP-1 KO mice and wild-type mice to intra-aortic infusion of elastase to stimulate aneurysm growth. The TIMP-1 KO mice demonstrated a significant increase aortic diameter when compared to the wild-type variety. It is also reported that TIMP-1 deficiency contributes to a reduction in atherosclerotic plaque size but promotes aneurysm (Silence et al., 2002). It should be noted that it is the difference between degradation and repair activities of the vascular wall that results in aneurysm formation and not the degradation activity alone.

1.2.4. Macrophage and lymphocyte presence

Histologically, it has been observed that macrophages and lymphocytes are present in the aneurysmal wall. What triggers the penetration of these immune system cells into the wall is still unknown.

Elastin degradation products are proposed to be chemo-attractant proteins for the macrophages (Senior et al., 1980). Kazi et al (Kazi et al., 2003) have observed the chemotaxis and have verified the presence chemo-attractant proteins within the wall covered by intra-luminal thrombus. The observed deposition of immunoglobulin (IG) in the aneurysmatic aortic wall also substantiates the fact that the pathogenesis of AAA may have origin in the autoimmune response. Macrophages and lymphocytes secrete a cascade of cytokines that results in activation of many proteases (see Figure 2). Also, 55% of the aneurysmatic population has been found infected with chlamydiae pneumonia (Ailawadi et al., 2003). A recently applied Positron Emission Tomography (PET) imaging method for detecting metabolic activity in aneurysm is based on the fact that macrophage are engaged in significant glycolysis activity on their surface. The positron emitting chemical marker called fluorodeoxyglucose (F18 FDG) was used to trace glycolysis activity on aneurysm surface (Reeps et al., 2008; Sakalihasan et al., 2002; Xu et al., 2010).

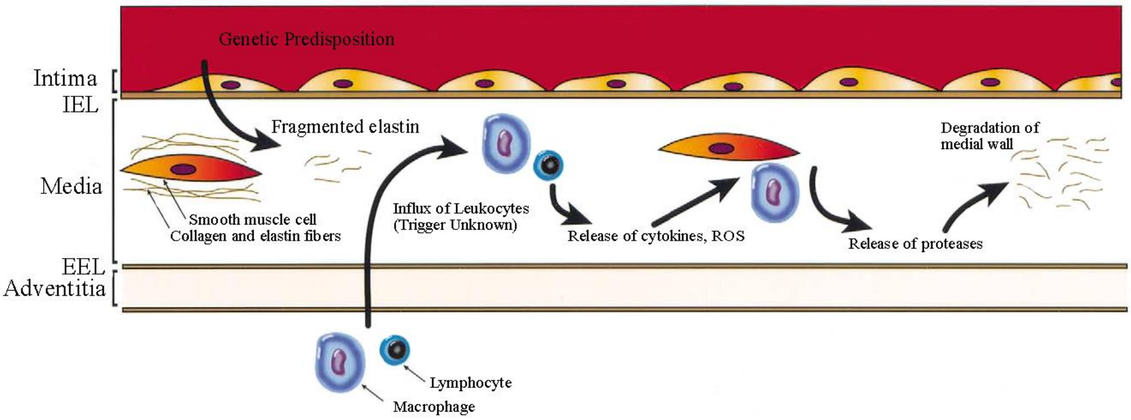
Genetic Predisposition
Intima
IEL
Media
EEL
Adventitia
Fragmented elastin
Smooth muscle cell
Collagen and elastin fibers
Influx of Leukocytes
(Trigger Unknown)
Release of cytokines, ROS
Degradation of
medial wall
Release of proteases
Lymphocyte
Macrophage

Figure 2. Localized stresses, fragmented medial proteins, and genetic predisposition, likely attract inflammatory cells into the aortic wall. Released chemokines, cytokines, and reactive oxygen species by these inflammatory cells, results in further influx of leukocytes, and further medial degradation (Ailawadi et al., 2003).

1.2.5. Reactive Oxigen Species (ROS)

In-vitro studies suggest that ROS activate MMP (Siwik et al., 2001), thereby having an important role in AAA pathogenesis. ROS are also found to cause apoptosis of the vascular smooth muscle cells, contributing to wall weakening. High levels of DNA fragmentation are found in aneurysmal medial smooth muscle cells; they are a marker for SMC apoptosis. The wall, though under degradation because of protease action, is simultaneously being synthesized because of protein generation by SMCs. ROS accelerate the wall degradation by promoting MMP action as well as decreasing protein synthesis by SMC apoptosis and damage to the structural integrity of the wall. It is hypothesized that ROS activate the pro-MMPs by covalently modifying the sulfur group of the cysteine switch (Wassef et al., 2001).

1.2.6. C-Reactive Proteine (CPR)

CRP, produced mainly by hepatocytes in the liver, has been established as an important factor in atherosclerosis pathology (Saratzis et al., 2011). Increased high-sensitive-C-Reactive Protein (hsCRP) has been observed in AAA patients (Wanhainen et al., 2005). This observation was supported by Wiernicki et al (Wiernicki et al., 2010) as they found a correlation between haptoglobin polymorphism and AAA, and elevated CRP levels in the AAA patients. However, growth rate was found not to have a significant association with CRP levels in a multivariate analysis.

1.2.7. Genetic Aspects

Genome wide association studies have consistently reported associations between a region on chromosome 9p21.3 and a broad range of vascular diseases, such as coronary artery disease (CAD), aortic and intracranial aneurysms and type-2 diabetes (T2D) (Bjorck et al., 2009). Ethnic association of AAA disease and frequently observed familial history has established genetic link of AAA by now (Baumgartner et al., 2008; Brown & Powell, 1999; Ogata et al., 2005; Saratzis et al., 2011; Shibamura et al., 2004). In 15% of AAA patients, it is found familial history (Saratzis et al., 2011). This emphasizes the need to explore genetic aspects involved in AAA. Marfan syndrome (MFS) and Thoracic Aortic Aneurysm and Dissection (TAAD) have been well characterized for their genetic links compared to AAA (Saratzis et al., 2011). However, genome wide studies have made advances in recent year to finger point the location on chromosomes related to AAA disease. Shibamura et al (Shibamura et al., 2004) reported loci of the AAA to be 19q13 (AAA1) and 4q31 (AAA2). Recently, Elmore et al (Elmore et al., 2009) reported the AAA loci to be 3p12.3.

1.2.8. Miscellaneous factors

Gender dependence of the AAA and association with smoking was highlighted in the UK Small Aneurysm Trial that based its finding on 1090 patients (UKSAT) (Brown & Powell, 1999). The trial found that female patients have less occurrence of AAA, however, chances of rupture of AAA were found higher in female patients. Biomechanical aspects were explored from gender perspective by Larsson et al (Larsson et al., 2011), however, differences found were not statistically significant. Their relatively smaller pool of patients could be the culprit. Also, chances of occurrence of AAA in the family of female patients were found higher than that in case of the male patients. Association of smoking has been debated since many of the studies that include the smoking as a variable in patient trial have not taken into account the COPD as a separate fact (Choke et al., 2005).

Influence of diabetes on AAA is debated. Baumgartner et al (Baumgartner et al., 2008) report inverse association. Diabetic patients with Haptoglobin polymorphisms Hp 2-1 and Hp 2-2 phenotype are reported to have lower elasticity compared to those with Hp 1-1 phenotype. However, in most of the mycotic aneurysms *diabetes mellitus* is found to be common (Chen et al., 2009).

Inhibition of platelet activation is reported to have reduced aneurysm diameter, thrombus development, platelet CD41 expression, leukocyte infiltration and elastic degradation of the aortic wall in experiment with rat model (Dia et al., 2009)

According to the aforementioned discussion, AAA etiology can be summarized as follows (Samarth et al., 2013):

1. Some unknown event attracts the attention of leukocytes to the infrarenal segment of aorta

2. Penetration of the leukocytes into the wall of aorta
3. Macrophages start secreting chemokines, ROS, pro-MMPs in extracellular fluid
4. pro-MMP gets activated
5. TIMP presence may attempt to neutralize the MMP activity
6. MMP activity dominates the TIMP resistance. Thus, net result is degradation of structural matrix proteins
7. Over a period the activity continues. The loss of elastin reduces the stiffness of the wall. Therefore, the aorta begins to bulge out in form of an aneurysm
8. Collagen degradation weakens the wall
9. Smooth muscle cells undergo apoptosis. This hampers the rebuilding activity of wall structural proteins
10. Interstitial collagen distribution becomes disorganized
11. Aneurysm increasingly expresses T cells, B cells, and plasma cells. This highlights the momentum of the autoimmune system
12. Th-1 cells are encouraging the inflammatory action and thereby aneurysm whereas Th-2 cells try to suppress the same.

1.3. GEOMETRIC FACTORS

1.3.1. Maximum diameter

Currently, the clinical management of AAAs is based on maximum diameter and expansion rate of an aneurysm (Ashton et al., Nov 2002; Brady et al., 2004). However, reports show that these two metrics are not a reliable measure of individual rupture risk. This is evident by the small aneurysms (diameters less than 5.0 cm) that do rupture and the larger aneurysms that have exceeded the threshold size for elective intervention that do not rupture.

In an autopsy study of four hundred and seventy-three non-resected aneurysms (Darling et al., 1977), 13% of the aneurysms with a maximum diameter less than 5.0 cm ruptured and 60% with diameters greater than 5.0 cm remained intact. Other studies report similar findings of small aneurysms rupturing, indicating that the current use of the maximum diameter or expansion rate may be insufficient in that it underscores the variable behavior of individual aneurysms.

In an interesting study by Solberg et al (Solberg et al., 2010), where 4265 subjects with a normal sized aorta resulted in 116 AAAs diagnosed after 7 years, a statistical analysis revealed that the baseline diameter was a highly significant ($p < 0.001$), strong (95% CI: 7–76 times higher risk) and gender-independent risk factor for developing AAA. They also found that median diameter increases less with age compared to mean diameter, indicating that there was less increase in diameter for people with smaller aorta in the beginning. Another interesting finding of the study was that when adjusted for age and aortic diameter, male sex was not significantly associated with AAA. It implies that geometry matters more than gender and hence biological differences. These findings are in agreement with previously reported fact that growth rate of larger non-aneurysmatic aorta was higher than the smaller non-aneurysmatic aorta (Mizowaki et al., 2009). These findings emphasize the role of size as a geometric factor involved in the aneurysmatic condition of the aorta and progression of disease.

1.3.2. Shape Effect

The mechanics of the AAA wall and the resulting distribution of wall stress are primarily determined by the individual shape, not size, of the aneurysmal aorta. While precise soft tissue characterizations of the wall and thrombus, as well as patient-specific blood flow velocity measurements, are important to achieve accurate computational predictions of the flow-induced wall stresses, the native AAA geometry is the most important feature to consider in evaluating the wall mechanics (Samarth et al., 2013). Limiting the characterization of geometry to the measurement of maximum diameter or expansion rate from medical images is not the best strategy to address the at-risk status of aneurysms on an individual basis. AAA shape is complex; most aneurysms are generally tortuous, asymmetric, and with amorphous multi-layered ILT (Vorp, 2007). Moreover, the implementation of patient-specific non-uniform thickness of the arterial wall in the analysis is a complex task, due primarily to limitations in the current technology to measure this parameter non-invasively.

Ruptured AAAs seem to be less tortuous and have a larger cross-sectional diameter asymmetry (Dobrin & Mrkvicka, 1994), which is consistent with FEA studies showing that the highest wall stress is obtained in AAAs with an asymmetric geometry (Vorp et al., 1998). The evidence for geometric asymmetry is further supported by the finding that peak wall stress is localized near the aorta-aneurysm inflection point where the aneurysm curvature changes (Fillinger et al., 2003). Moreover, the location of maximum stress at the posterior wall seems to coincide with peaks in the magnitude of the Gaussian curvature (Nyilas et al., 2005). Idealized fusiform and saccular models have also shown that wall stress increases with bulge diameter and asymmetry (Rodriguez et al., 2008; Vorp et al., 1998).

1.3.3. Presence of Intra-luminal thrombus

A common feature in most AAAs is the presence of an intra-luminal thrombus (ILT). ILT is known to alter the stress distribution in the aneurysmal wall (Dia et al., 2009; Mizowaki et al., 2009; Smith, 2000) and directly affect AAA growth and rupture (Dia et al., 2009; Brown & Powell, 1999; Nagashima et al., 2004; Raghavan et al., 2005; Solberg et al., 2010; Stringfellow et al., 1987) making it important in AAA biomechanics. Despite ILT's impact on aneurysm disease, from a biomechanics perspective, thrombus development and its relation to aneurysm rupture is still not clearly understood. Whether it increases or decreases the risk of aneurysm rupture, i.e., reinforces proteolytic activity (Pappu et al., 2008), which weakens the wall (Dobrin & Mrkvicka, 1994) or buffers against wall stress (Vorp et al., 1998), is still subject to debate.

1.3.4. Wall thickness

A factor of significant importance in AAA rupture risk prediction is the non-uniformity of the wall thickness. Figure 3 shows an estimation of AAA wall thickness distribution obtained from an AAA CT scan (Shum et al., 2010). Di Martino et al (DiMartino et al., 2006), using a laser micrometer, measured the thickness of AAA wall specimens, obtained fresh from the operating room from patients undergoing surgical repair. A significant difference was found in wall thickness between ruptured (3.6 ± 0.3 mm) and electively repaired (2.5 ± 0.1 mm) aneurysms, as well as an inverse correlation between wall thickness and local tissue strength. The tensile strength of ruptured AAA tissue was found to be lower than that for electively repaired tissue (54 N/cm^2 vs. 82 N/cm^2). In the same study, it was found that AAA rupture is associated with aortic wall weakening, but not with wall stiffening.

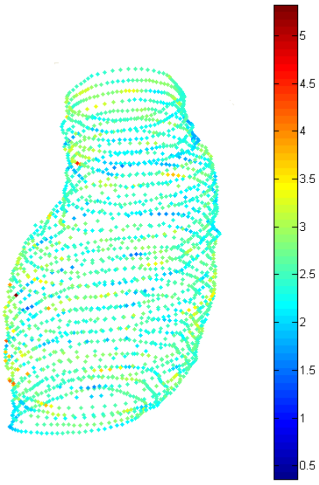

Figure 3. Estimated wall thickness distribution (in mm) in a point cloud resulting from a segmented CT dataset (Shum et al., 2010).

Since AAA wall strength in large aneurysms did not correlate positively with maximum transverse diameter, wall thickness would be a better predictor of rupture for large AAAs. In an autopsy study, Raghavan et al (Raghavan et al., 2006) analyzed the tissue properties of three un-ruptured and one ruptured AAA revealing that all aneurysms had considerable regional variation in wall thickness and there was a significant reduction in wall thickness near the rupture site. Similarly, Mower et al (Mower et al., 1993) demonstrated that the wall thickness represents a major parameter influencing wall stress distribution, rather than aneurysm maximum diameter alone.

1.3.5. Geometry and Peak Wall Stress

Geometric features have been shown to be significant predictors of PWS and subsequent risk of rupture or tendency (Fillinger et al., 2002; Fillinger et al., 2003; Venkatasubramaniam et al., 2004). Multiple regression analysis was performed on 39 patients and 17 features to assess the influence of the features on the peak wall stress (Giannoglou et al., 2006). Among the geometrical parameters, PWS was correlated with the mean centerline curvature, the maximum centerline curvature, and the maximum centerline torsion of the AAAs, with mean centerline curvature as the only significant predictor of PWS and subsequent rupture risk resulting from the multiple regression analysis. A multivariate analysis of 40 variables of 259 aneurysms revealed that ruptured aneurysms tend to be less tortuous and have a greater cross-sectional diameter asymmetry (Fillinger et al., 2004).

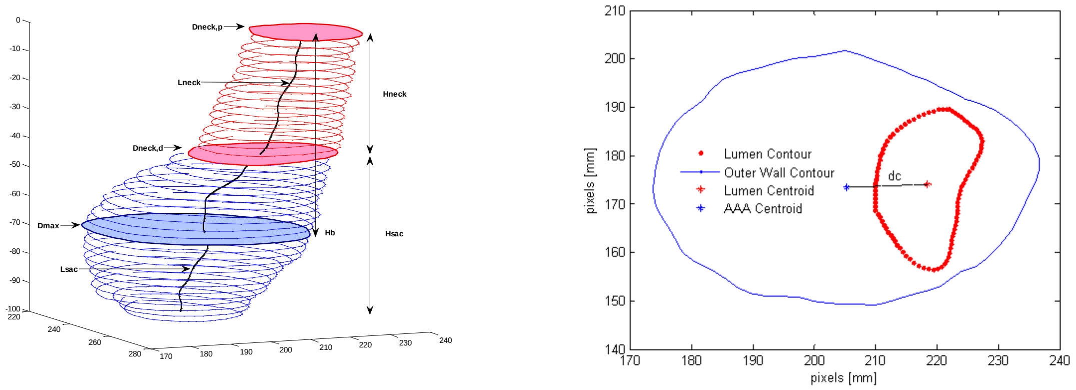

(a)

(b)

Figure 4. (a) 1-D size indices: maximum diameter (D_{max}), proximal neck diameter ($D_{neck,p}$), distal neck diameter ($D_{neck,d}$), sac height (H_{sac}), neck height (H_{neck}), sac length (L_{sac}), neck length (L_{neck}), bulge height (H_b); (b) 1-D size index: centroid distance at the maximum diameter (dc).

Current research had been concerned with identifying features in aneurysm morphology that are correlated with peak wall stress, and therefore rupture. Georgakarakos (Georgakarakos et al., 2010a) developed a linear model to associate PWS and geometric parameters. They report that the optimal predictive model can be formulated as follows: *PWS = 8.791 + 2.3953*MaxDiameter + 25.2923*IntTortuosity* (Georgakarakos et al., 2010a). Shum et al developed a quantitative pipeline consisting of image segmentation (Shum et al., 2010; Shum et al., 2011b) and geometry quantification to compute 64 features that describe the size, shape, wall thickness, and curvature for a subset of ruptured and unruptured aneurysms (see Figure 4).

Utilizing these features, a decision tree model (see Figure 5) was trained on 76 AAAs and a prediction accuracy of 87% for sac length, surface area, tortuosity, and the ratio of ILT to AAA volume was obtained (Shum et al (Shum et al., 2011a)).

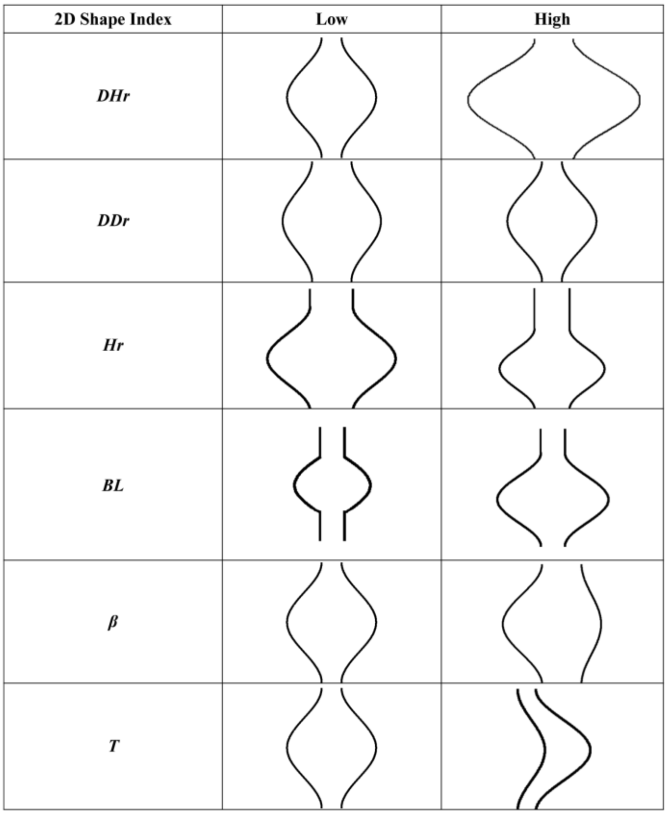

Figure 5. Schematic of 2D shape indices providing an approximate measure to construe the global AAA shape: diameter to height ratio (DHr), diameter to diameter ratio (DDr), height ratio (Hr), bulge location (BL), asymmetry (β), and tortuosity (T).

In addition to linking geometric features to rupture potential, five “*geometric biomechanical factors*” were recently combined to obtain a *rupture risk qualitative indicator* (Vilata et al., 2010):

- Deformation rate
- Asymmetry
- Saccular index
- Relative wall thickness
- Growth rate

This index was defined to monitor the evolution of patients with aneurysms by integrating geometric information obtained from periodic checkups in an effort to improve the accuracy of rupture risk assessment.

Validation studies were only performed on one clinical case and three cases obtained from the literature, and a broader study enrolling more patients is currently in progress. Results show that the deformation rate and growth rate are more influential on the rupture potential of aneurysms than the maximum diameter, and that a rupture risk qualitative indicator greater than 0.64 (nondimensional, based on the weighted averages of the five geometric biomechanical factors) indicates elective repair should be considered.

1.4. BIOMECHANICAL FACTORS

From a purely biomechanical viewpoint, aneurysm rupture is a phenomenon that occurs when the mechanical stress acting on the dilating inner wall exceeds its failure strength. Therefore, a criterion for repair based upon quantifying aneurysm stress and strength could facilitate a better method to determine at-risk AAAs.

Unfortunately, obtaining in vivo patient-specific measurements of tissue stresses or strength non-invasively is currently not feasible. However, mathematical and computational models that accurately compute the aneurysmal wall stress can be utilized to evaluate the AAA biomechanical environment at the organ scale. In addition, recent research has pointed the unsuitability of deciding a surgical repair based solely on the maximum diameter criterion (Doyle et al., 2009; Doyle et al., 2010; Fillinger et al., 2002; Fillinger et al., 2003; Vorp, 2007). Therefore, alternative rupture risk parameters need to be proposed as alternative to the classical AAA size and expansion rate (McGloughlin & Doyle, 2010).

Early studies used Laplace’s law to correlate AAA diameter and rupture (Dobrin, 1989). However, this approach ignores the complex geometry and boundary conditions as well as the presence of the ILT. In this regard, calculation of the peak wall stress by using finite element analysis was first applied to a 2 dimensional simple geometric shape of AAA by Stringfellow et al (Stringfellow et al., 1987). Their work showed that AAA models with the same diameter but different geometry had different wall stress pointing to the importance of AAA shape and the non adequacy of Laplace’s law even for an idealized approximation of complex geometries. This work was later corroborated by Elger et at (Elger et al., 1996). In addition, the study by Thubrikar et al (Thubrikar et al., 2001) indicates a considerable transmural variation of the maximum principal stress, for which 3D continuum models or advanced shell models are required. A diameter matched approach was used by Gasser et al (Gasser et al., 2010) to emphasize inclusion of ILT in analysis for better ability to distinguish ruptured and non-ruptured aneurysms.

Fillinger et al (Fillinger et al., 2002; Fillinger et al., 2003) showed the feasibility of using finite element analysis (FEA) for patient-specific wall stress calculations and reported statistically significant differences in peak stress for ruptured/symptomatic AAAs (46.8 N/cm^2) in comparison with those electively repaired (38.1 N/cm^2). They also demonstrated that maximum wall stress correlated more closely with the risk of rupture than maximum diameter (Fillinger et al., 2003). In their study, wall stress was calculated by using FEA applied to a population of 103 patients, from which wall stress at a threshold of 44 N/cm^2 had 94% sensitivity and 85% accuracy in predicting rupture, compared to 81% sensitivity and 73% accuracy with the maximum diameter at a threshold of 5.5 cm. A similar study was undertaken by Venkatasubramaniam et al. (Venkatasubramaniam et al., 2004) with 27 patients, from which 15 AAAs ruptured. They found that ruptured AAAs had significantly higher peak wall stress than non-ruptured AAAs (77 N/cm^2 vs. 55 N/cm^2). Both studies (Fillinger et al., 2003; Venkatasubramaniam et al., 2004) found a strong correlation between areas of high stress and the rupture site, based on quasi-static computational solid stress calculations applying a uniform intraluminal pressure directly on the wall.

1.4.1. Effect of blood flow

Most of the wall stress distribution on AAA has been obtained from structural analysis of AAA models by applying a uniform pressure on the inner surface of aneurysm sac. The limitation of this approach is that the hemodynamics of the blood flow through the aneurysm and the compliant nature of the AAA wall are not accounted for.

One of the pioneering works that account for the effect of blood flow on the peak wall stress of AAA was conducted by Di Martino et al (Di Martino et al., 2001). Their fluid-structure interaction (FSI) analysis of a realistic aneurysm aorta model showed that the complicated hemodynamics would considerably affect the stress distribution, but also reported the cushioning effect of ILT on the AAA wall. However, in their work, the wall and ILT were considered linear elastic and isotropic in behavior.

The nonlinear behavior of the wall and ILT as well as more complex flow conditions has been considered in a series of works conducted by Scotti et al (Finol & Scotti, 2007; Scotti et al., 2008; Scotti et al., 2005). These studies have demonstrated the importance of considering the nonlinear elastic behavior of the structure. Also the comparative study between FSI (coupled and decoupled) and Computational Solid Mechanics (CSM) analysis of patient-specific AAA performed by Scotti et al (Finol et al., 2008) show that the non uniform pressure distribution in the inner surface of the AAA due to the flow yielded a maximum peak wall stress up to 20% higher compared to that obtained with static wall stress analysis when a uniform systolic pressure of 117 mmHg is applied.

In these studies it is concluded that FSI analysis has the potential to capture the fluid dynamics inside a complex AAA structure accurately and hence is a better approach for calculating the wall stress and studying rupture risk. Leung et al (Leung et al., 2006) also compared the stress results obtained from FSI model and computational static structural (CSS) model and reported that the addition of fluid flow and compliant wall can change the local stresses slightly but has negligible effect on the peak wall stress. However, they did not consider the presence of ILT in their analysis.

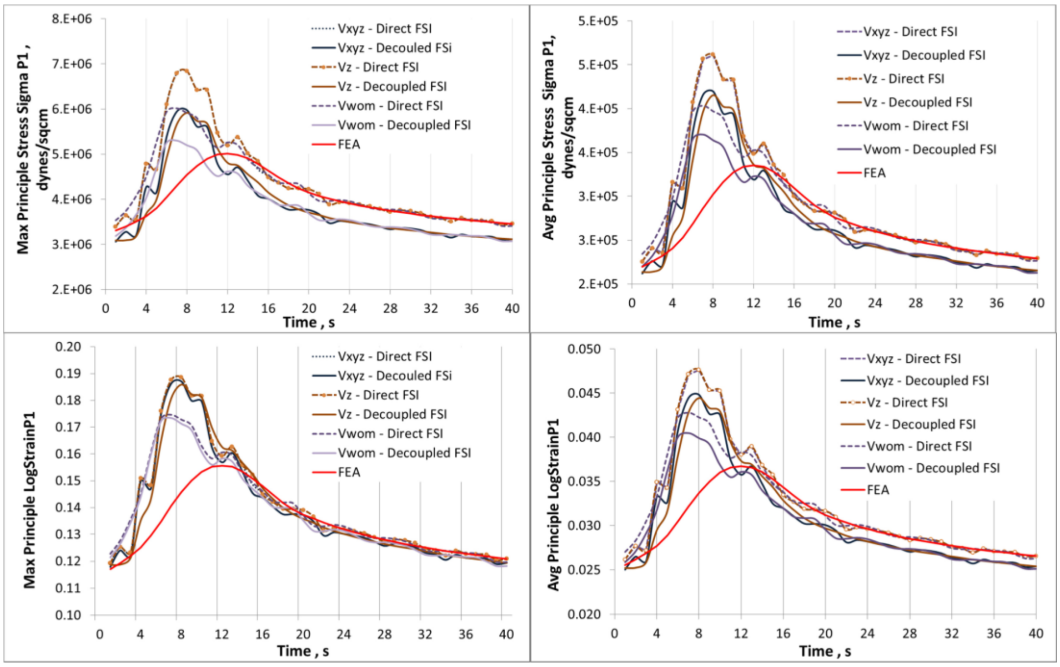

Figure 6. Maximum and average principal stress and strain waveforms for a patient-specific AAA obtained using direct FSI, uncouple FSI and transient FEA. The stress and strain follow the inlet velocity waveform rather than the pressure waveform boundary condition.

One of the main conclusions that can be extracted from these studies is that using a non-uniform pressure distribution on the AAA sac can substantially improve structural analysis avoiding computationally extensive FSI analysis for determining AAA rupture risk. Results from Scotti et al (Scotti et al., 2005; Scotti & Finol, 2007), as well as the importance of considering ILT in FSI analysis were corroborated by subsequent authors (Khanafer et al., 2009; Kim et al., 2008; Papaharilaou et al., 2007). A recent study by Chandra et al (Chandra et al., 2013) demonstrated the effect of MRI derived inlet flow boundary conditions on the fluid-structure-interaction modeling of a patient-specific AAA model with ILT. Comparison of results obtained from fully coupled FSI simulations, decoupled FSI simulations and transient FEA simulations revealed that the stress-strain variations follow the inlet velocity boundary condition rather than the pressure outlet boundary condition and further emphasizes on the fact that peak systolic pressure does not provide the phase for peak stress and strain (see Figure 6).

The influence of material anisotropy in FSI simulations have been investigated by Rissland et al (Rissland et al., 2009) and Xenos et al (Xenos et al., 2010). In their work, Rissland and colleagues introduced a new anisotropic material model of AAA wall to perform FSI simulations of patient-specific AAA geometries in order to develop more reliable predictor for risk of rupture. The ILT was still modeled as a linearly elastic compressible material. The results clearly indicate that the isotropic material properties have less stress values than anisotropic model resulting in underestimating the risk of rupture.

1.5. Objectives

The general framework of the present thesis relies on the capabilities of the numerical simulation of AAAs to aid on estimating their risk of rupture, as well as to better understand its passive mechanics.

Within this context, the present thesis aims to elucidate the effect of the mechanical features of a AAA, namely: anisotropy of the tissue, shape of the lesion, initial stresses, presence and location of the ILT, as well as the possible role of ILT heterogeneity. To achieve this general goal, the following specific goals have been outlined:

- To develop a framework for a reliable Finite Element analysis of patient specific geometries of AAA´s.
- To propose appropriate isotropic and anisotropic hyperelastic material models for aneurysmal arterial tissue based on reported biaxial tests.
- To determine realistic (physiological) boundary conditions and adequate numerical methods to solve the biomechanical problem.
- To develop a pull-back algorithm that allows to determine zero-pressure configuration of an AAA while using both isotropic and anisotropic material models. This algorithm should be general enough to be applied to a variety of biological structures under pressure, e.g., the heart, atria, and cerebral aneurysms among others.
- To study the effect of using zero-pressure configuration against CT based imaged on the peak wall stress and on the general stress field of and AAA in conjunction with isotropic and anisotropic treatments of the arterial wall.
- To study the effect of different ILT´s stiffness and heterogeneity on AAA peak wall stress.

- To study the effect of the presence of ILT on the PWS and the effect of its topology compared to the ILT compliance.

MECHANICAL BEHAVIOR OF THE AAA TISSUES

2. MECHANICAL BEHAVIOR OF THE AAA TISSUES

As mentioned in the previous chapter, an abdominal aortic aneurysm is an abnormal widening of the aorta, commonly developed below the renal arteries and above the iliac bifurcations, in which, an intraluminal thrombus develops in nearly 90% of the cases. Therefore, a reliable finite element simulation of the AAA relies on the identification of appropriate material models for the aortic tissue and the intraluminal thrombus. This chapter describes the material models used in this investigation

2.1. Arterial Tissue

The aorta belongs to the group of elastic arteries which are the ones that have relatively large diameters and are located close to the heart. Microscopically the arterial wall is composed of three distinct layers, the *intima*, the *media* and the *adventitia* as shown in Figure 7 (Holzapfel et al., 2000).

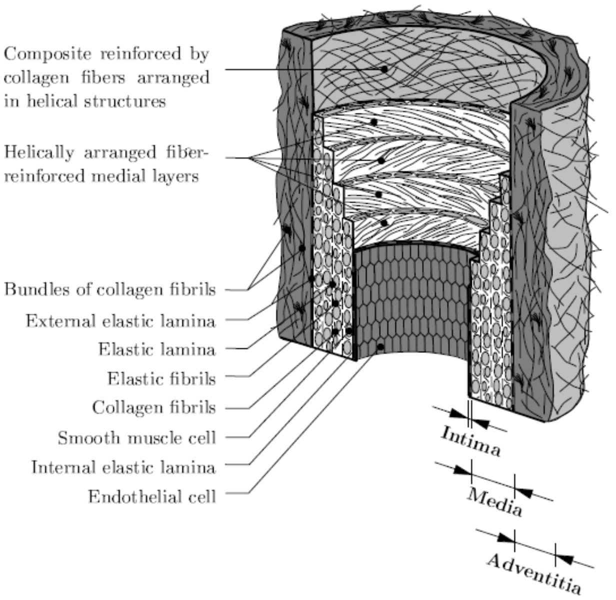
Composite reinforced by collagen fibers arranged in helical structures
Helically arranged fiber-reinforced medial layers
Bundles of collagen fibrils
External elastic lamina
Elastic lamina
Elastic fibrils
Collagen fibrils
Smooth muscle cell
Internal elastic lamina
Endothelial cell
Intima
Media
Adventitia

Figure 7. Diagrammatic model of the major components of a healthy elastic artery composed by three layers: Intima, Media and Adventitia (Holzapfel et al., 2000)

The characteristics of each layer are the following (Holzapfel et al., 2000):

- Intima: Is the innermost layer of the artery. It consists of a single layer of endothelia cells lining the arterial wall and resting on a thin basal membrane. In healthy young individuals the intima is very thin and makes an insignificant contribution to the solid mechanical properties of the arterial wall; however it thickens and stiffens with age (arteriosclerosis) so that the mechanical contribution may become significant.
- Media: Is the middle layer of the artery and consists of a complex three-dimensional network of smooth muscle cells, and elastin and collagen fibrils. The orientation of and close interconnection between the elastic and collagen fibrils, elastic laminae, and smooth muscle cells together constitute a continuous fibrous helix which has a small pitch so that the fibrils in the media are almost circumferentially oriented. This structured arrangement gives the media high strength, resilience and the ability to resist loads in both longitudinal and circumferential directions. From the mechanical perspective, the media is the most significant layer in a healthy artery.
- Adventitia: Is the outermost layer of the artery and consists mainly of fibroblasts and fibrocytes (cells that produce collagen and elastin), histological ground substance and thick bundles of collagen fibrils forming a fibrous tissue. The wavy collagen fibrils are arranged in helical structures and serve to reinforce the wall. They contribute significantly to the stability and strength of the arterial wall. The adventitia is much less stiff in the load-free configuration at low pressures than the media, however at high levels of pressure the collagen fibers reach their straightened lengths and the adventitia changes to a stiff ´jacket-like’ tube which prevents the artery from overstretch and rupture.

Healthy arteries are highly are highly deformable composite structures and show a nonlinear stress-strain response with a typical (exponential) stiffening effect at higher pressures (He & Roach, 1994; Holzapfel et al., 2000; Summer et al., 1970). This stiffening effect, common to all biological tissues, is based on the recruitment of embedded (load carrying) wavy collagen fibrils, which leads to the characteristics anisotropic behavior of arteries (Holzapfel et al., 2000).

Several models that describe the behavior of AAA are available (Raghavan & Vorp, 2000; Raghavan et al., 1996; Vande Geest et al., 2006b; Rodriguez et al., 2009; Rodriguez et al., 2008; Baek et al., 2007; Polzer et al., 2012; Gasser, 2012). For AAA wall early studies formulated microstructure-based models by the known of fibrous nature of the tissue, for example Raghavan’s et al (Raghavan et al., 2006) was associated with the state of the elastin and collagen within the arterial wall. However, microstructure-based models are difficult to utilize for the estimation of wall stresses in intact three-dimensional (3D) vessels, so it is more appropriate to utilize continuum-based constitutive models which describe gross mechanical behavior (Vorp, 2007; Vande Geest et al., 2006b; Vorp et al., 1995).

Isotropic constitutive models have been fitted from uniaxial loading conditions which are useful in many ways, starting from their simplicity, but biaxial testing had allowed a more appropriate modeling of aortic tissue revealing the anisotropic behavior of arterial wall (Holzapfel et al., 2000; Vorp, 2007)

Planar biaxial testing by Vande Geest et al. (Vande Geest et al., 2006b) as well as well as findings by Di Achille (Di Achielle et al., 2011) demonstrated that the aneurysmal degeneration of aortic tissue leads to an increase in mechanical anisotropy, with the circumferential direction being stiffer. This study also showed that the aneurysm wall of the average population is highly nonlinear but rather isotropic. This motivated the development of improved constitutive models for the AAA wall (Rodriguez et al., 2008; Vande Geest et al., 2006b) permitting more elaborated computations of AAA and the reassessment of established biomechanical markers of AAA rupture risk (Rissland et al., 2009; Rodriguez et al., 2009; Rodriguez et al., 2008).

For this thesis, both isotropic and anisotropic models are used, as patient-specific biaxial testing are best fitted with anisotropic model but mean population testing are well fitted with isotropic models.

It is postulated the existence of a strain-energy function (SEF) W from which the stress-strain behavior of the material can be derived. To express W

as a function of the invariants it is employ the multiplicative decomposition for the deformation gradient $\mathbf{F} = \mathbf{F}_{vol}\bar{\mathbf{F}}$ into a volumetric part $\mathbf{F}_{vol} = J^{+1/3}\mathbf{I}$ and an isochoric part $\bar{\mathbf{F}} = J^{-1/3}\mathbf{F}$, with the volume ratio $J = \det\mathbf{F} > 0$ and $\det\bar{\mathbf{F}} = 1$. Under these considerations the SEF *W* can be written as

$$\boldsymbol{W}(\boldsymbol{C}, \mathbf{a_0}) = \boldsymbol{U}(\boldsymbol{J}) + \overline{\boldsymbol{W}}(\bar{\boldsymbol{I}}_{\mathbf{1}}, \bar{\boldsymbol{I}}_{\mathbf{2}}, \bar{\boldsymbol{I}}_{\mathbf{4}}), \qquad \text{(Eq. 1)}$$

where $\mathbf{C} = \mathbf{F}^T\mathbf{F}$ is the right Cauchy-Green tensor and $\mathbf{a_0}$ denotes a unit vector along the direction of anisotropy of the tissue which is assumed to coincide with the circumferential direction of the vessel (Alastrué et al., 2006.) as shown in Figure 8.

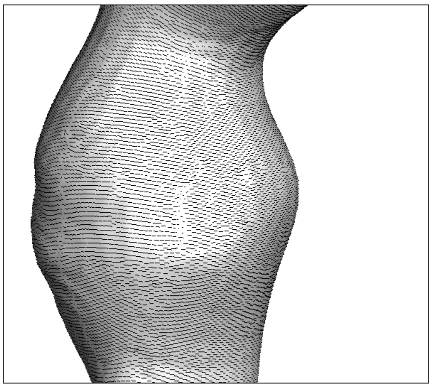

Figure 8. Circumferential direction of anisotropy in an AAA

The volumetric elastic response *U* and isochoric elastic response $\bar{W}$ of the material are given scalar-valued functions of *J* and the invariants $\bar{I}_1, \bar{I}_2, \bar{I}_4$, which are expressed in terms of $\bar{\mathbf{C}} = \bar{\mathbf{F}}^{\boldsymbol{T}}\bar{\mathbf{F}}$, the modified right Cauchy-Green tensor, and $\mathbf{a_0}$ as

$$\begin{gathered} \bar{I}_1 = \mathrm{tr}\bar{\mathbf{C}}, \quad \bar{I}_2 = \frac{1}{2}[(\mathrm{tr}\bar{\mathbf{C}})^2 - \mathrm{tr}\bar{\mathbf{C}}^2], \\ \bar{I}_4 = \mathbf{a}_0 \cdot \bar{\mathbf{C}} \cdot \mathbf{a}_0. \end{gathered} \qquad \text{(Eq. 2)}$$

The second Piola–Kirchoff stress tensor can be obtained from the defined SEF as:

$$\mathbf{S} = Jp\mathbf{C}^{-1} + 2J^{-2/3} \sum_{\substack{i=1 \\ i\neq 3}}^{4} \frac{\partial \bar{W}}{\partial \bar{I}_i} \mathrm{DEV}\left(\frac{\partial \bar{I}_i}{\partial \bar{\mathbf{C}}}\right), \qquad \text{(Eq. 3)}$$

where $p = {dU}/{dJ}$ is the constitutive equation for the hydrostatic pressure *p*, and $\mathrm{DEV}(\cdot) = (\cdot) - \frac{1}{3}[(\cdot){:}\,\mathbf{C}]\mathbf{C}^{-1}$ is the deviatoric operator in the Lagrangian description. The Cauchy stress tensor can be derived from the previous definition as

$$\boldsymbol{\sigma} = J^{-1}\mathbf{FSF}^{T}. \qquad \text{(Eq. 4)}$$

For the case of isotropy, the material response of the aneurysm wall tissue was characterized by the SEF (Demiray, 1972):

$$W_{wall}^{iso} = \kappa(J-1)^2 + D_1\left(e^{D_2(\bar{I}_1-3)} - 1\right), \qquad \text{(Eq. 5)}$$

where D_1 and D_2 are material parameters and κ is the volumetric modulus.

For the case of anisotropy, the aneurysmal wall tissue was modeled by a SEF (Rodriguez et al., 2008):

$$\begin{aligned} W_{wall}^{aniso} \;=\; & \kappa(J-1)^2 + D_1\left(e^{D_2(\bar{I}_1-3)} - 1\right) \\ & + \frac{k_1}{k_2}\left(e^{k_2(\bar{I}_4-1)^2} - 1\right), \end{aligned} \qquad \text{(Eq. 6)}$$

where D_1, D_2, k_1, k_2 are material parameters. This approach is to be used due to the lack of histologic evidence regarding the fiber distribution in aneurysmal tissue. The wall's stiffer response corresponds to its circumferential direction, i.e. as it has been verified through biaxial testing in Vande Geest et al. (Vande Geest et al., 2006b).

The material parameters for the constitutive models, Eqs. (3) and (4), are obtained by regression analysis of the mean biaxial test for aneurysmal tissue reported means of a nonlinear in Vande Geest et al. (Vande Geest et al., 2006b). Table 2 shows the identified model parameters for both constitutive models.

Table 2. Material parameters for the isotropic, Eq. (5), and anisotropic, Eq. (6), aneurysmal wall tissue constitutive models.

Model	D_1 (kPa)	D_2	K (kPa)	k_1 (kPa)	k_2
Isotropic	0.214	41.	E4	-	-
Anisotropic	0.214	41.3	E4	0.212	130

Figure 9 shows the fit for the isotropic model, Eq. 5, to the original data reported by van de Geest (R^2=0.943), whereas Figure 10 shows the same results for the anisotropic model (R^2=0.953).

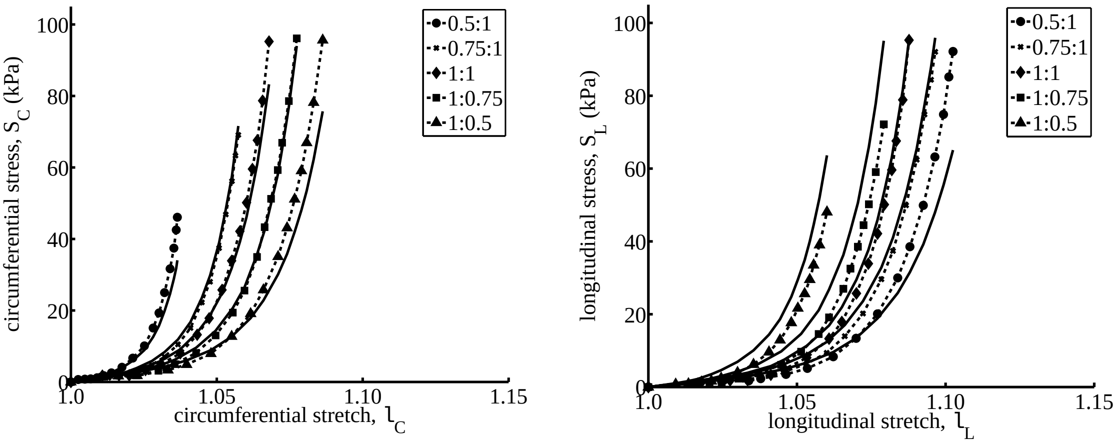

(a) (b)

Figure 9. Biaxial experimental data from vande Geest et al. (Vande Geest et al., 2006b) versus predicted results by the isotropic SEF Eq. (5) in the (a) circumferential and (b) longitudinal directions.

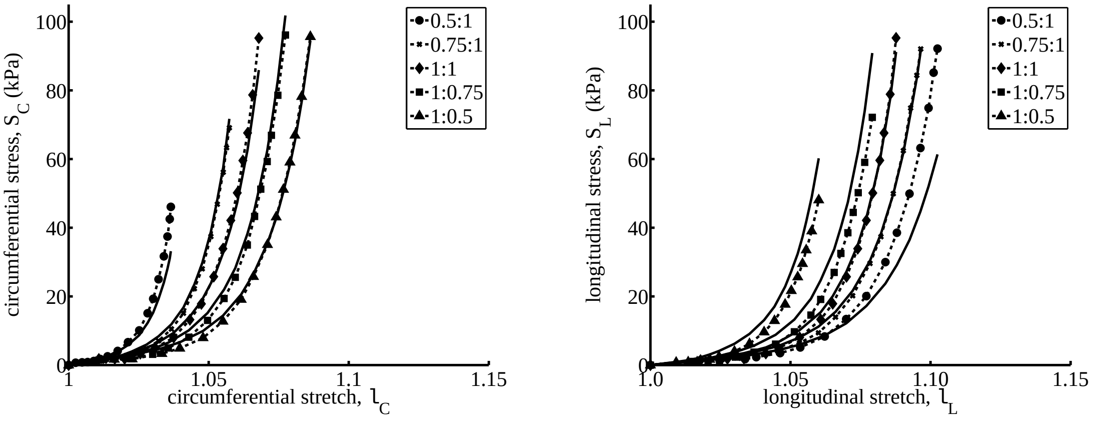

(a) (b)

Figure 10. Biaxial experimental data from vande Geest et al. (Vande Geest et al., 2006b) versus predicted results by the anisotropic SEF Eq. (6) in the (a) circumferential and (b) longitudinal directions.

Both models produce comparable results since the mean stress-strain data reported in Van de Geest et al (Vande Geest et al., 2006b) shows little degree of anisotropy. It is also to be noted that, even though our material model takes into account the behavior of aneurysmal tissue, either model (Eq. 5 and Eq. 6) does not distinguish between distinct wall layers. While the normal arterial wall is built-up by intimal, medial and adventitial layers, this structure is lost through aneurysmal disease (Govindjee & P.M., 1998).

2.2. Intraluminal Thrombus

Most AAAs of a size that approaches a risk of rupture contain an Intraluminal thrombus (ILT) (Hans et al., 2005), see Figure 11, which is a non-homogenous multilayer clot, that adheres to part or all of the dilated aortic wall. It is located within the sac of 75% of clinically-relevant AAAs (Harter et al., 1982) yet its role in AAA rupture risk is much disputed and not entirely understood.

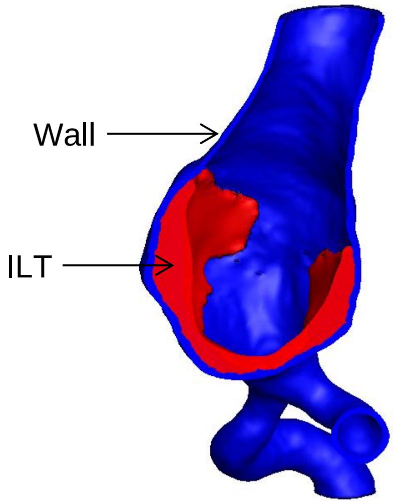

Figure 11. Intraluminal thrombus (ILT)

The presence of an ILT may partially compensate for the hemodynamic effects from arterial expansion. An ILT can restore the lumen of a distended aorta to a semi-normal size and to a certain extent absorbs the stress on the degraded AAA like a cushion, thereby lowering wall stress (Speelman et al., 2010), in other words, ILT supports the redistribution of the stress on the wall (Di Martino et al., 1998; Hinnen et al., 2005). This effect is important as long as the ILT is intact, but it has been shown that small fractures in the surface of the ILT can propagate to the wall of the aneurysm, concentrating the stress of the focal areas leading to rupture (Gasser et al., 2008).

Stenbaek et al. (2000) (Stenbaek et al., 2000) investigated the increase of relative ILT volume as a potential rupture risk predictor and concluded that a rapid increase may be a better predictor of AAA rupture than an increase in maximal diameter. These results suggest that the geometrical configuration of the ILT relative to the arterial wall may be an influential factor not only on the value of the peak wall stress, but also on its location within the lesion. This observation is in agreement with Wang et al. (Wang et al., 2002) which reports that the incorporation of ILT to the 3D stress analysis models of AAA has a profound influence on the magnitude and distribution of stresses acting on the AAA wall.

In-vitro testing of ILT tissue from AAAs showed found isotropic and almost linear stress strain properties (Di Martino et al., 1998; Gasser et al., 2008; O´Leary et al., 2014; Wang et al., 2001) that gradually change across the radial direction. (Gasser et al., 2010; Wang et al., 2001) Most recent data (O´Leary et al., 2014) identified two distinct ILT morphologies with different mechanical properties: i) A multilayered ILT whose strength and stiffness may either decreases gradually from the luminal to the medial/abluminal layer or decrease abruptly between the luminal and medial/abluminal layer; ii) a single layer ILT, a newly formed thrombus, with a significantly lower strength and stiffness than the multi-layered ILT.

The ILT is modeled as an isotropic hyperelastic material considering two extreme cases: : i) An stiff thrombus tissue named as Type A ILT; and ii) A more compliant thrombus named as Type B ILT. In addition, ILT tissue is regarded isotropic, i.e. the constitutive formulations are independent of the principal anisotropy direction $\mathbf{a_0}$.

For Type A, the SEF proposed by Di Martino and Vorp (Di Martino & Vorp, 2003.):

$$W_{TA} = C_{20}(\bar{I}_2 - 3) + C_{02}(\bar{I}_2 - 3)^2, \qquad \text{(Eq. 7)}$$

where C_{20} and C_{02} are material constants with dimensions of stress and $\bar{I}_2$ the second modified invariant. The reported parameters used were C_{20}=28 kPa and C_{02}=28.6 kPa (Di Martino & Vorp, 2003.).

For the type B ILT, representing a more compliant ILT tissue, the SEF proposed in the study by Gasser et al. (Gasser et al., 2008) is used:

$$W_{TB} = c\sum_{i=1}^{3}(\lambda_i^4 - 1), \qquad \text{(Eq. 8)}$$

where material parameter c=2.11 kPa is the average of the luminal, medial and abluminal ILT (Gasser et al., 2008); λ_i, i =1, 2 ,3 denotes the i^{th} principal stretch, which describes tissue elongation along the i^{th} principal direction. Figure 12 shows the Cauchy stress versus strain for both types of ILT considered.

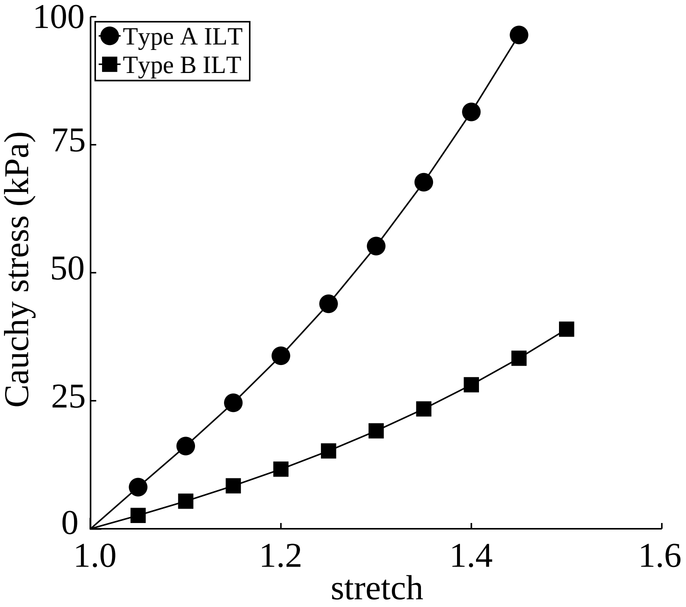

Figure 12. Cauchy stress versus stretch curves for the ILT material models considered in the study

It is to be noted that the SEF for ILT proposed by Di Martino and Vorp, and Gasser et al. are based on uniaxial testing instead of biaxial testing as is the case for the arterial wall. However, previous studies on ILT luminal layer have demonstrated the tissue to be isotropic. As such, uniaxial testing should (theoretically) give the same results than biaxial testing. A comparison of luminal ILT's elastic behavior under uniaxial elongation according to two different constitutive models: i) Gasser et al. (Gasser et al., 2008) (from uniaxial testing) and ii) van de Geest et al. (Vande Geest et al., 2006a) (from biaxial testing) gives the result shown in Figure 13. Given the variability of ILT properties, the mechanical response can be considered the same.

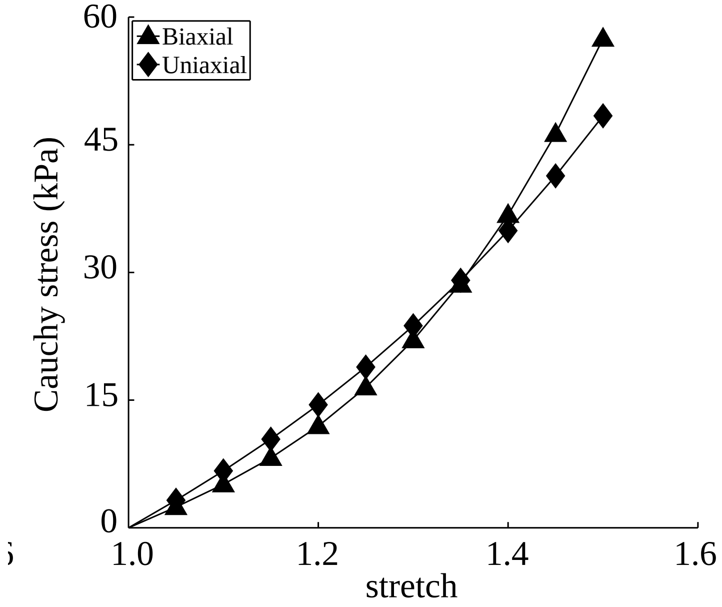

Figure 13. Comparison of luminal ILT's elastic behavior under uniaxial elongation according to two different constitutive models characterized using uniaxial test data (Gasser et al., 2008) and biaxial test data (Vande Geest et al., 2006a).

PATIENT SPECIFIC AAA FINITE ELEMENT MODELS GENERATION

3. PATIENT SPECIFIC AAA FINITE ELEMENT MODELS GENERATION

The 3D computational models are developed through image processing and segmentation of the available CT (Computed Tomography) image slices (resolution of 512x512, average pixel size of 0.769 mm and average slice thickness of 3 mm). Images were reconstructed with specialized software which was applied by an operator with an engineering background and assisted by a radiologist to ensure a proper segmentation of aneurysms. All reconstructed models included ILT and assumed a non-homogeneous aneurysm wall thickness that varied between 1.5 mm at the thrombus-free wall and 1.13 mm at sites covered by a thick (>25mm) thrombus layer (Larsson et al., 2011). Reconstructed surfaces were exported in STereoLithography (STL) file format for further processing.

3.1. AAA Models Generation

Three surfaces were used (which were available from the STL files): the outer wall, the luminal surface, and the inner wall. The outer and inner surfaces determine the aortic wall; whereas the luminal and inner surfaces determine the ILT. With these 3 surfaces a FE model is to be generated in which the elements belonging to the wall and those to the ILT should be differentiated so that the corresponding material properties can be applied. The approached used, which allowed a better convergence during the pull-back algorithm (chapter 5) without losing model quality, was to generate one isotropic and uniform sized mesh from which the elements belonging to the wall were labeled. The labeling was performed by means of a auxiliary mesh created with the outer and inner surfaces, which determine the arterial wall.

The STL file format surfaces from the CT were first treated in Rhinoceros 3D (Robert McNeel & Associates, Seattle. WA), meshed with the ANSYS-ICEM software (ANSYS, Inc., Canonsburg, PA) and exported to the Finite Element analysis software ABAQUS (ver 6.9, Hibbitt, Karlson and Sorensen, Inc., Pawtucker, RI) to generate the FE model. During the meshing process MATLAB (The MathWorks, Inc, Natick, MA) was used to label the elements of the complete AAA mesh, identifying those that are arterial wall and those that are ILT.

3.1.1. Surfaces Preparation

Surfaces in STL file format were imported in Rhinoceros 3D and merged in a single file. The final objective is to generate two volumes. The first volume encloses the whole AAA (outter arterial wall + luminal surface) whereas the second volume comprises the arterial wall only. Figure 14 shows the three surfaces of a typical AAA 3D-model, in red the luminal surface, in blue the inner arterial wall, and in green the outer AAA surface.

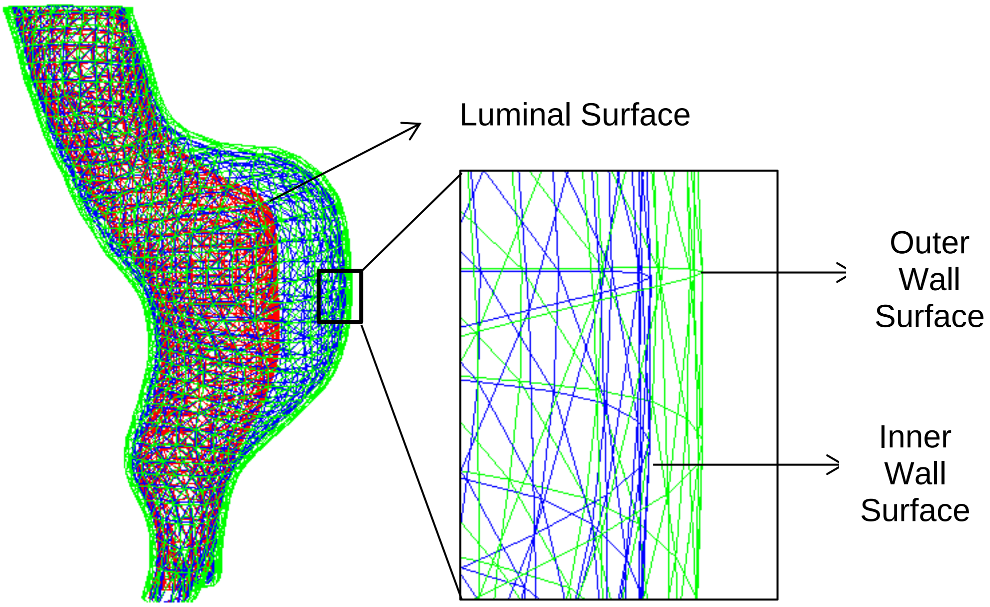

Figure 14. Internal, external and lumen surfaces of an AAA 3D model

As the imported surfaces do not contain top and bottom covers, these are created using 2 parallel surfaces (normal to the AAA axial Axis), as shown in Figure 15a. The covers are created first by trimming the 3 surfaces so that they all start and finish at these two planes (see Figure 15a). Then, the covers are generated for the aorta and the iliacs as shown in Figure 15b,c.

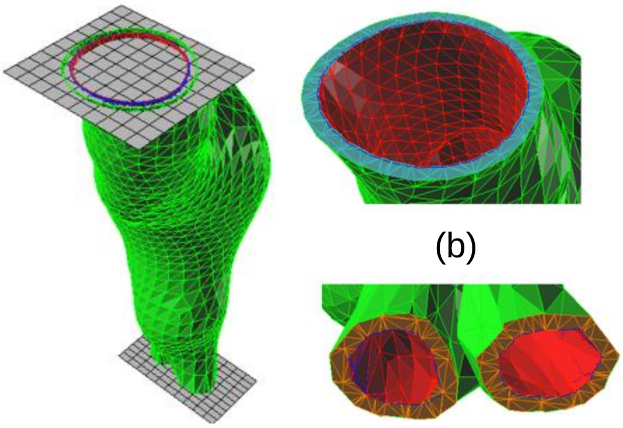

(b)

(a) (c)

Figure 15. Surfaces modelling in Rhinoceros 3D. (a) Planes to cut the surfaces (b) upper cover between external and internal surfaces (c) lower cover between external and internal surfaces for each of the iliac bifurcations

With the surfaces and covers available, the two volumes are create and exported as STL file format to be read in ANSYS-ICEM for meshing.

3.1.2. Meshing

Surfaces sets are imported in ANSYS-ICEM where the two meshes are created. For each set, the lines of the top and bottom covers are extracted from the areas (see Figure 16) so that when the mesh is generated the elements on the covers are forced to lay over these planar surfaces, otherwise ANSYS-ICEM will round it.

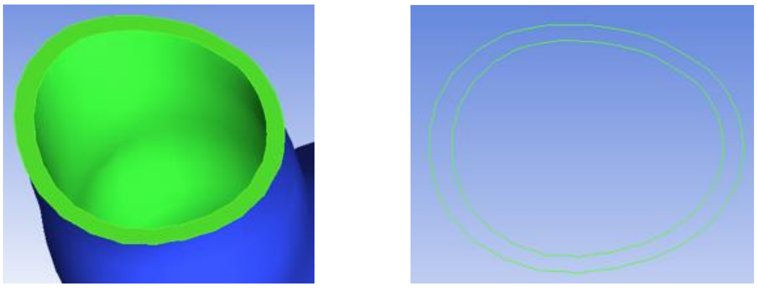

(a) (b)

Figure 16. Lines extracted from the areas. (a) Geometry in ANSYS-ICEM (b) extracted lines from top cover

In the *Part Mesh Setup* options a maximum size element is entered for all part, see Figure 17, looking forward to result in at least 3 elements through the arterial wall (we choose an element size approximately ¼ of the minimum wall thickness).

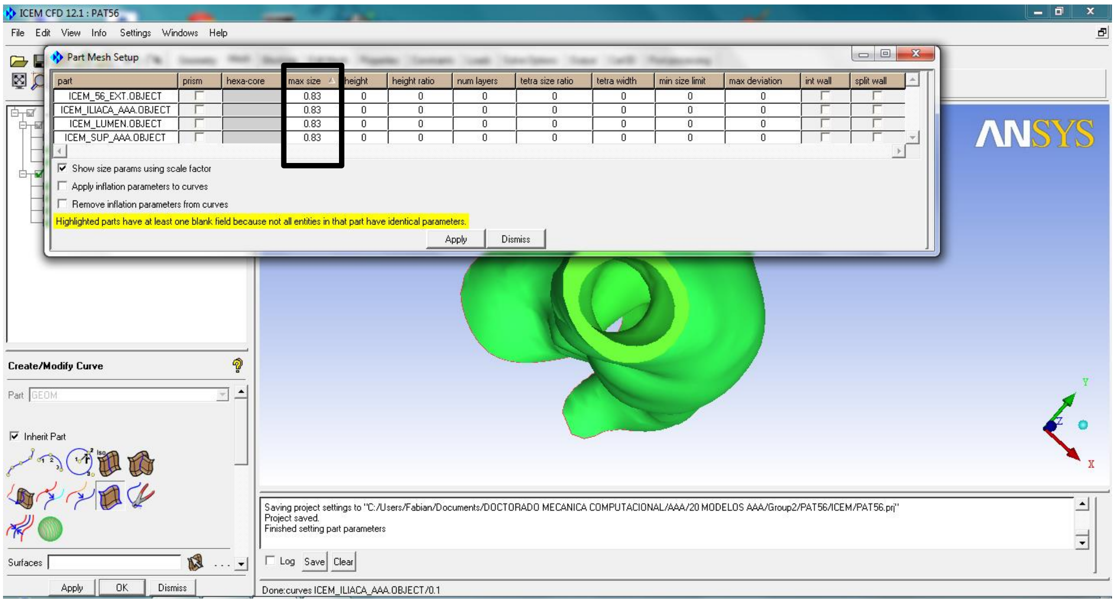

part	prism	hexa-core	max size	height	height ratio	num layers	tetra size ratio	tetra width	min size limit	max deviation	int wall	split wall
ICEM_56_EXT.OBJECT	☐		0.83	0	0	0	0	0	0	0	☐	☐
ICEM_ILIACA_AAA.OBJECT	☐		0.83	0	0	0	0	0	0	0	☐	☐
ICEM_LUMEN.OBJECT	☐		0.83	0	0	0	0	0	0	0	☐	☐
ICEM_SUP_AAA.OBJECT	☐		0.83	0	0	0	0	0	0	0	☐	☐

☑ Show size params using scale factor
☐ Apply inflation parameters to curves
☐ Remove inflation parameters from curves

Highlighted parts have at least one blank field because not all entities in that part have identical parameters.

```
Saving project settings to "C:/Users/Fabian/Documents/DOCTORADO MECANICA COMPUTACIONAL/AAA/20 MODELOS AAA/Group2/PAT56/ICEM/PAT56.prj"
Project saved.
Finished setting part parameters
```

Done:curves ICEM_ILIACA_AAA.OBJECT/0.1

Figure 17. Mesh setup in ANSYS-ICEM

The two meshes (AAA and arterial wall) are created following this same procedure for each one, and the solid meshes are then exported to Abaqus format (a text file) so that they can be read in MATLAB for labeling. The meshing algorithm used by ANSYS-ICEN generates fairly uniform meshes in the volume (elements of approximately same size), a characteristic that is desirable for the finite element computations, in particular for the application of the pull-back algorithm described in the following chapters.

3.1.3. Labeling

A MATLAB code was developed to label elements belonging to a portion of a body from the whole model. As an input it reads the elements (number and connectivity) and nodes (number and coordinates) corresponding to the volume meshes just generated. The code finds out which elements correspond to the wall and then label it as arterial material. The ILT is determined as material omission. For convenience and simplicity elements are renumbered so that all elements belonging to the wall are consecutive and starting from one, with the elements following. The labeling code outputs the labeled mesh in ABAQUS format.

3.1.4. FEM model generation

The labeled mesh is opened in ABAQUS. Figure 18 shows the labeling result of an AAA model, a Solid Section is assigned to the arterial wall and another to the ILT, and material model and properties are assigned to each of these Solid Sections.

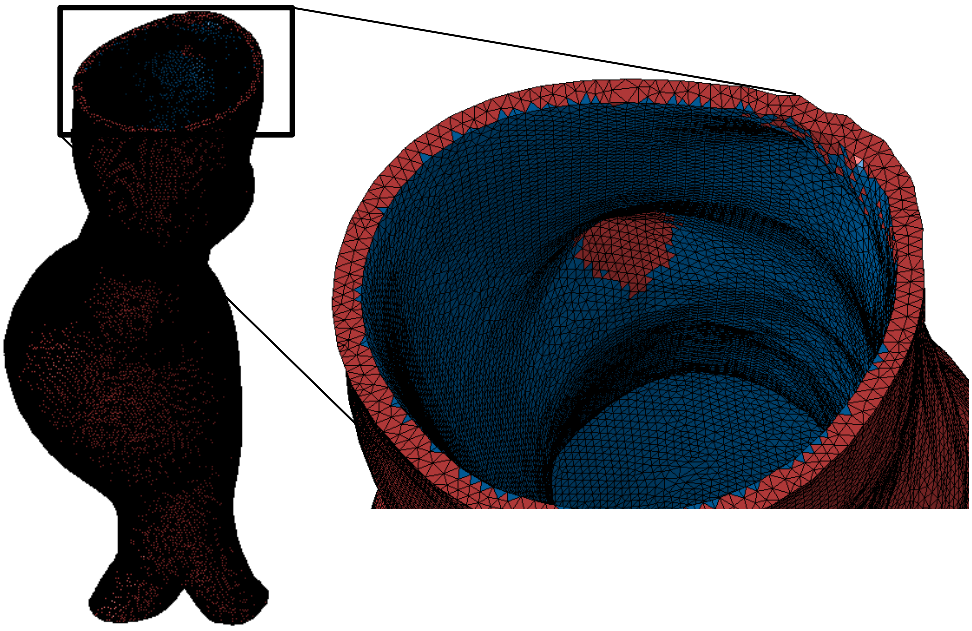

Figure 18. Labeled AAA mesh in ABAQUS

The constraints due to the thoracic aorta and common iliac arteries were simulated by restraining the longitudinal displacement (Figure 19a) while allowing displacements in the radial direction (Figure 19b). Finally, The blood pressure was applied to the luminal surface of the AAA.

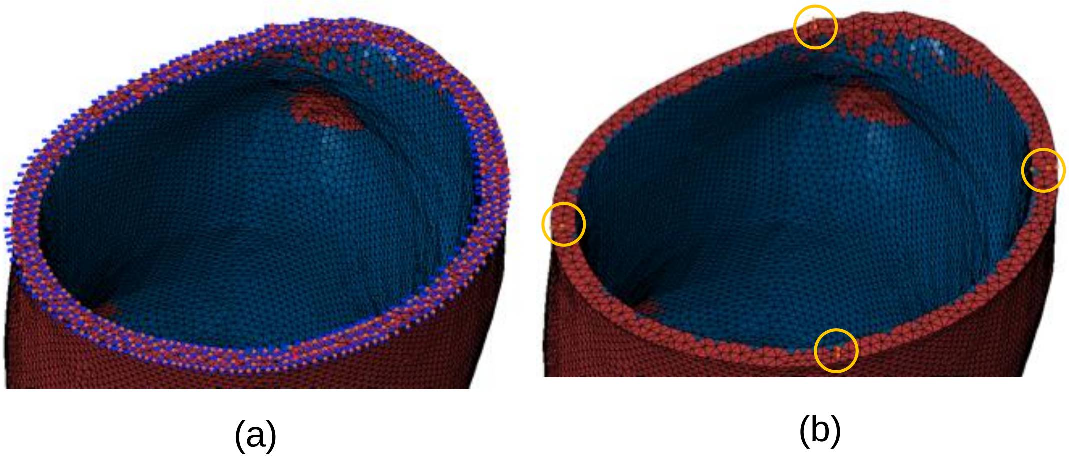

Figure 19. Displacement restraints applied to AAA models. (a) Axial displacement restriction (b) restrictions to allow radial displacement

It is noted that the aneurysmal models consider uniform mechanical properties for the arterial wall and the ILT, and no distinction were made between the aneurysm and the adjacent vasculature. A refined model should consider the variation in the mechanical properties between the arterial and aneurysmal tissues since otherwise stress concentrations would appear at the interfaces.

3.1.5. Direction of anisotropy

The assessment of the direction of anisotropy has been performed following the procedure proposed by Alastrue et al. (Alastrué et al., 2006.). In this procedure, the model is subjected to a sub-diastolic pressure using the isotropic material model described by Eq. (5) for the arterial wall and by Eq. (7) for the ILT. Then, the direction of anisotropy is made coincident with the direction of maximum principal stress. The result obtained when this procedure is applied is a dominant circumferential direction of the fibers shown in Figure 20 for two typical models.

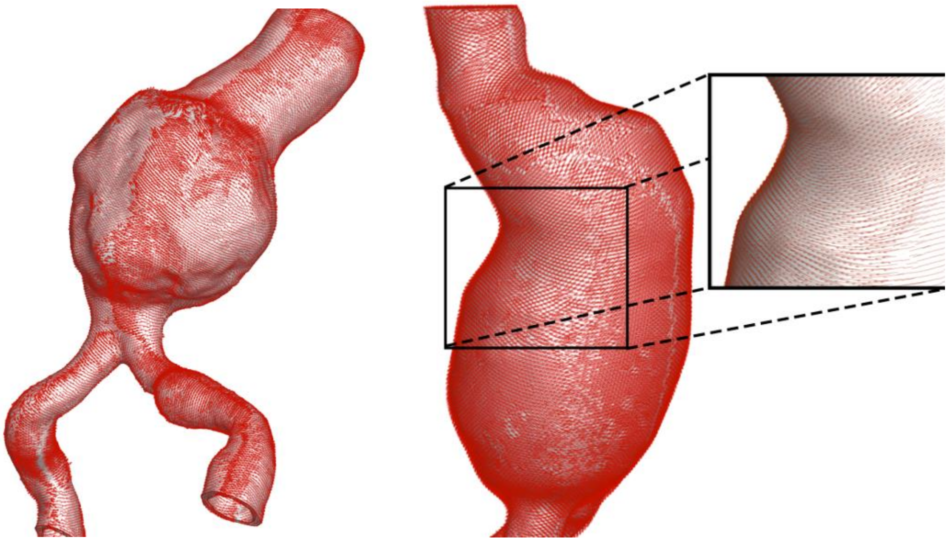

Figure 20. Circumferential direction on two typical AAA models. Circumferential directions were obtained according to the procedure proposed in Alastrue et al (Alastrué et al., 2006.).

3.2. *Material Model Implementation*

The isotropic and anisotropic material models for the arterial wall were implemented in the material user subroutines UHYPER (for the isotropic material model) and UANISOHYPER_INV (for the anisotropic material model) within the finite element software ABAQUS. These subroutines are shown in Appendix D for the Isotropic and Appendix E for the Anisotropic model.

3.3. *Mesh sensitivity analysis*

In order to test the quality of the mesh used for the calculations, a sensitivity analysis was performed on a typical AAA model subject to diastolic pressure. Table 3 shows the peak principal stress (PWS) in the AAA wall for different mesh densities.

Table 3. Predicted peak principal stress (PWS) in the AAA wall for the model. Results for different meshes are shown, where NE denotes the number of elements. Change in PWS, $\Delta\mathbf{PWS}$, is computed between two consecutive mesh densities.

NE	PWS (kPa)	ΔPWS (%)
149,949	260	--
300,845	305	14.8
446,726	300	-1.7
815,588	310	3,2

As these results demonstrate, for meshes with more than 300000 elements, the maximum principal stress changes less than a 3% with respect to the finest mesh used, while giving a sufficient number of elements through the arterial wall as shown in Figure 21 (a minimum of three elements at any section of the model). Therefore, in the following, all models have been meshed using a minimum element size equal to one-fourth of the minimum arterial wall thickness which guarantees the required mesh quality.

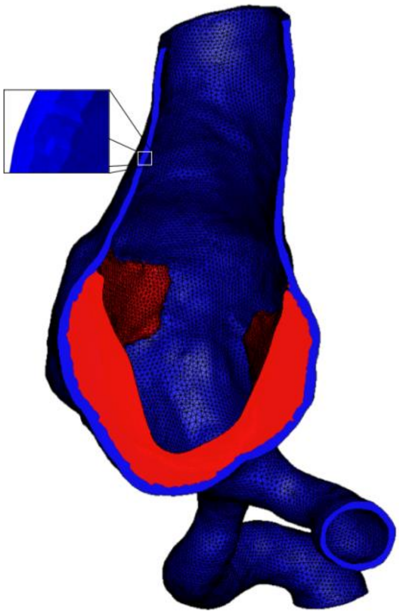

Figure 21. Finite element meshes for a typical AAA model (inset shows a detail of the wall mesh).

PULLBACK ALGORITHM

4. PULLBACK ALGORITHM

The reconstructed AAA geometry from CT images is pressurized, and hence, it is not the zero-pressure configuration. Specifically, for most CT modalities, the geometry seen in the images refers to the configuration that is subjected to the diastolic blood pressure. Assuming this geometry as the zero-pressure configuration, as is frequently done, leads to inaccurate deformations and stresses, and therefore may misled the calculation of the AAA rupture risk. Consequently, recent studies (De Putter et al., 2006; Lu et al., 2007; Raghavan et al., 2006; Speelman et al., 2009) introduced a hypothetical zero-pressure configuration, which in turn serves as the reference for biomechanical simulations. Specifically, a more realistic computation of the PWS should consider such a zero-pressure geometry.

When loading the zero-pressure configuration with the diastolic blood pressure, the deformed AAA is thought to match the AAA geometry seen in the CT images as in Figure 22. This constraint implicitly defines the shape of the zero-pressure configuration. A number of alternatives have been presented to solve this problem (De Putter et al., 2006; Lu et al., 2007; Raghavan et al., 2006).

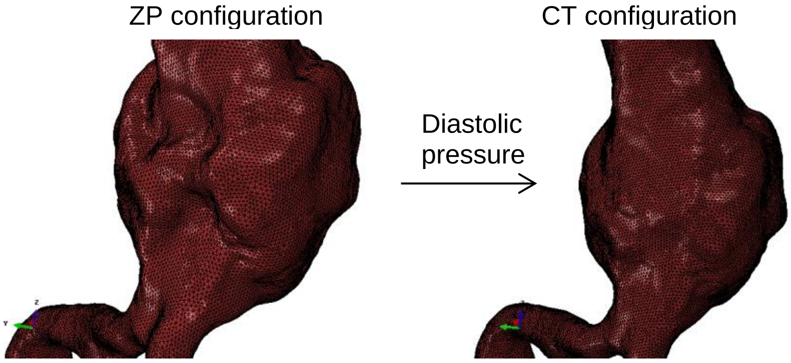

Figure 22. ZP and CT based configuration of an AAA with ILT

One approach relies on inverse elastostatic methods. These methods were first introduced by Shield (Shield, 1967) for elastically homogeneous materials and zero body forces and later generalized for elastic materials of any grade by Carlson (Carlson, 1969.). Later, Chadwick (Chadwick, 1975) exploited the duality property demonstrated by Shield to formulate Shield's equilibrium equations in terms of Eshelby's energy-momentum tensor. These results were further re-examined by Godvinjee and Mihalic (Gasser et al., 2008; Govindjee & Mihalic, 1996) in order to provide a more suitable finite element formulation. This formulation involved minor changes to elements designed for traditional finite element analysis, and could be applied to nearly incompressible materials. The formulation proposed by Godvinjee and Mihalic was applied by Lu et al (Lu et al., 2007) to find the zero-pressure configuration of AAAs. It is noted that the inverse method requires manipulations on the finite element matrices, which makes its application difficult when dealing using commercial finite element solvers.

In addition, many of the reported approaches to compute the zero-pressure configuration considered shell models of the AAA geometry (Lu et al., 2007; Raghavan et al., 2006), and all of them investigated only isotropic aneurysm wall models. Most severely, none of the reported studies accounted for an intraluminal thrombus (ILT) when predicting the zero-pressure configuration. However, an ILT is seen in almost all clinical relevant AAAs (Hans et al., 2005). This chapter presents an algorithm to determine the zero-pressure geometry of an AAA and overcomes the above mentioned limitations. Specifically, the proposed methodology accounts for the wall’s anisotropy and the presence of the ILT. The algorithm is a modification of the method proposed by Raghavan et al. (Raghavan & Vorp, 2000), which continuously updates the zero pressure geometry based on the displacement field rather than on an incremental upgrading of the deformation gradient, as proposed by de Putter et al. (De Putter et al., 2006). The proposed approach offers some numerical advantages with respect to the methodology proposed by de Putter et al. Most important, computations always start from an updated reference configuration, instead from an initially deformed configuration, such that the proposed methodology avoids using very small increments at the initial steps. This leads to numerical efficiency through fast convergence. The proposed method has been implemented on commercial finite element analysis software ABAQUS (ver 6.9, Hibbitt, Karlson and Sorensen, Inc., Pawtucker, RI) using solid meshes for both the AAA wall and the ILT.

4.1. Zero-pressure geometry algorithm

The algorithm to reconstruct the zero-pressure geometry of an AAA model from the CT image based geometry is explained in the following. The main purpose of this algorithm is to find the zero-pressure configuration, i.e. a reference configuration that deforms into the geometry $\mathbf{X}_{image}$that is seen in the CT images when subjected to the diastolic pressure, P_{diast}. The proposed algorithm keeps the mesh connectivity unchanged and iteratively updates the nodal coordinates. When working with the anisotropic material, the local circumferential direction is also consistently pulled-back to the zero-pressure configuration. The iterative algorithm is outlined in Figure 23, where *B* denotes a configuration of the AAA.

```
Given: $\mathbf{X}_{image}$, circumferential direction ($\mathbf{n}$),
       $tol$, $\max_{iter}$, $f_{aniso}$
Initialize: $k := 1$, $\mathbf{X}_Z^0 := \mathbf{X}_{image}$
Repeat
    i)   Find $\mathbf{X}_{def}^k$ from:
         $\boldsymbol{\nabla} \cdot \boldsymbol{\sigma} = \mathbf{0}$ in $B^{k-1}$
         $\boldsymbol{\sigma} = 2\frac{1}{J}\mathbf{F}\frac{\partial W}{\partial \mathbf{C}}\mathbf{F}^T$
         $\mathbf{u} \mid_{\partial B_t^{k-1}, \partial B_b^{k-1}} = \bar{\mathbf{u}}$
         $(\boldsymbol{\sigma} \cdot \mathbf{m}_i) \mid_{\partial B_i^{k-1}} = P_{diast}$
    ii)  Update zero-pressure geometry
         $\mathbf{X}_Z^k := \mathbf{X}_Z^{k-1} + (\mathbf{X}_{def}^k - \mathbf{X}_{image})$
    iii) Fiber pull-back
         if $f_{aniso} == 1$ then
             $\mathbf{F}^k := \frac{\partial \mathbf{X}_{image}}{\partial \mathbf{X}_Z^k}$
             $\mathbf{n}^k := (\mathbf{F}^k)^{-1}\mathbf{n}$
         end if
    iv)  Error
         $error = \|\mathbf{X}_{def}^k - \mathbf{X}_{image}\|_\infty$
    v)   $k := k + 1$
Until ($error \leq tol$ and $k < \max_{iter}$)
```

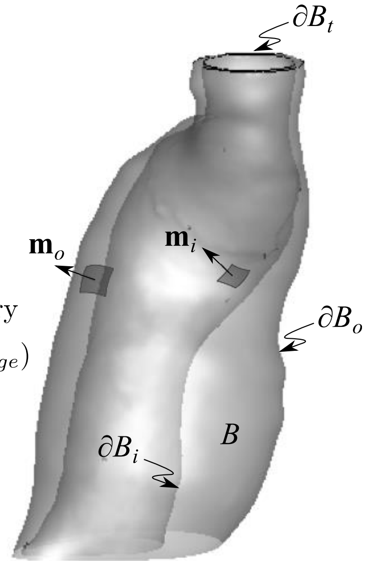

Figure 23. Zero-pressure geometry algorithm. The algorithm continuously updates the reference configuration of the AAA until the difference between the original CT-image and the deformed configuration obtained from the current zero-pressure geometry, $\mathbf{X}_{def}^k$, is less than a prescribed tolerance, *tol*.

The initial zero-pressure configuration B_0 corresponds to the geometry that was reconstructed from the CT image, $\mathbf{X}_{image}$, where $\mathbf{X}$ represents a $N_n \times 3$ matrix that stores the nodal coordinates of the finite element mesh. Here, N_n denotes the total number of mesh nodes, and for an anisotropic material model (f_{aniso}=1) the circumferential direction is also provided at the element level. Now, the iterative algorithm starts and the zero-pressure configuration is updated until the error norm, i.e. the absolute maximum nodal distance between $\mathbf{X}_{image}$ and the deformed configuration from inflating the current zero-pressure configuration, $\mathbf{X}_{def}$, is less than a prescribed tolerance tol.

Step i: At the k-th iteration, an elastic problem is solved that considers the k-1-th zero-pressure geometry as its stress-free reference configuration. Constitutive relations and boundary conditions apply as described in the previous chapter.

Step ii: When the elastic problem is solved, the k-th zero-pressure geometry is computed by adding the difference $\mathbf{X}_{def}^{k} - \mathbf{X}_{image}$ to the k-1-th zero-pressure geometry.

Step iii: When using an anisotropic constitutive model ($f_{aniso}=1$), the circumferential direction is pulled-back to the k-th zero-pressure configuration, i.e. $\mathbf{n}^k = (\mathbf{F}^k)^{-1}\mathbf{n}$ with the deformation gradient $\mathbf{F}^k := \frac{\partial \mathbf{X}_{image}}{\partial \mathbf{X}_Z^k}$.

Step iv: The error norm is computed, and if it is less than tol, or the number of iterations is greater than the maximum allowed, $\max_{iter}$ the iteration is terminated.

Step v: The iterator k is incremented.

4.2. Computational Validation

The proposed algorithm has been validated using an idealized geometry (anisotropic cylinder) and a patient specific geometry.

4.2.1. Cylindrical tube

For the cylindrical geometry, because of the symmetry, only a quarter of the cylinder was considered. The problem was set-up such that its zero-pressure configuration corresponded to a cylinder of 20 cm length, an external diameter of 8cm, and a uniform wall thickness of 0.5cm. A quarter of the cylinder was discretized with 15700 linear tetrahedral elements, and the arterial wall was assumed to be anisotropic with the circumferential direction being stiffer. Specifically, the following Strain Energy Function (SEF) defined by Eq. 6 was used with the material parameters given in Table 2.

The pressurized geometry, $\mathbf{X}_{image}$, was then obtained by inflating the cylinder with a pressure of 10.6 kPa (80 mmHg). Figure 24 shows the pressurized and the zero-pressure geometries.

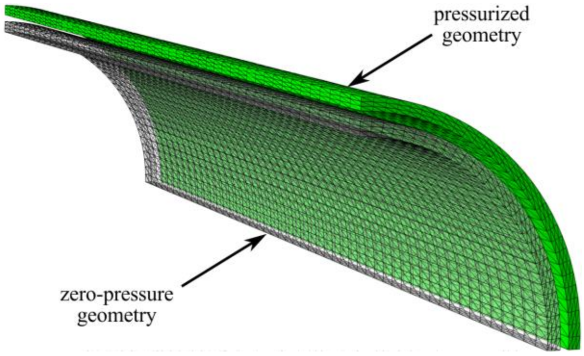

Figure 24. Idealized geometry used to validate the algorithm to compute the zero-pressure geometry. The cylinder in green corresponds to the pressurized geometry used as input information to compute the zero-pressure geometry. The wireframe corresponds to the zero-pressure geometry identified by the algorithm.

The algorithm's tolerance was set to 0.003 cm, i.e. less than 0.1% change in the actual external diameter. The algorithm requires five iterations to reach the desired tolerance (see Figure 25). The algorithm converged remarkable fast; already after the second iteration the error is less than a 0.15%. However, this behavior is in part due to the symmetry of the model problem.

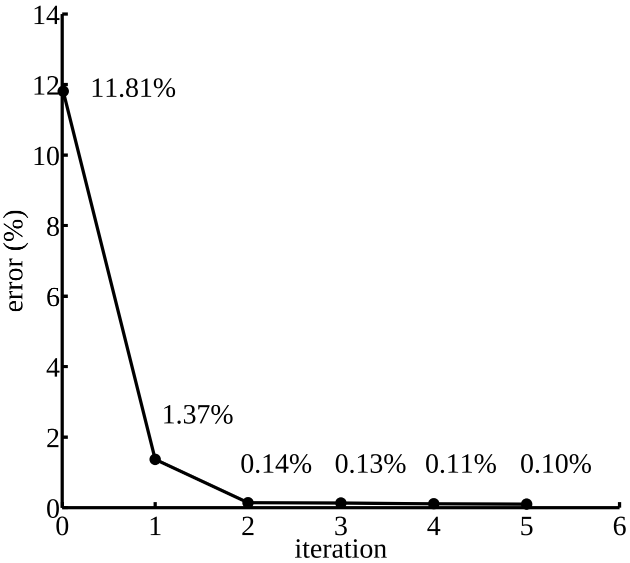

Figure 25. Convergence plot for the idealized geometry. The algorithm takes five iterations to reach the required tolerance (0.1%). Already, after the second iteration the error is less than 0.2%.

4.2.2. Patient specific AAA geometry

A second computational validation of the algorithm was performed using a model of an AAA (model B12 in Table 3). The following procedure was followed to validate the algorithm:

i. The model, which is a CT based image, is considered as the ZP configuration.
ii. The diastolic pressure is applied to this model. The obtained geometry is considered as the CT based image.
iii. The ZP algorithm is applied to the geometry obtained in step ii to retrieve the original geometry.

This procedure was applied to a typical AAA model (see Figure 25) including the ILT and also removing the ILT from the model (just arterial wall). For the arterial wall the isotropic SEF given by Equation 5 and material parameters from Table 2 were used. For the ILT the SEF described by Equation 7 with the material parameters given in chapter 2 was used.

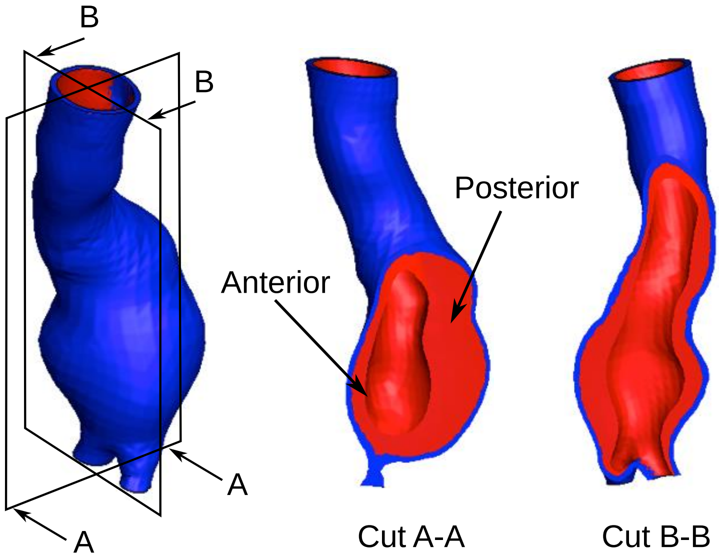

Figure 26. Typical AAA model: Geometry and ILT distribution

4.2.3. Arterial wall only

The ZP algorithm was applied until the maximum nodal distance $\mathbf{X}_{def}^{k} - \mathbf{X}_{image}$ was below 0.09 mm. Convergence to the zero pressure geometry was achieved after 12 iterations. Figure 27 shows the maximum and mean nodal distance for each iteration compared to the ZP configuration. For the last iteration the maximum nodal distance to the ZP configuration was found to be 0.09 mm and the mean nodal distance 0.021 mm.

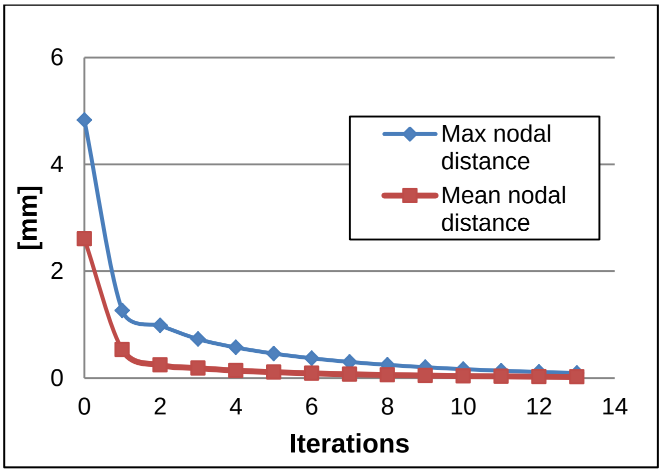

Figure 27. Convergence of the Pull-Back algorithm for the AAA model without the ILT. Maximum and mean nodal distance between the identified and the actual ZP configuration.

Figure 28 shows the evolution of the zero pressure configuration along the iterative process. As in the case of the cylinder most of the correction takes place in the first iterations of the algorithm.

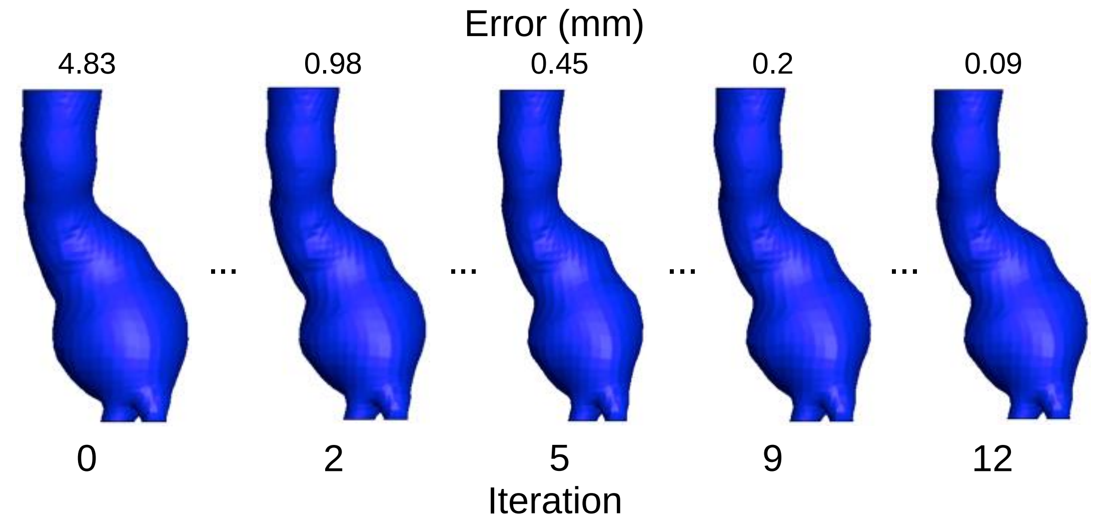

Figure 28. Evolution of the zero pressure configuration for the AAA model without the ILT.

The convergence of the algorithm is also depicted in Figure 29, which shows the evolution in the position of the element with the maximum error through the iterations. The figure clearly shows how the element approaches to the position in the actual ZP configuration as the iterations progress. We can see that most of the correction has taken place in the first three iterations of the algorithm.

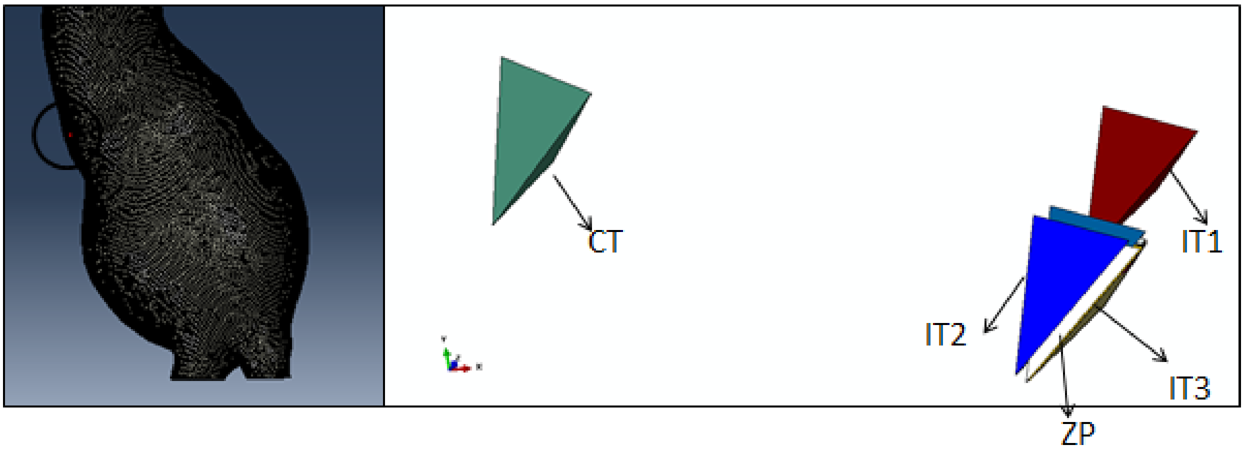

Figure 29. Convergence of the element with maximum error for the AAA model without the ILT.

4.2.4. Whole model

As the presence of ILT stiffens the AAA and this model in particular has a thick ILT, the initial maximum nodal distance between the ZP and CT configuration was found to be smaller, in this case 2.89 mm (instead of 4.83 mm for the model with no ILT).

A maximum nodal distance $\mathbf{X}_{def}^{k} - \mathbf{X}_{image}$ below 0.02 mm was achieved in the fifth iteration, and by the seventh iteration the maximum error was less than 0.008 mm. Figure 30a shows the convergence plot of the algorithm. As in the previous case, the maximum and mean nodal distances at each iteration are depicted. Figure 30b shows the evolution of the geometry through the iterations, in this case being the initial displacement half compared to when ILT was not included the geometric differences are very small.

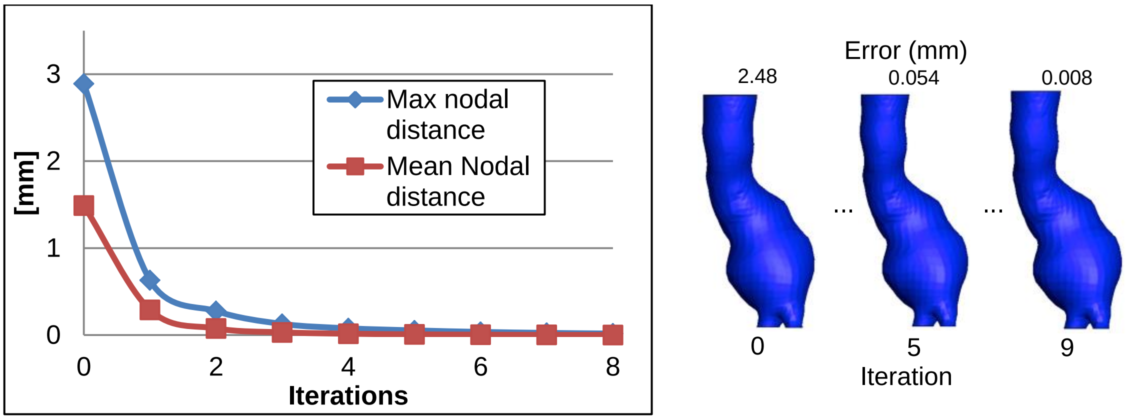

(a) (b)

Figure 30. Convergence of the Pull-Back algorithm for the AAA model (whole model): a) Maximum and mean nodal distance between the identified and the actual ZP configuration; b) Evolution of the zero pressure configuration for the AAA model (whole model).

Figure 31 shows the evolution of the element with the maximum error through the iterations. As in the previous case, the figure shows that most of the correction in the ZP configuration occurs within the first three iterations. In fact, for this particular case, at the third iteration, the maximum absolute error between both configurations is less than 0.7 mm.

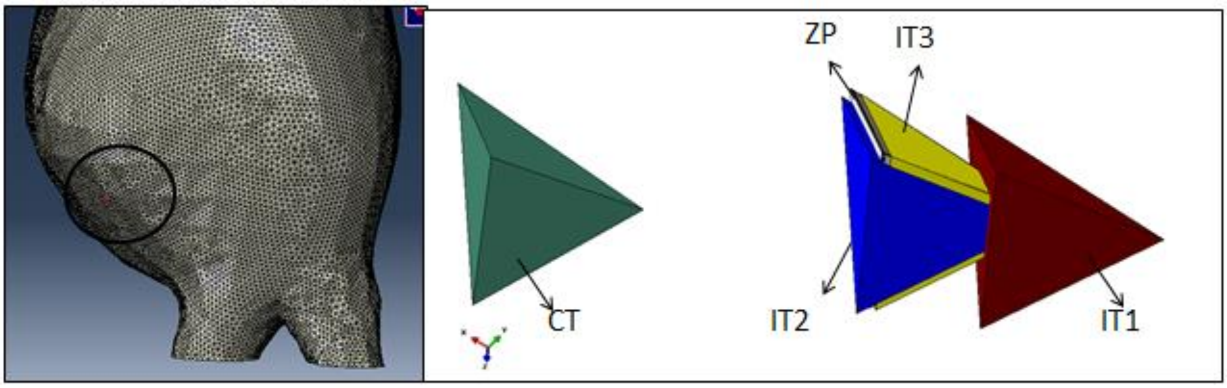

Figure 31. Convergence of the element with maximum error for the AAA model (whole model).

Another interesting finding during the numerical validation of the algorithm was that the iterative procedure was also found to be globally volume preserving for both, the isotropic and the anisotropic material behavior. Table 4 shows the percentage difference between the volumes of the final zero pressure and the CT-based geometries for the AAA model (column identified as AAA model 1). The algorithm was applied to an additional patient specific AAA model (column identified as AAA model 2 in Table 4) to demonstrate this observation. The observed changes are negligible.

Table 4. Percentage volume change between the zero pressure and CT-based geometries.

	AAA Model 1		AAA Model 2	
	Isotropic	Anisotropic	Isotropic	Anisotropic
Percentage volume difference	0.02%	0.04%	-0.008%	-0.029%

4.3. *Experimental Validation*

In collaboration with the Vascular Biomechanics and Biofluids Laboratory at the University of Texas San Antonio, an experimental validation of the proposed Pull-Back algorithm has been performed. This section describes the methodology and main results of this effort.

4.3.1. Material & Methods

To a phantom model of idealized axisymmetric abdominal aortic aneurysm (AAA) geometry (Figure 32a) was applied the proposed algorithm on the pressurized configuration of this phantom to reconstruct the zero pressure (ZP) geometry. The strategy was to: 1) obtain micro CT images of the AAA phantom at unpressurized (0mmHg) and pressurized conditions, the latter with internal pressures of 80 mmHg, 120 mmHg and 140 mmHg; 2) develop image based models and meshes from micro CT image data; 3) apply the proposed algorithm to the pressurized geometry to reconstruct the ZP geometry; and 4) compare and validate the reconstructed ZP geometry with the CT image based geometry obtained at the unpressurized condition. A schematic of the experimental setup is shown in Figure 32b.

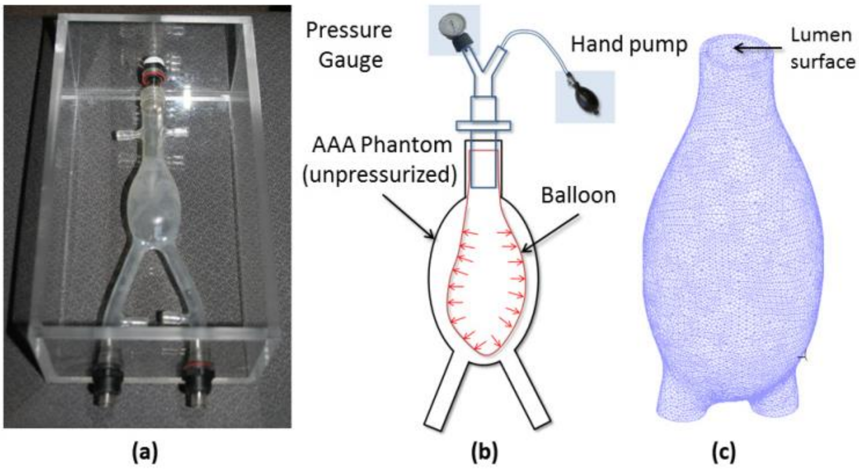

Figure 32. a) Phantom replica of AAA; b) Schematic diagram of experimental setup for zero pressure algorithm validation; c) Image based computational geometry of AAA phantom with hexahedral mesh used for structural simulations.

The phantom was developed using a silicone elastomer with a modulus of elasticity, E =1170 kPa. The measured average wall thickness was 0.1365 cm, the maximum aneurysm diameter was 4.7 cm and total length of the phantom was 26 cm. As shown in the schematic (Figure 32b), a balloon (initial thickness = 0.02 cm) was inserted into the AAA phantom and pressurized using a hand pump until the desired intraluminal pressure was achieved in the aneurysm sac, monitored using a pressure gauge. The phantom was then inserted into a μCT scanner (Skyscan 1076 in vivo scanner, Bruker Corporation, MA) and imaged at the unpressurized condition (0 mmHg) and then repeated for the three different pressurized conditions (80 mmHg, 120 mmHg, and 140 mmHg). The scan resulted in 2,996-3,010 images with a pixel resolution of 35 μm and slice spacing of 35 μm. Scanned images were obtained as image files (.png), which were then converted to DICOM files before the commercial software Mimics (Materialize NV, Belgium) was used for automatic segmentation and lumen surface generation. An in-house code called 'AAAMesh' was then used to develop the mesh with hexahedral elements (Figure 32c). A uniform wall thickness of 1.365 mm was assumed for these models during mesh generation. The element size was optimized through a mesh sensitivity study, which resulted in a mesh size in the range 40,242 - 41,952.

The pressurized phantom meshes were subject to the pull-back algorithm for reconstruction of the ZP geometry. The structural simulations performed with the finite element solver ADINA 8.8 (Adina R&D Inc., Watertown, MA). Although the phantom wall and the balloon form a composite laminate structure, the effective Young's modulus calculated using classical mechanics did not change significantly (1,171 kPa), given the relatively thin balloon compared to the phantom's wall thickness. For each of the pressurized meshes, the iterative algorithm was executed until the iteration error was less than 0.5%. The lumen surface of the ZP geometries was then compared with the lumen surface of the AAA phantom at the unpressurized condition, qualitatively and quantitatively. The relative matching of lumen surfaces was visualized using a part comparison feature in 3-Matic (Materialise NV, Belgium). A directional Hausdorff distance (D_H) was further calculated between the nodes of the two lumen surfaces to quantify the mismatch. D_H is a measure of closeness between two sets of points (e.g., P and Q). Intuitively, D_H finds the point p (from set P) that is furthest from any point in set Q and measures the distance from p to its nearest neighbor in Q. However, this calculation was performed from P to Q and again from Q to P and the maximum of those two values is reported as D_H.

4.3.2. Results

The ZP algorithm was applied to the three pressurized phantom meshes (at 80mmHg, 120 mmHg, and 140 mmHg) and the algorithm converged in 6, 7 and 8 iterations, respectively (see Figure 33a).

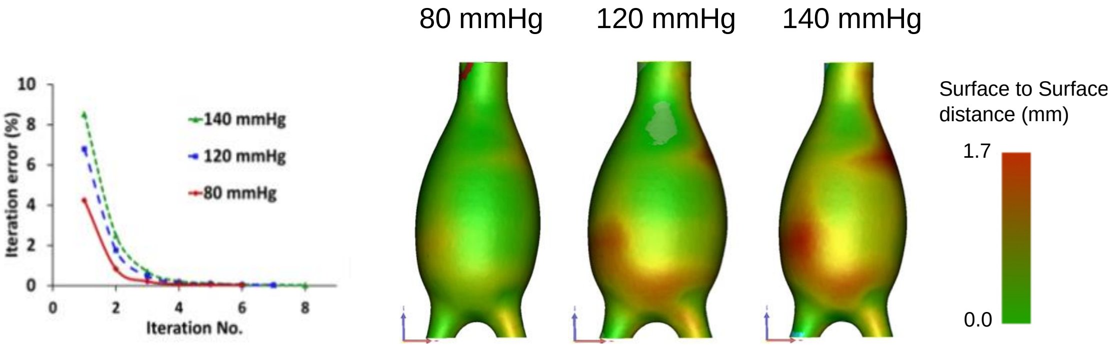

(a) (b)

Figure 33. a) Convergence of ZP algorithm applied to phantom geometries pressurized at 80, 120 and 140 mmHg; b) front view and c) right view of superimposed lumen surfaces of ZP geometry/80mmHg and Phantom@0mmHg; d) spatial distribution of nodal distances between the two surfaces (red represents maximum distance).

The maximum deviation (D_H) was 2.6% of the maximum aneurysm diameter when the loading was 80 mmHg gauge, and increased to 3.5% and 3.9% for 120 mmHg and 140 mmHg gauge, respectively. Figure 33b shows a qualitative visualization of the surface to surface distances; the deviation is small throughout the AAA sac with the exception of the distal region of the anterior wall. The reason for this discrepancy is due to three factors mainly. First, while applying the intraluminal pressure loading to the AAA phantom with a balloon, only the aneurysm sac was subjected to the pressure during the μCT scan, thus the region distal to the aorto-iliac bifurcation shows shrinkage in the predicted unloaded geometry. However, the unloaded phantom geometry was found to be insignificantly smaller, in volume, than the actual unloaded geometry, which is likely due to the nearly incompressible material model used for the FEA simulations in the iterative algorithm. Secondly, there may be a slight discrepancy in the material properties of the silicone elastomer used for the AAA phantom and those that characterize the specimens used for planar biaxial tensile testing, since the production lots were different. Moreover, the

AAA phantom could have hardened over time until it was used in the scanner, as hardening is common among elastomers. Third, it was noted that during the experiments the phantom was in contact with the CT scanner tray during the scanning process. In the structural simulations the inlet and outlet boundary nodes were fixed, therefore nodal displacements in the sac region was forced to be uniform on all sides. Therefore, it is believed that the contact of the phantom with the tray led to the mismatch between the actual and predicted ZP geometries in the anterior surface of the phantom as shown in Figure 33b.

EFFECT OF THE ZERO PRESSURE GEOMETRY ON THE AAA RUPTURE RISK

5. EFFECT OF THE ZERO PRESSURE GEOMETRY ON THE AAA RUPTURE RISK

Although the criterion for AAA repair varies in practice, the maximum diameter is the most frequently used clinical AAA repair indication. However, the diameter criterion is under controversial discussion since only 25% of AAAs rupture in a patient´s lifetime (Brown & Powell, 1999). Consequently, small AAAs (<5.5cm) rupture and large AAAs (>5.5cm) remain stable, whereas surgical interventions continue to pose serious risk especially in elder patients. Therefore, alternative rupture risk indices have been proposed in order to target patients that require AAA repair. Specifically, biomechanical parameters like peak wall stress (PWS) or peak wall rupture risk (PWRR) have shown to be a feasible an promising alternative that can be used to better ascertain the risk of rupture. The computation of such parameters requests (i) accurate methods for reliable reconstruction of the aortic geometry, (ii) appropriate material properties for the aneurysmatic tissues, and (iii) realistic (physiological) boundary conditions, and (iv) along with adequate numerical methods must be developed to solve the biomechanical problem. The objectives of this chapter are two fold. To quantify the impact of the material formulation of the arterial Wall i.e., isotropic versus anisotropic behavior, and to study the influence of the unloaded geometry on the predicted values of the PWS in the arterial wall, and therefore on the PWRR.

5.1. Methods

5.1.1. Patient specific models

For this study twelve non-ruptured patient-specific abdominal aortic aneurysm geometries were considered. The term non-ruptured is used in the context that all CT images were acquired following a standard imaging protocol before the subjects underwent repair or during the surveillance period after diagnosed with AAA. Two of these models, named A1 and A2, were obtained from medical images at Allegheny General Hospital (Pittsburgh, PA) from asymptomatic subjects who were eligible for elective endovascular repair. The 3D computational models were developed through image processing and segmentation of the available CT image slices (resolution of 512x512, average pixel size of 0.769 mm and average slice thickness of 3 mm). The DICOM formatted CT images were imported in the ScanIP module of Simpleware^{TM} (Exeter, UK) for segmentation. A semi-automatic methodology (Shum et al., 2010) was followed to segment and create the masks for the three domains (i.e. lumen, ILT and AAA wall). Ten additional non-ruptured AAA geometries, named B1 to B10, were acquired at two hospitals in Stockholm, Sweden. All AAA images provided a sufficiently high out-of-plane resolution of the image data and a good identification of the exterior aneurysm surface. Local ethics committee approved the collection and use of anonymized data from human. Aneurysms B1 to B10 were reconstructed with the diagnostic software A4research (VASCOPS GmbH, Graz, Austria), which was applied by an operator with engineering background assisted by a radiologist to ensure proper segmentation of the aneurysms. Details regarding the image segmentation process are given elsewhere (Auer et al., 2010). All reconstructed models include the ILT and assumed a non-homogeneous aneurysm wall thickness varying between 1.5 mm and 1.13 mm at the thrombus-free and covered sites respectively.

All surface geometries were exported in STereoLithography (STL) file format and meshed following the procedure explained in Chapter 3. The total number of elements per AAA model ranged between 430k and 1000k elements, and had at least three elements through the arterial wall thickness in order to capture the stress gradients through the wall. Table 5 show the main characteristics of the aneurysms considered in the study.

5.1.2. Material model and boundary conditions

The aneurysmal wall tissue was modeled using isotropic and anisotropic hyperelastic material models. For the case of isotropy, the material response of the aneurysm wall tissue was characterized by Demiray´s SEF (Demiray, 1972), Equation 5, whereas for the case of anisotropy the SEF given in Equation 6

(Rodriguez et al., 2008), was used. The material parameters are given in Table 2. The ILT was modeled as an isotropic hyperelastic material considering the SEF proposed by Di Martino and Vorp (Di Martino & Vorp, 2003.) given in Equation 7. The corresponding material parameters can be found in Chapter 2. The isotropic and anisotropic material models for the arterial wall were implemented in the material user subroutines UHYPER (for the isotropic material model) and UANISOHYPER_INV (for the anisotropic material model) within the finite element software ABAQUS.

Table 5. Characteristics of the twelve patient-specific AAA models.

Model	Max diameter (cm)	Max ILT thickness (cm)	Arterial wall elements	ILT elements	Total elements
A1	5.1	1.1	322,228	110,985	433,213
A2	5.0	1.8	247,850	198,876	446,726
B1	5.1	2.0	354,865	181,423	536,288
B2	4.2	1.1	336,766	242,191	578,957
B3	5.1	1.4	285,509	291,834	577,343
B4	5.0	2.1	287,576	199,300	486,876
B5	5.4	0.9	346,193	288,170	634,363
B6	5.1	2.4	308,788	239,911	548,699
B7	4.4	0.2	368,482	243,630	612,112
B8	4.8	2.1	338,181	213,913	552,094
B9	5.1	2.1	333,169	279,490	612,659
B10	4.7	1.0	292,151	282,051	574,202
Mean ± SD	4.9±0.3	1.5±0.7			

The constraints due to the thoracic aorta and common iliac arteries were simulated by restraining the longitudinal displacement while allowing displacements in the radial direction as described in Chapter 3. Internal pressures of 10.6 kPa (80 mmHg) and 16 kPa (120 mmHg) were applied to the lumen surface to simulate the diastolic and systolic pressures, respectively. The diastolic pressure was used during the iterative algorithm to find the ZP configuration, as this was considered the intraluminal pressure when the images were acquired. The systolic pressure was used to find the largest stresses on the AAA. Unfortunately, the patient specific diastolic and systolic pressure were not available at the moment of the study.

5.1.3. Statistical analysis

Statistical analyses were performed in Matlab R2012 v.8.0, and data are reported by their mean and standard deviation (mean ± SD), respectively. The Lilliefors test was used to test the normality of the data. Statistical significance was tested with the Wilcoxon signed-rank test, where a two-sided p-value of less than 0.05 determined significance. Finally, linear correlations among parameters were quantified by Pearson's linear correlation coefficient ρ.

5.2. Results

The algorithm described in Chapter 4 was executed with a tolerance error of 0.2 mm (less than the image resolution). The zero-pressure geometry for the twelve patient-specific AAA geometries was computed with isotropic and anisotropic material models. Figure 34 shows the ZP and CT configuration for 4 AAA models. The figure shows how the maximum difference in geometry between the ZP and CT configurations is located in the regions with minimum ILT thickness located at the AAA bulge.

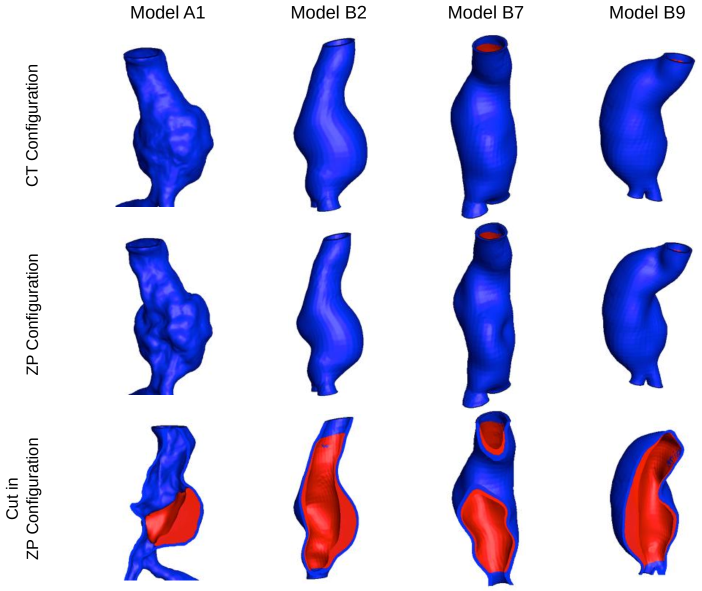

Figure 34. ZP and CT based configuration of an AAA with ILT for models A1, B2, B7 and B9 models.

Isotropic and anisotropic material models predicted almost the same zero-pressure configuration. The maximum displacement between CT-based and the computed zero-pressure geometries was about 14% and 16% for the isotropic and anisotropic model, respectively. For all models together the maximum difference between CT-based and zero-pressure geometries was 5.25 SD 1.21 mm and 5.35 SD 1.11 mm for the isotropic and anisotropic material models, respectively.

The computed PWS was 332 SD 160 kPa and 357 SD 167 kPa for the isotropic and anisotropic material models, respectively, based on the zero-pressure geometry. These values are well in the range of failure stress reported in the literature. See for example by Raghavan et al. (Raghavan & Vorp, 2000) (336 to 2351 kPa with a median of 1266 kPa for ruptured and non-ruptured aneurysms), or Di Martino et al. (DiMartino et al., 2006) (820 ± 90 kPa for electively repaired aneurysms). For model A1, the stress field obtained with the CT-based and the zero-pressure reference geometries is shown in Figure 35.

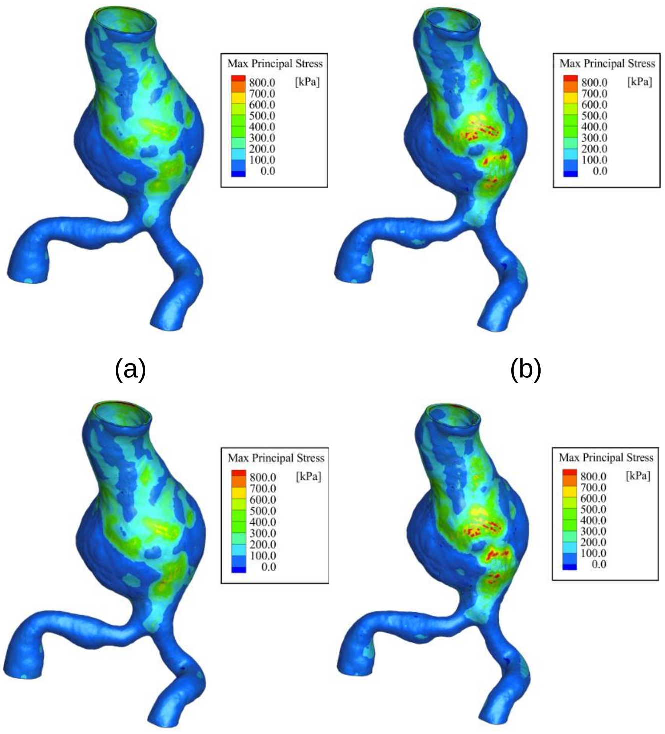

(a) (b)

(c) (d)

Figure 35. Maximum principal stress for model B1 (in kPa). (a) Isotropic model based on the CT-based geometry; (b) Anisotropic model based on the CT-based geometry; (c) Isotropic model based on the zero-pressure geometry; (d) Anisotropic model based on the zero-pressure geometry.

For the anisotropic wall model the predicted PWS was 630kPa and 810kPa for CT-based and the zero-pressure reference geometries, respectively. Hence, PWS increased approximately by 28% when considering the zero-pressure geometry. Results for the isotropic model are very similar. However, it is noted that the anisotropic model leads to slightly higher stresses. For model B1 the location of the maximum principal stress was found at the bulge within a thrombus free region of the arterial wall (see Figure 35c and Figure 35d).

In all analyzed cases, PWS using the CT-based geometry was lower than PWS obtained with the zero pressure geometry, regardless of the material model used (see Figure 36). Specifically, for isotropic and anisotropic models PWS was underestimated by 21%(SD 17%) and 14%(SD 14%), respectively.

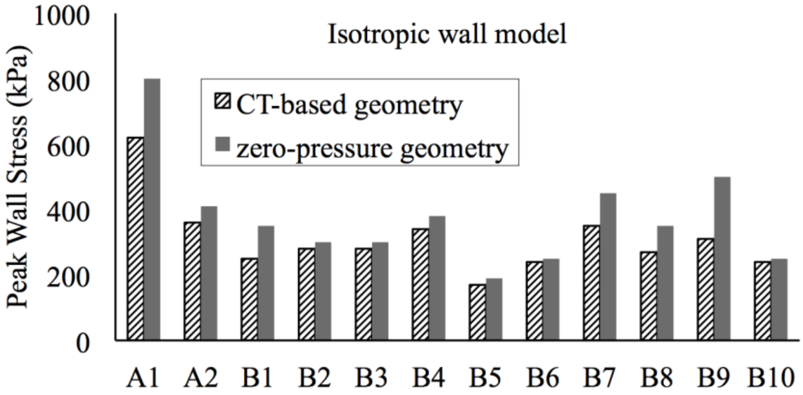

(a)

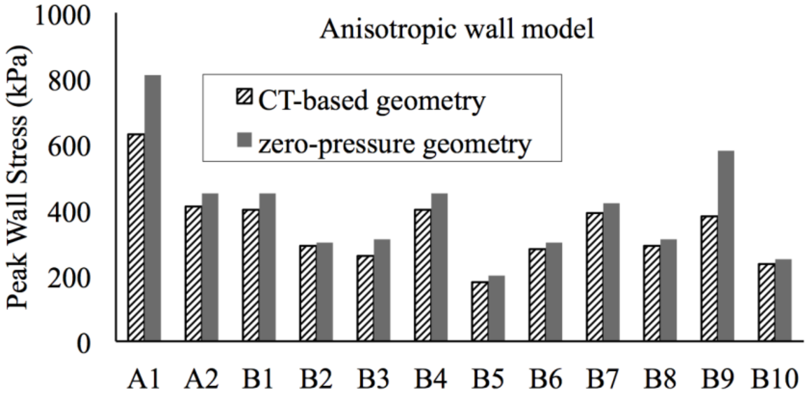

(b)

Figure 36. Predicted peak principal stresses (PWS) in the AAA wall. Results use the CT-based (striped bars) and the zero-pressure (grey bars) geometries for their stress-free reference configurations. Predictions are based on an isotropic (a) and anisotropic (b) constitutive descriptions of the AAA wall.

The difference between the predicted PWS for the CT-based and the zero-pressure geometry for both material models was tested with a paired, two-sided signed rank test. This test found significant differences (p-value 0.005) between the computations based on the zero-pressure geometry and those with the CT based geometry. In this regard, the PWS estimated with the ZP based geometry would be larger than the stress estimated based on the CT-based geometry. This finding was the same for both isotropic and anisotropic material models. In addition, the difference between the predicted PWS based on the zero-pressure geometry for the isotopic and anisotropic material models of the wall was also tested for significance. In this case, no statistical difference was found (p-value=0.093).

Figure 37 shows the PWS as a function of the maximum AAA diameter. These results used the anisotropic material model and considered the zero-pressure geometry as their reference and stress-free configuration.

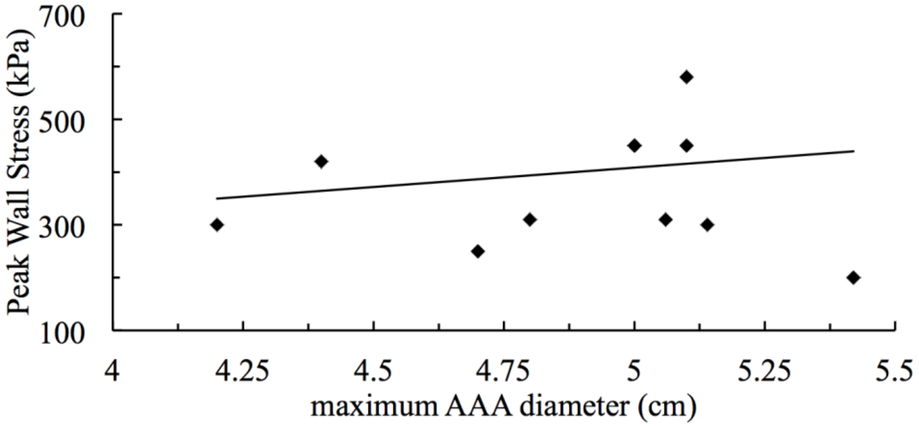

Figure 37. Peak principal stresses (PWS) in the wall compared to the diameter of AAAs Predictions considered an anisotropic constitutive model for the AAA wall and the zero-pressure geometry as their stress-free reference configuration. The trend line shows a slight increase in the PWS with the maximum AAA diameter.

Although PWS somehow increases with the diameter, no clear correlation between both variables is seen ($\rho = 0.15,$ p-value=0.64). Specifically, the highest PWS is seen in model B1 that has a diameter of 5.1 cm, whereas for B4, with the largest diameter, PWS was lowest. Figure 38 shows the cross-sections at which PWS was predicted. In order to focus the iliac arteries are hidden the image.

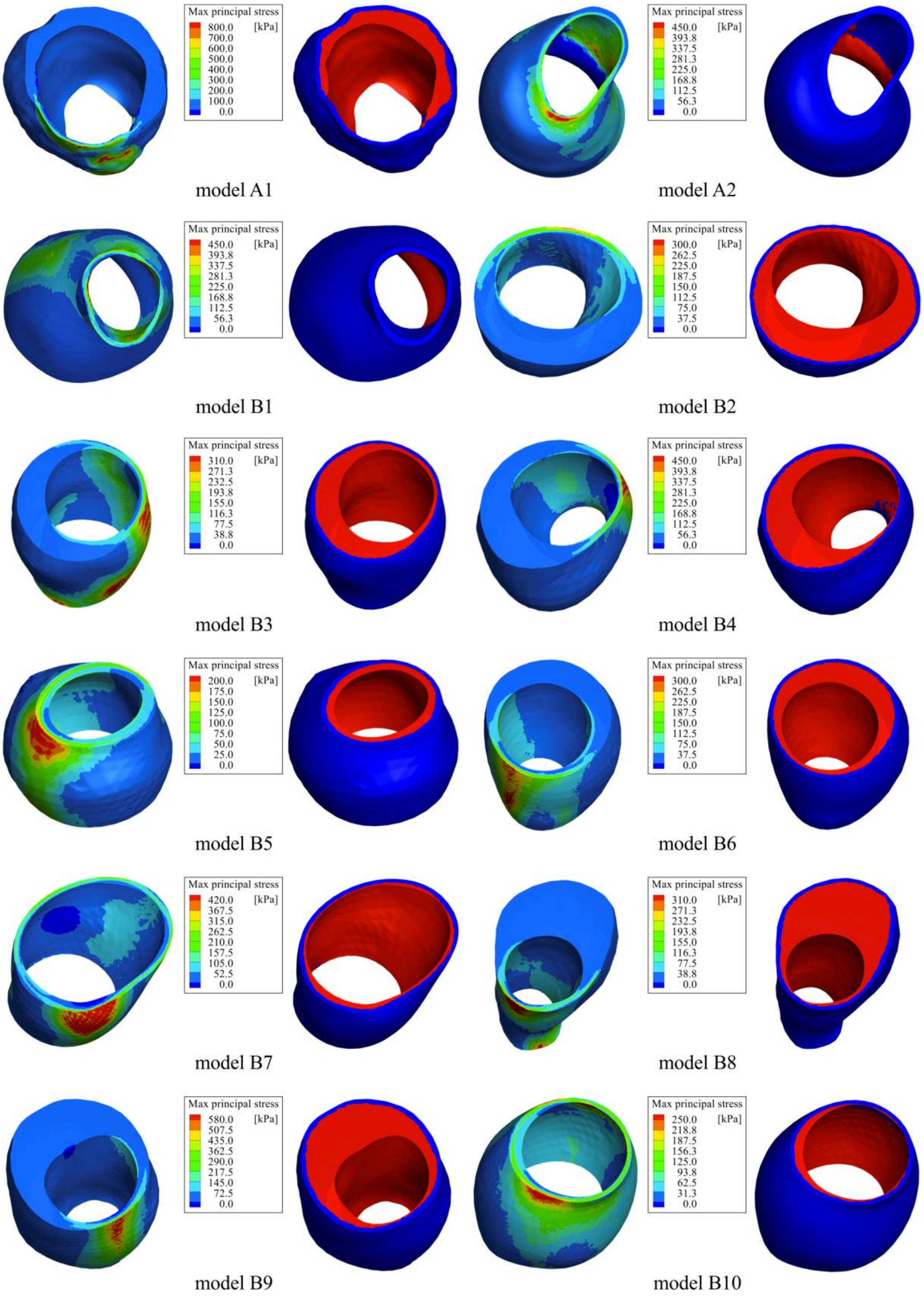
Max principal stress [kPa]
800.0
700.0
600.0
500.0
400.0
300.0
200.0
100.0
0.0
model A1
Max principal stress [kPa]
450.0
393.8
337.5
281.3
225.0
168.8
112.5
56.3
0.0
model A2
Max principal stress [kPa]
450.0
393.8
337.5
281.3
225.0
168.8
112.5
56.3
0.0
model B1
Max principal stress [kPa]
300.0
262.5
225.0
187.5
150.0
112.5
75.0
37.5
0.0
model B2
Max principal stress [kPa]
310.0
271.3
232.5
193.8
155.0
116.3
77.5
38.8
0.0
model B3
Max principal stress [kPa]
450.0
393.8
337.5
281.3
225.0
168.8
112.5
56.3
0.0
model B4
Max principal stress [kPa]
200.0
175.0
150.0
125.0
100.0
75.0
50.0
25.0
0.0
model B5
Max principal stress [kPa]
300.0
262.5
225.0
187.5
150.0
112.5
75.0
37.5
0.0
model B6
Max principal stress [kPa]
420.0
367.5
315.0
262.5
210.0
157.5
105.0
52.5
0.0
model B7
Max principal stress [kPa]
310.0
271.3
232.5
193.8
155.0
116.3
77.5
38.8
0.0
model B8
Max principal stress [kPa]
580.0
507.5
435.0
362.5
290.0
217.5
145.0
72.5
0.0
model B9
Max principal stress [kPa]
250.0
218.8
187.5
156.3
125.0
93.8
62.5
31.3
0.0
model B10

Figure 38. Cross-sections, where the peak principal stress (PWS) in the wall was predicted. Color-coded principal stresses plot (left) and segmented tissues with the ILT in red and the arterial wall in blue (right) are shown. Predictions considered an anisotropic constitutive model for the AAA wall and the zero-pressure geometry as their stress-free reference configuration.

Finally it is reported that the algorithm required between 5 to 13 iterations (average 8 iterations) to find the zero-pressure geometry with a tolerated error of less than 0.2 mm. Figure 39 shows the convergence of the algorithm for aneurysm model A2, where isotropic and anisotropic wall models were considered. Note that after 4 iterations the error norm is already below the resolution of the CT images.

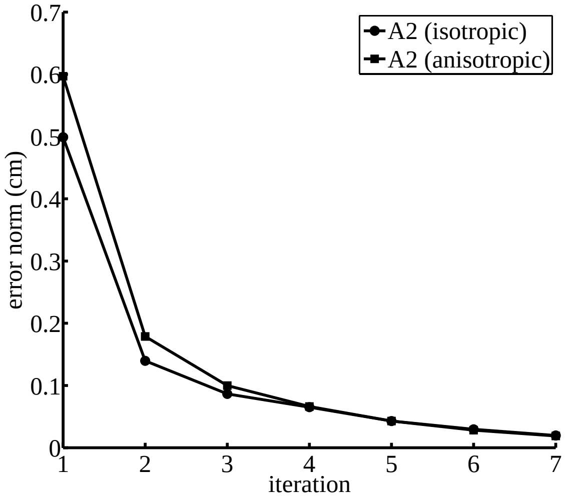

Figure 39. Convergence of the algorithm to predict the AAA zero-pressure geometry. Model A2 is considered and the computation used isotropic (circles) and anisotropic (squares) constitutive models for the AAA wall.

5.3. Discussion

The importance to determine the AAA zero-pressure configuration is indicated by a number of publications in the past few years, and that it is generally accepted that PWS estimations that use the CT-based geometries can lead to errors (Demiray, 1972; Lu et al., 2007; Raghavan et al., 2006; Speelman et al., 2009).

Previously reported approaches assumed an isotropic wall and neglected the presence of ILT. This over-simplifies the biomechanical problem and questions the reliability of stress predictions. In addition, only few of the proposed methodologies consider the three-dimensional solid AAA wall (Demiray, 1972; Speelman et al., 2009).

This chapter presents the application of a novel methodology to predict the zero-pressure geometry of patient-specific AAAs and overcomes the above mentioned limitations. In contrast to approaches that consider the CT-based geometry as the reference configuration (Demiray, 1972; Shum et al., 2011a), the proposed pull-back algorithm continuously updates the AAA reference configuration. Therefore, after convergence, the reference configuration corresponds to the zero-pressure geometry of the AAA.

This has noticeable numerical advantages over the previously reported methodologies based on incremental upgrading of the deformation gradient (Demiray, 1972; Speelman et al., 2009). Specifically, much larger increments can be used to find the zero-pressure. This is because in the present methodology, loading always starts from a zero-load reference configuration, instead of a loaded reference configuration as in the case of methodologies based on upgrading the deformation gradient (Demiray, 1972; Speelman et al., 2009).

When starting from a loaded configuration, the configuration is supposed to be in equilibrium with the applied pressure. Therefore, the inner pressure has to be incremented slowly as the deformation gradient is updated in order to avoid ill conditioning of the tangent matrix during the finite element analysis. This restriction implies a significantly larger number of iterations to converge to the zero-pressure geometry of the AAA.

The algorithm presented in this work is a modification of the method proposed by Raghavan et al. (Raghavan et al., 2006), which consists in finding a scaling factor, k, such that the zero pressure geometry can be obtained approximately as $\mathbf{X}_z \coloneqq \mathbf{X}_{image} - k\mathbf{U}$, where **U** is the normalized displacement field obtained by applying the diastolic pressure to the CT-based geometry. However, the methodology proposed by Raghavan et al. can only give approximate solutions as for any patient-specific AAA it cannot be guaranteed that the vector **U** will be the same for any pressure increment applied to the model due to material and geometric nonlinearities.

Simulations showed that in all twelve patients-specific geometries the proposed algorithm found the zero-pressure geometry in less than 13 iterations with a tolerated absolute error of 0.2 mm (or 1% relative error). Even more remarkably, setting the accuracy to the resolution of CT images (< 0.7 mm), the algorithm identified in all cases the zero-pressure geometry in less than five iterations.

Results also showed that the proposed algorithm preserved the tissue volume globally, i.e. the zero-pressure and CT-based geometries had the same volume (see Chapter 4 for details). This feature is particularly important for three-dimensional solid simulations of cardiovascular tissue, since the arterial wall and ILT are typically considered incompressible. This algorithmic feature is the direct consequence of using quasi-incompressible material descriptions (for the wall and the ILT) to predict the zero-pressure geometry. However, this kinematic restriction cannot be guaranteed at element level (Gauss points), as we observed local volume changes greater than 50%.

It is important to point out that the proposed methodology is not absent of numerical problems due to distortion of the mesh during the iterative process. In order to minimize this type of numerical problems, the use of nearly isotropic meshes with a very regular distribution of element size is recommended. Using this approach it was found a good performance in all analyzed AAA geometries.

In this work, the material behavior had little influence on identifying the ZP geometry. Specifically, the zero-pressure geometries obtained from isotropic and anisotropic material models differed by less than 3%. Similarly, PWS predictions were rather insensitive to the choice of the AAA wall model (see Figure 36). This observation is partly caused by the biaxial stress-strain data reported in van de Geest et al. (Vande Geest et al., 2006b), which reflects an almost isotropic response of the AAA wall (see Figure 9).

Consequently, the models (Equation 5) and (Equation 6) were able to fit the data quite well with the anisotropic model outperforming the isotropic one slightly (R^2=0.94 for the isotropic material versus R^2=0.95 for the anisotropic model). We used such a phenomenological approach to model the constitution of the aortic wall, although recently the collagen fiber distribution has been reported (Gasser et al., 2012). According to this data an orthotropic collagen orientation distribution should be considered in a histological model. However, at least at a macroscopic length-scale considering the detailed collagen organization might not have significant advantages over our approach.

The most remarkable changes in stress predictions were observed when changing between the CT-based and the zero-pressure geometries for the stress-free reference configuration of our simulations. Specifically, PWS obtained with the CT-based geometry was statistically significant lower than those obtained with the zero-pressure geometry. This observation holds for isotropic and anisotropic materials and was in agreement (De Putter et al., 2006; Speelman et al., 2009) as well as in disagreement (Lu et al., 2007) with previous reports. It is noted that previous conclusions has been derived without considering the ILT.

Results also point to the importance of considering ILT in biomechanical AAA simulations. The stress fields shown in Figure 38 indicate that, in addition to AAA morphology and local wall curvature (Maier et al., 2010; Shum et al., 2011b), the ILT plays an important role in the biomechanical AAA rupture risk assessment. Similar conclusions were reported from a retrospective study that compared ruptured and non-ruptured cases (Gasser, 2012).

Unfortunately there was no access to patient-specific blood pressure and it was used instead a mean diastolic and systolic arterial pressure of 80 mmHg (10.6 kPa) and 120 mmHg (16.0 kPa) respectively for all our cases. Using patient-specific pressure data would have directly influenced the predicted wall stress, but could not have changed our conclusions regarding the importance of using the zero-pressure geometry in stress predictions. Finally, it is also noted that the computations did not consider residual stresses (and strains) in the in the zero-pressure configuration. Although well documented for healthy tissue, to the authors' knowledge there was no adequate experimental data available that allows including this effect for AAA simulations.

5.4. Conclusions

A methodology was proposed to predict the zero-pressure geometry of aneurysms that is suitable for general three-dimensional solid models. Specifically, it allows for isotropic and anisotropic AAA wall models and considers the ILT. The proposed iterative method is stable and predicts the zero-pressure geometry with few iteration steps. However, since the methodology is based on finite element models, the quality of the initial mesh is vital for the performance of the algorithm.

Results indicate a statistical significant influence of the zero-pressure geometry on the PWS developed on the AAA wall as compared to predicted PWS based on the CT-based geometry. However, the results also indicate that, the choice of the material model is not as important since no statistically significant differences were found in the predicted PWS based on the zero-pressure geometry with either material model for the AAA wall.

Results obtained on twelve patient specific AAA geometries indicate that there must be other structural characteristics in the AAA geometry that have an influence on the PWS. It is noted that in most cases the PWS was located at the bared arterial wall of the bulge that was not covered by the ILT. These results suggest that the geometrical configuration of the ILT relative to the arterial wall may be an influential factor not only on the value of the peak wall stress, but also on its location within the lesion. This observation is in agreement with Wang et al. (Wang et al., 2002) which reports that the incorporation of ILT to the 3D stress analysis models of AAA has a profound influence on the magnitude and distribution of stresses acting on the AAA wall.

Finally, although only AAAs were considered in this work, the algorithm can be applied to a variety of biological structures under pressure, e.g. the heart, atria and brain aneurysms among others. The results achieved with this algorithm underscore the important effect of using the zero-pressure geometry to compute PWS values, which is also in agreement with previous studies.

ON THE IMPACT OF INTRALUMINAL THROMBUS MECHANICAL BEHAVIOR IN AAA PASSIVE MECHANICS

6. ON THE IMPACT OF INTRALUMINAL THROMBUS MECHANICAL BEHAVIOR IN AAA PASSIVE MECHANICS

Most large (approximately 75% of clinically relevant AAAs (Harter et al., 1982)) AAAs contain an Intraluminal Thrombus (ILT) (Hans et al., 2005), i.e. a non-homogenous pseudo-tissue that develops from coagulated blood and adheres to the dilated aortic wall. An ILT may partially compensate for the hemodynamic effects linked to the aneurysmatic expansion of the infrarenal aorta. Specifically, the ILT can restore the lumen of a distended aorta to a semi-normal size and helps carrying the blood pressure, i.e. it unloads the underlying wall from stress through a stress cushioning effect (Di Martino et al., 1998; Doyle et al., 2007; Hinnen et al., 2005; Li et al., 2008; Mower et al., 1997; Speelman et al., 2010; Thubrikar et al., 2003; Wang et al., 2002). The stress cushioning effect may be compromised in fissured ILTs (Li et al., 2008). However, a thick ILT layer is also known to weak the underlying AAA wall (Vorp et al., 2001), and has also been suggested to increase AAA rupture risk. Specifically, clinical studies showed that a rapid increase of ILT volume relates to AAA rupture risk (Stenbaek et al., 2000), a thicker ILT layer accelerates AAA expansion (DiMartino et al., 2006), and a large ILT leads to a higher risk for cardiovascular events (Parr et al., 2011). In conclusion, because of the above mentioned competition between stress cushioning and wall weakening effects the role of the ILT with respect to the risk of AAA rupture remains not very well understood and further studies are needed to draw sound conclusions.

As stated in Chapter 3, in-vitro testing of ILT tissue from AAAs showed found isotropic and almost linear stress strain properties (Di Martino et al., 1998; Gasser et al., 2008; O´Leary et al., 2014; Wang et al., 2001) that gradually change across the radial direction. (Gasser et al., 2010; Wang et al., 2001) Most recent data (O´Leary et al., 2014) identified two distinct ILT morphologies with different mechanical properties: i) A multilayered ILT whose strength and stiffness may either decreases gradually from the luminal to the medial/abluminal layer or decrease abruptly between the luminal and medial/abluminal layer; ii) a single layer ILT, a newly formed thrombus, with a significantly lower strength and stiffness than the multi-layered ILT.

The reported wide variability of stiffness and strength for ILT tissue suggests considering this information in a biomechanical AAA rupture risk assessment. In addition, earlier results (Rodriguez et al., 2009) indicated that peak wall stress (PWS) was predominantly located at the ILT-free aneurysm wall, suggesting that, beside the specific ILT morphology (constitution), also its topology (geometrical configuration) considerably influences PWS predictions. This conclusion is in basic agreement with many other studies (Georgakarakos et al., 2009; Inzoli et al., 1993; Li et al., 2008; Mower et al., 1997; Polzer et al., 2011; Wang et al., 2002), that observed a considerable change of wall stress magnitude and distribution when incorporating the ILT in a biomechanical analysis.

In this chapter, 21 small AAAs were reconstructed from Computer Tomography (CT) data and biomechanically analyzed in order to uncover potential mechanisms by which ILT morphology and topology influence PWS. The employed FE models considered AAA wall anisotropy, used the zero-pressure configuration as a stress-free reference configuration (Zero Pressure Algorithm from Chapter 5), and assumed hypothetical arrangements of fibrotic and newly-formed ILT of reported stiffness (DiMartino et al., 2006; Gasser et al., 2008).

6.1. Material Models

6.1.1. Patient specific models

In total, CT images of 21 non-ruptured patient-specific AAAs from two hospitals in Stockholm, Sweden, with maximum diameters between 4.2 and 5.4 cm have been considered for this study. A local ethics committee approved the use of anonymized human data, and the quality of CT images allowed accurate individual AAA models to be built. Images were reconstructed with diagnostic software A4clinics Research Edition (VASCOPS GmbH, Graz, Austria), which was applied by an operator with an engineering background and assisted by a radiologist to ensure a proper segmentation of aneurysms. Details regarding the image segmentation process are given elsewhere (Auer et al., 2010). All reconstructed models included ILT and assumed a non-homogeneous aneurysm wall thickness that varied between 1.5 mm at the thrombus-free wall and 1.13 mm at sites covered by a thick (>25mm) thrombus layer.

All surface geometries were exported in STereoLithography (STL) file format and meshed following the procedure explained in Chapter 3. The total number of elements per AAA model ranged between 486k and 1130k elements, and had at least three elements through the arterial wall thickness in order to capture the stress gradients through the wall. Table 6 show the main characteristics of the aneurysms considered in the study.

Table 6. Characteristics of AAA models for Intraluminal Thrombus mechanical behavior study.

Model	Max diameter (cm)	Total AAA volume (cm^3)	Total ILT volume (cm^3)	Lumen diameter (cm)	Arterial wall elements	ILT elements	Total elements
B1	4.20	63,18	23.80	2.40	336766	242191	578957
B2	5.06	104,03	48.20	3.05	285509	291834	577343
B3	5.00	88,37	53.60	2.65	287576	199300	486876
B4	5.42	79,78	40.20	2.30	346193	288170	634363
B5	5.14	86,23	61.80	2.60	308788	239911	548699
B6	4.8	117.05	65.92	2.30	338181	213913	552094
B7	5.10	148,21	76.10	3.00	333169	279490	612659
B8	4.70	101,45	36.80	3.60	292151	282051	574202
B9	5.14	102,88	19.30	3.50	526225	390292	916517
B10	4.69	101,61	32.50	2.30	471006	454455	925461
B11	4.96	124,14	37.30	3.00	542548	464363	1006911
B12	4.95	77,42	29.80	3.00	371334	272154	643488
B13	4.57	92,68	28.10	3.20	448897	408567	857464
B14	4.66	125,24	35.50	3.00	634232	369926	1004158
B15	4.80	86,73	39.10	2.80	370222	346075	716297
B16	4.67	100,13	19.40	3.95	561545	400480	962025
B17	5.35	137,36	55.50	2.95	582862	547318	1130180
B18	5.31	146,33	19.70	3.60	727384	321940	1049324
B19	5.11	76,21	3.90	4.15	577949	147151	725100
B20	4.88	93,58	66.60	1.75	436167	335403	771570
B21	5.26	111,50	52.20	3.30	455792	386573	842365
Mean ± Std	4.94±0.30	103.05±23.22	40.27±18.69	2.97±5.93	-	-	-

6.1.2. Material models

The aneurysmal wall tissue was modeled as an anisotropic hyperelastic material using the SEF given in Equation 6 (Rodriguez et al., 2008). The material parameters are given in Table 2. For ILT we have considered two extreme cases: i) A stiff thrombus tissue named as Type A ILT; and ii) A more compliant thrombus named as Type B ILT. In addition, ILT tissue is regarded isotropic, i.e. constitutive formulations are independent of the principal anisotropy direction $\mathbf{a_0}$**.** For Type A, the SEF proposed by Di Martino and Vorp given by Equation 7 has been used. ON the contrary, for type B ILT, representing a more compliant ILT tissue, we have used SEF proposed in the study by Gasser et al given by Equation 8. Material parameters for both SEFs are found in Chapter 2.

6.1.3. Finite element simulations

FE simulation was carried out in ABAQUS (Dassault Systèmes Simulia Corp.). The anisotropic material model for the AAA wall was implemented as a user subroutine UANISOHYPER_INV, whereas the ILT material models used the software's standard material libraries. The principal anisotropy direction a_0 was defined as described in Chapter 2.

Unfortunately, there was no access to patient-specific intraluminal blood pressure and instead mean diastolic and systolic arterial pressures of 80 mmHg (10.6 kPa) and 120 mmHg (16.0 kPa) was used, respectively, for all the cases. The diastolic pressure was used during the iterative algorithm to find the zero-pressure configuration, as the recorded images characterize this state of loading. The systolic pressure was used to find the largest stresses in the AAA wall. The constraints due to the thoracic aorta and common iliac arteries were simulated by restraining the longitudinal displacement while allowing displacements in the radial direction.

It is noted that the aneurysmal model considers uniform mechanical properties, and we made no distinction between the aneurysm and the adjacent vasculature. In addition, residual stresses in the zero-pressure configuration have been neglected and no contact with surrounding organs was considered. A refined model should consider the variation in the mechanical properties between the arterial and aneurysmal tissues as well as AAA wall heterogeneities (Tierney et al., 2012). However, as in the case of ILT tissue, this information was not available from the CT images.

The developed FE models were equipped with different ILT models that aim at capturing ILT variability with respect to morphology and topology. In addition FE models that completely neglect the ILT were used for reference wall stress predictions.

Stress for the arterial wall are reported as peak maximum principal wall stress (PWS) and as average stress (MPWS) calculated as:

$$MPWS = \frac{1}{V}\int_V \ \sigma_{III} dV, \qquad \text{(Eq. 9)}$$

where V is the AAA tissue volume and σ_{III} is the maximum principal stress. For the ILT, peak and average stresses refer to the von Mises stress.

6.1.4. Statistical analysis

Statistical analyses were performed in Matlab R2012 v.8.0, and data are reported by their mean and standard deviation (mean ± SD), respectively. The Lilliefors test was used to test the normality of the data. Statistical significance was tested with the Wilcoxon signed-rank test, where a two-sided p-value of less than 0.05 determined significance. Finally, linear correlations among parameters were quantified by Pearson's linear correlation coefficient ρ.

6.2. Results

FE models equipped with homogeneous ILT properties predicted PWS of 405 kPa (SD 168 kPa) and 484 kPa (SD 143 kPa) for type A and type B ILT material models, respectively. Both stress values are significantly lower than the failure stress reported in the literature for electively repaired aneurysms (DiMartino et al., 2006), i.e., 820 kPa (SD 90 kPa). In all analyzed cases the PWS was found to be higher for the model using the softer (type B) ILT material model, see Figure 40a (detail results for each AAA are given in APPENDIX A).

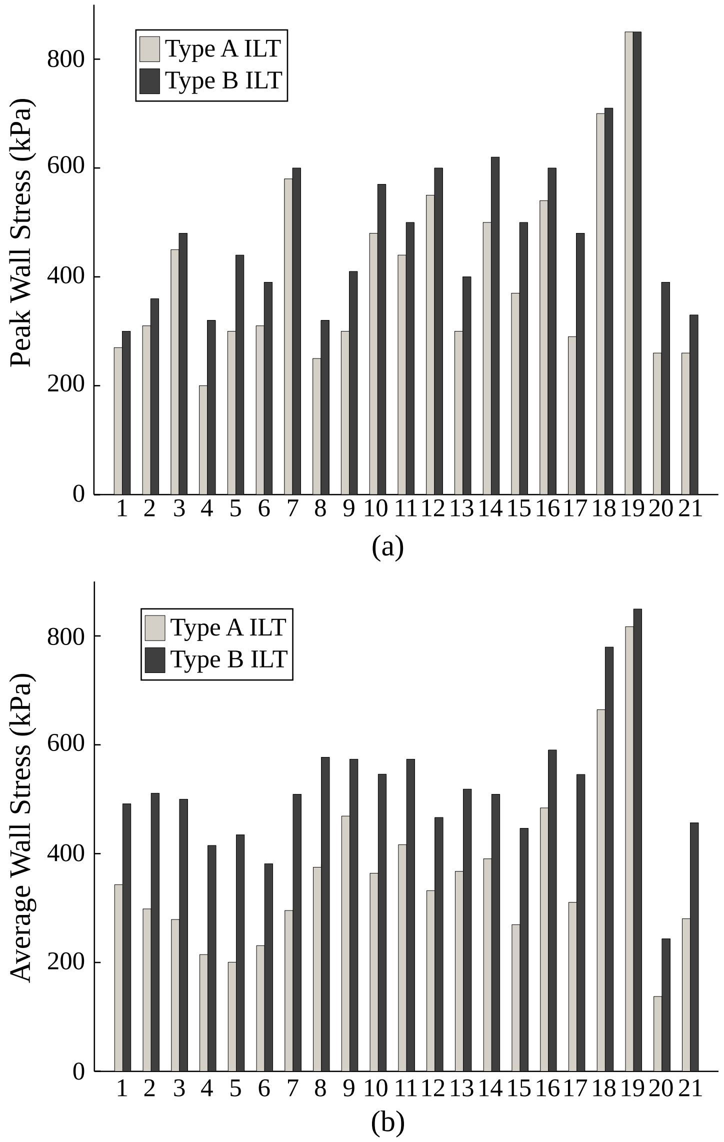

(a)

(b)

Figure 40. a) Predicted peak principal stresses in the AAA wall; b) Predicted average principal wall stress in the wall. Results use the zero pressure geometries for their stress-free reference configurations. Predictions are for the type A ILT (light grey bars) and for the type B ILT (dark grey bars).

The influence of the ILT material behavior on the AAA stress field becomes clearer when considering the MPWS. In this case, the two groups (type A and type B) are clearly distinguishable, see Figure 40b. Both PWS ($p<0.001$) and MPWS ($p<0.001$) were different for simulations using type A and type B ILT models.

Differently to what was found for the wall stress, the average stress in the ILT was higher for type A than for type B thrombus (p<0.001), see Figure 41. This result is consistent with the larger compliance of the type B ILT. For both ILT model types, the predicted average stress was lower than the experimentally identified rupture stress of ILT (Gasser et al., 2008) (type A: 156 kPa (SD 57.9); type B: 47.7 kPa (SD 22.9)).

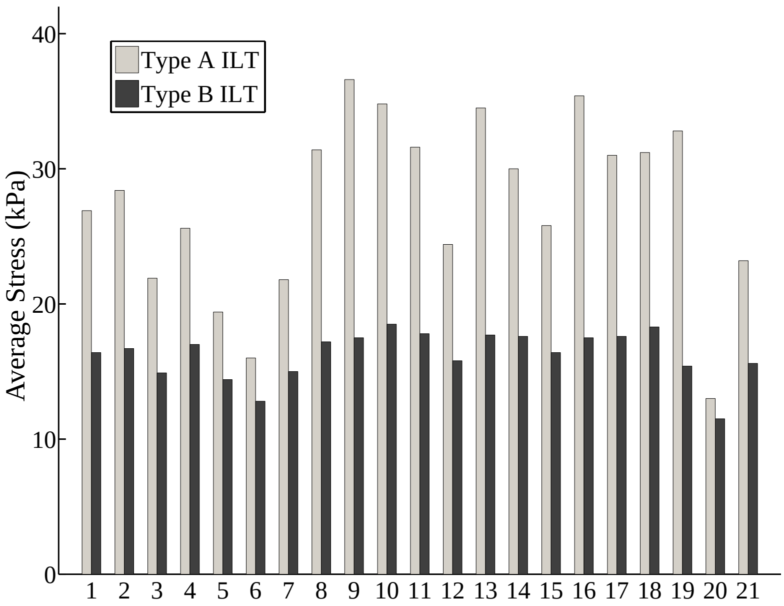

Figure 41. Predicted average von Mises stress in the ILT. Results use the zero pressure geometries for their stress-free reference configurations. Predictions are for the type A ILT (light grey bars) and for the type B ILT (dark grey bars).

Correlations of PWS and MPWS with AAA diameter and ILT volume are shown in Figure 42. Despite PWS somehow increases with the diameter, no significant correlation between both variables is seen for any type of ILT (Type A: ρ=0.09, p=0.69; Type B: ρ=0.15, p=0.51). On the contrary, borderline significance was seen for the correlation with the ILT volume (type A: ρ=-0.44, p=0.05; type B: ρ=-0.40, p=0.07). Similar to PWS, no correlation of MPWS was seen when tested against the diameter (Type A: ρ=0.05, p=0.82; Type B: ρ=0.15, p=0.52). However, a strong correlation between MPWS and ILT volume was found (Type A: ρ=-0.77, p<0.001; Type B: ρ=-0.69, p=0.001) indicating the significant influence of the ILT on wall stress in AAAs.

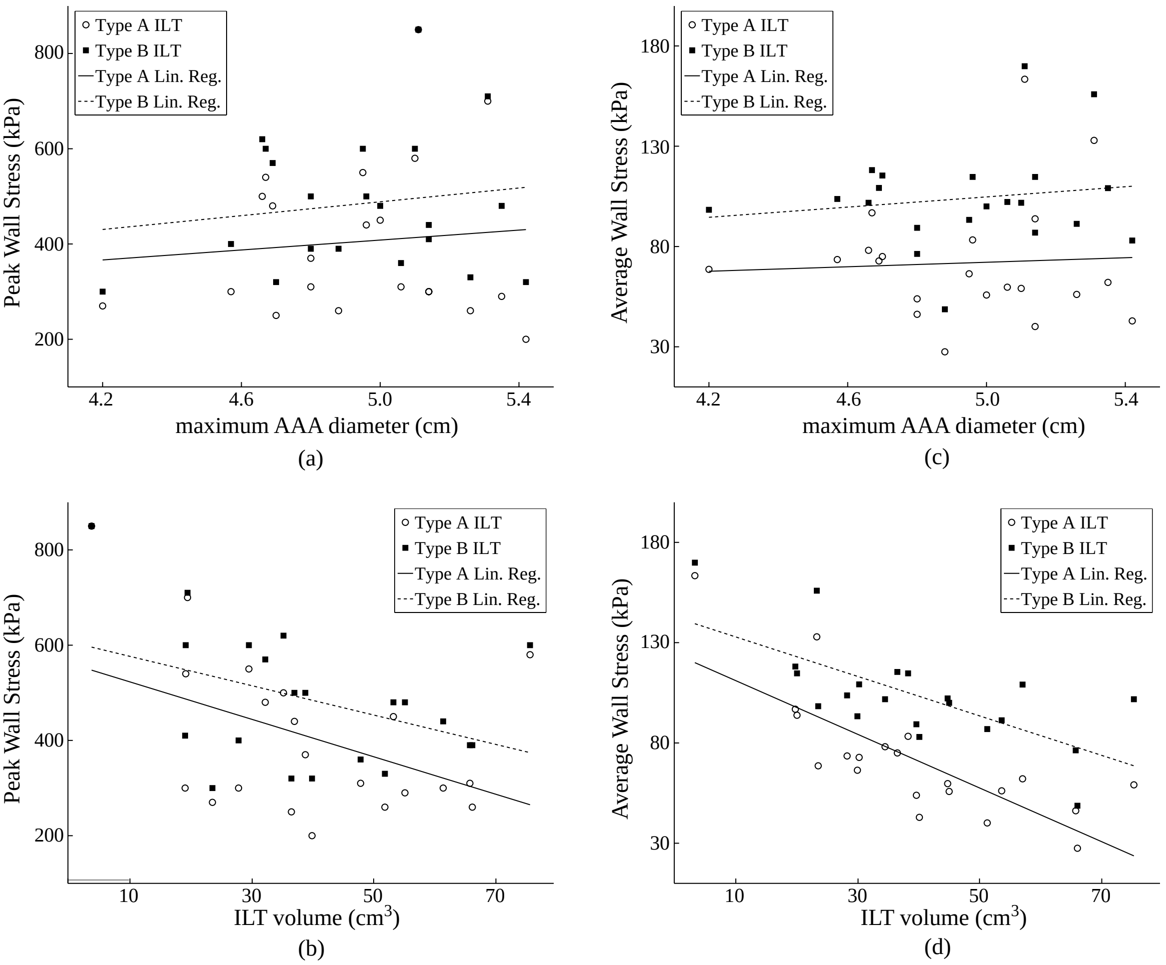

Figure 42. Predicted maximum principal wall stress (panels a and b) and average maximum principal wall stress (panels c and d) in the AAA wall for both types of ILT material compare to the maximum AAA diameter (panels a and c), and the ILT volume (panels b and d). Results use the zero pressure geometries for their stress-free reference configurations. The trend line shows a slight increase of the PWS with AAA maximum diameter, where as PWS shows a tendency to decrease with ILT volume. The observed tendency is the same for both ILT types.

In order to further investigate the influence of the ILT on the wall stress predictions, stress results with the different ILT models were compared to predictions from FE models that completely neglected the ILT. Specifically, the stress ratio between the maximum principal stress (vonMises stress for the ILT) from simulations without ILT and with a particular ILT model (type A or type B) was computed for each element of the AAA model, see Figure 43 (Detail Results for all AAA models are shown in APPENDIX B).

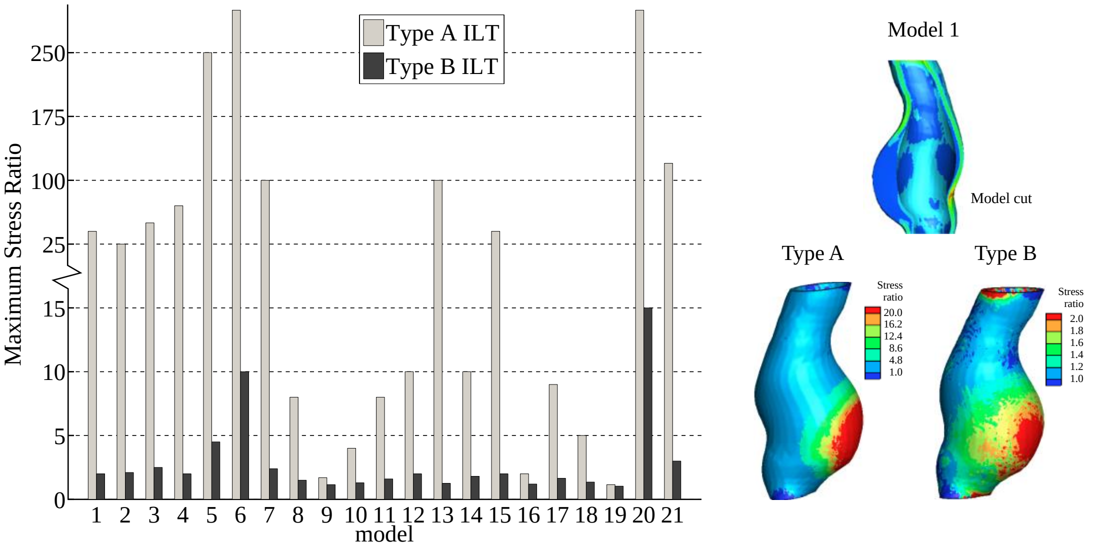

Figure 43. Predicted maximum stress ratio in the AAA wall covered by the ILT due to the presence of the ILT. Predictions are for the type A ILT (light grey bars) and for the type B ILT (dark grey bars). The inset shows the stress ratio profile for model 1. The maximum stress ratio located in the area of maximum ILT thickness.

Figure 43 nicely illustrates that a stiffer ILT model (type A) leads to a significantly higher stress reduction than the more compliant ILT model (type B) for all AAA cases. It is also noted that for AAA with thin ILTs, e.g. models 9, 16, and 19, a similar maximum stress ratio for both ILT types is obtained. In particular, case 19 has almost no ILT. Therefore, stress predictions from all models (type A, type B and no ILT) are similar. In addition to the results shown in Figure 43, it is noted that stress reduction is clearly limited to the sites that are covered by ILT while ILT-free parts of the wall remain exposed to the same stress that was predicted by the ILT-free FE models. This observation is illustrated for case 1 by the inset of Figure 43 and hold also for all other cases.

A closer analysis of the stress field obtained for each of the models (see Figure 44) suggests that the topology of the ILT may play a more important role on the PWS than ILT. Figure 44 shows the maximum principal stress using type A ILT for 20 models (model 19 has been excluded because it is almost free of ILT). This figure indicates that the PWS, in the lesion, seems to be located in the area corresponding to ILT-free parts of the wall. In fact, a detailed analysis of different sagittal sections of the models revealed that the PWS was located on areas with minimum ILT thickness.

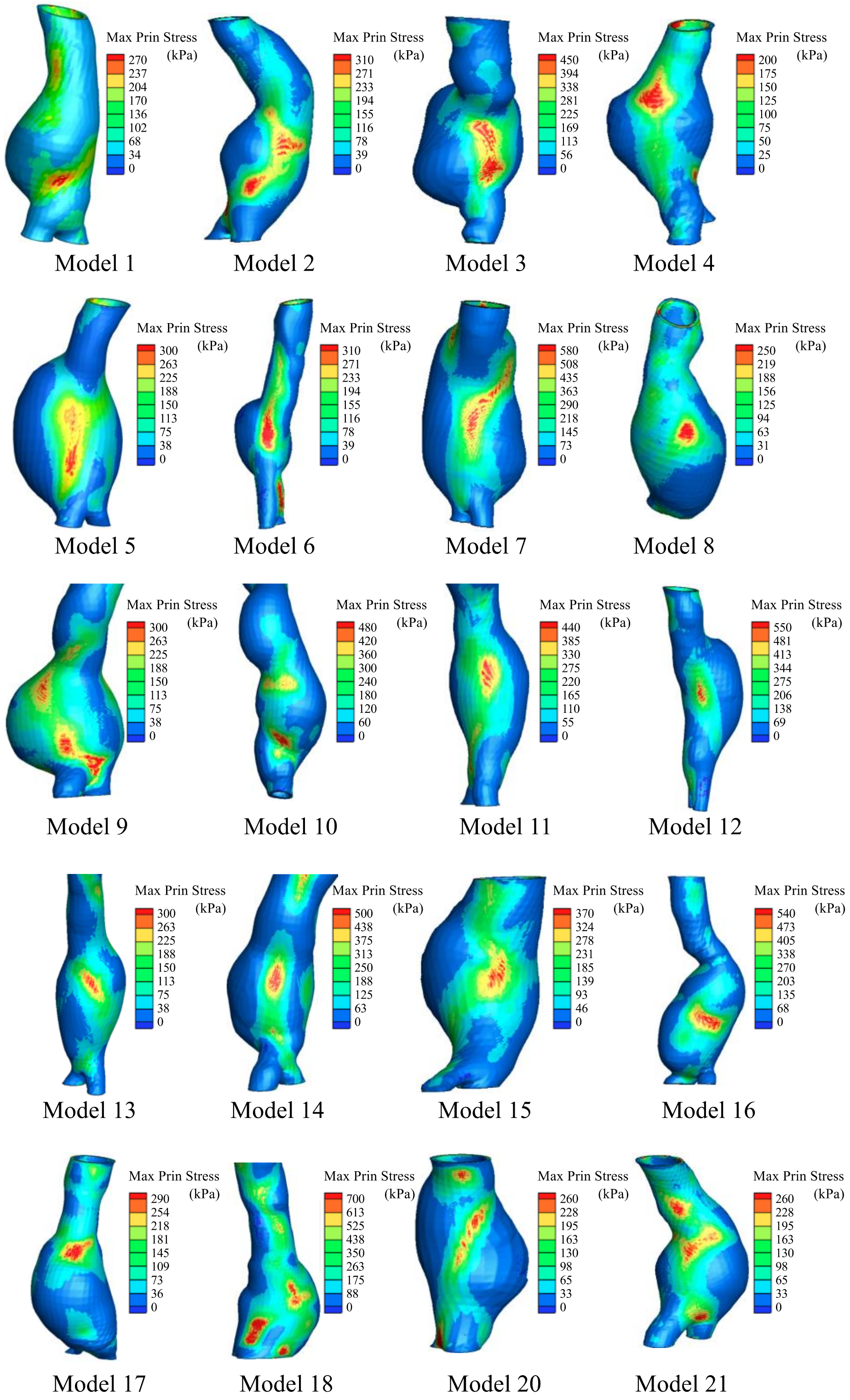
Max Prin Stress (kPa)
270 237 204 170 136 102 68 34 0
Model 1
Max Prin Stress (kPa)
310 271 233 194 155 116 78 39 0
Model 2
Max Prin Stress (kPa)
450 394 338 281 225 169 113 56 0
Model 3
Max Prin Stress (kPa)
200 175 150 125 100 75 50 25 0
Model 4
Max Prin Stress (kPa)
300 263 225 188 150 113 75 38 0
Model 5
Max Prin Stress (kPa)
310 271 233 194 155 116 78 39 0
Model 6
Max Prin Stress (kPa)
580 508 435 363 290 218 145 73 0
Model 7
Max Prin Stress (kPa)
250 219 188 156 125 94 63 31 0
Model 8
Max Prin Stress (kPa)
300 263 225 188 150 113 75 38 0
Model 9
Max Prin Stress (kPa)
480 420 360 300 240 180 120 60 0
Model 10
Max Prin Stress (kPa)
440 385 330 275 220 165 110 55 0
Model 11
Max Prin Stress (kPa)
550 481 413 344 275 206 138 69 0
Model 12
Max Prin Stress (kPa)
300 263 225 188 150 113 75 38 0
Model 13
Max Prin Stress (kPa)
500 438 375 313 250 188 125 63 0
Model 14
Max Prin Stress (kPa)
370 324 278 231 185 139 93 46 0
Model 15
Max Prin Stress (kPa)
540 473 405 338 270 203 135 68 0
Model 16
Max Prin Stress (kPa)
290 254 218 181 145 109 73 36 0
Model 17
Max Prin Stress (kPa)
700 613 525 438 350 263 175 88 0
Model 18
Max Prin Stress (kPa)
260 228 195 163 130 98 65 33 0
Model 20
Max Prin Stress (kPa)
260 228 195 163 130 98 65 33 0
Model 21

Figure 44. Stress field in the AAA models with asymmetric ILT. The PWS was always located in the side where ILT thickness is minimum. Results correspond to type A ILT.

This observation hold also when using type B ILT, and explains the good correlation between PWS and minimum ILT thickness shown in Figure 45a (Type A: ρ=-0.73, p<0.001; Type B: ρ=-0.62, p=0.002). In addition, for the section where the PWS is located we have found a strong correlation between

PWS and the Laplace's law computed using the effective lumen diameter and the effective wall thickness, $\mathrm{D_{lumen}}/(\mathrm{t_{wall}}+\mathrm{t_{ILT}^{min}})$ (type A: ρ=0.87, p<0.001; type B: ρ=0.81, p<0.001) as shown in Figure 45b. Here, $\mathrm{D_{lumen}}$ denotes the lumen diameter at the section of minimum ILT thickness, $\mathrm{t_{ILT}^{min}}$, and $\mathrm{t_{wall}}$, is the local effective wall thickness at this site.

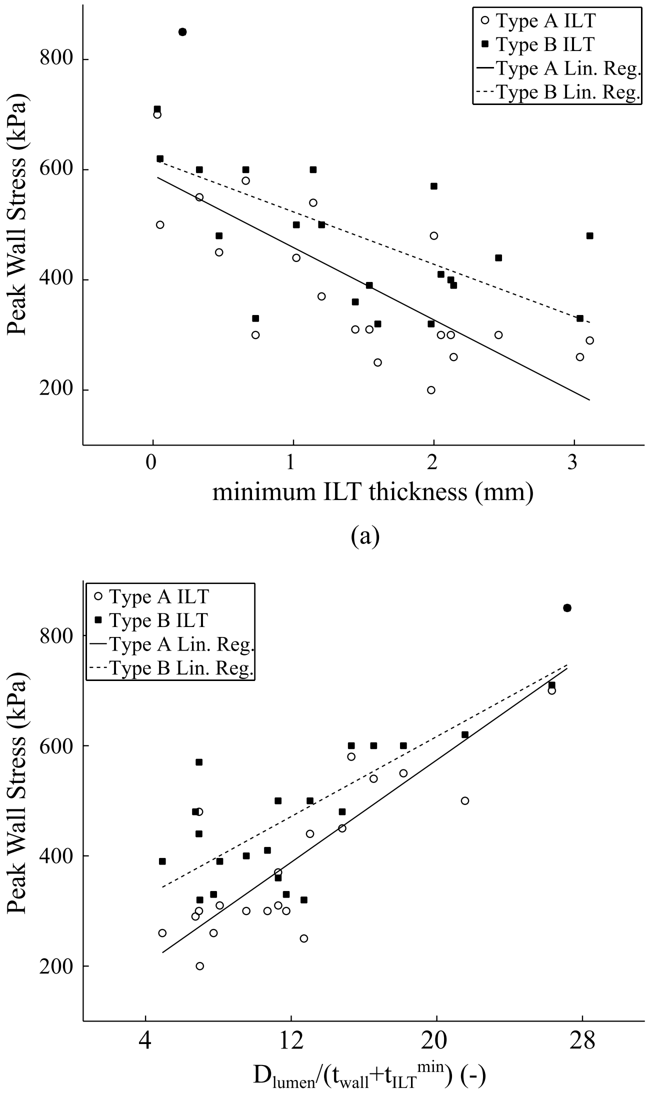

(a)

(b)

Figure 45. Peak Wall Stress for both ILT types. a) As a function of minimum ILT thickness; b) As a function of the local lumen diameter to wall thickness plus minimum ILT thickness ratio.

Current state of the art assumes homogeneous ILT properties in the simulations since its heterogeneity is not available from CT scans. However, as demonstrated in previous studies (Gasser et al., 2008; O´Leary et al., 2014), the ILT is heterogeneous with a stiff and high resistant lumen layer and a weaker and compliant medial-abluminal layer. Due to missing information regarding the spatial composition of ILT our remaining analysis was based on a hypothetical model that allocates only stiff AAA tissue (modeled as Type A ILT material) and more compliant AAA tissue (modeled as Type B ILT material) as shown in Figure 46 where results for AAA model B20 are shown.

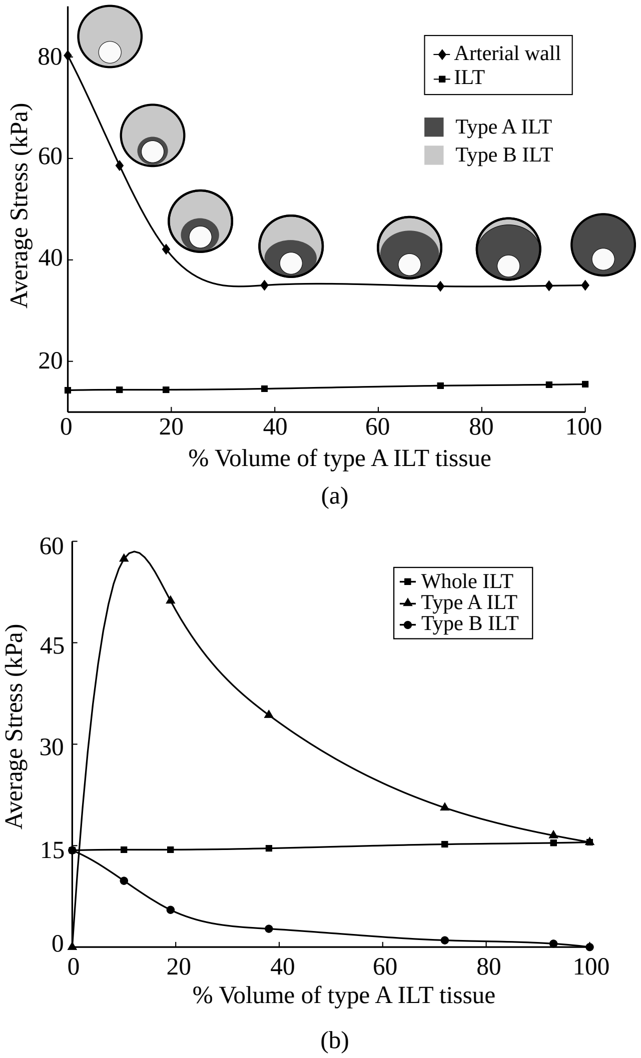

Figure 46. Average stress for a hypothetical heterogeneous ILT. Heterogeneity is represented as volume percentage of Type A ILT tissue (section in dark grey in the top panel). a) Mean stress in the arterial wall (solid line with solid diamonds) and ILT (solid line with solid squares); b) Mean stress in the ILT (solid line with solid squares) and in the individual ILT components: Type B ILT (solid line with solid circles) and Type A ILT (solid line with solid triangles).

Figure 46 shows the average AAA wall stress (MPWS) and the average ILT stresses as a function of the volume percentage of type A ILT. The top panel indicates a reduction of the average wall stress until reaching a steady value as the percentage of type A ILT increases. On the contrary, the average ILT stress increases monotonically, but slowly, with the percentage of type A

ILT. It is noted that ILT stress behavior is more complex distributed within the different layers (luminal and medial/abluminal layers), see Figure 46b. While average stress in the type A ILT layer (in the luminal side) shows a non-monotonic behavior, the average stress in the type B ILT layer (medial/abluminal layer) decreases monotonically with the percentage of type A ILT. This indicates that the stiffer layer of the ILT bears most of the ILT load.

Similar results were found on other six models analyzed. Figure 47 shows the MPWS on the seven models (Results and Figures for all 7 models are shown in Appendix C). The figure corroborates the reduction on the MPWS as the percentage of stiff ILT increases.

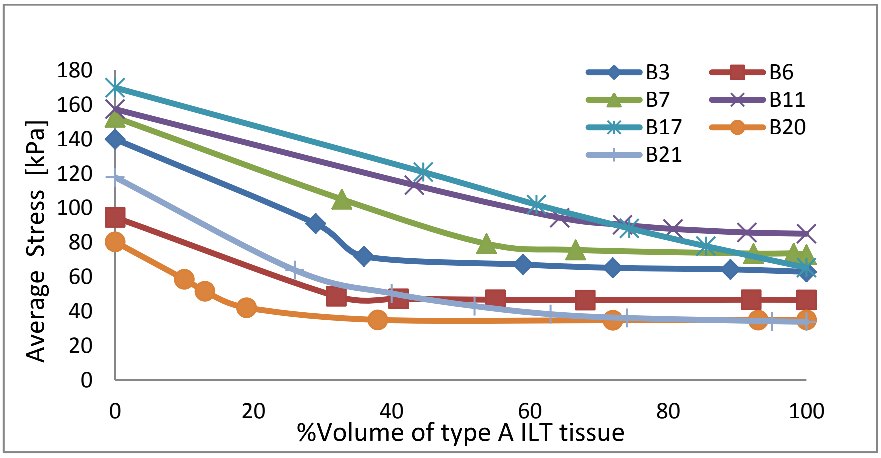

Figure 47. Average stress of Aneurismal Wall for hypothetical heterogeneous ILT for 7 different AAA models.

The monotonically increase in the mean stress of the whole ILT as the percentage of type A ILT increases is also found in all 7 models (see Figure 48). However, the rate at which the MPWS increases is quite sensitive to the size on topology of the ILT. For instance, the increase in the ILT’s MPWS was found to be very slow for models with the thickest ILT (B6 and B20), whereas MPWS increased at the fastest rate on models B11 and B17 with the thinnest ILT.

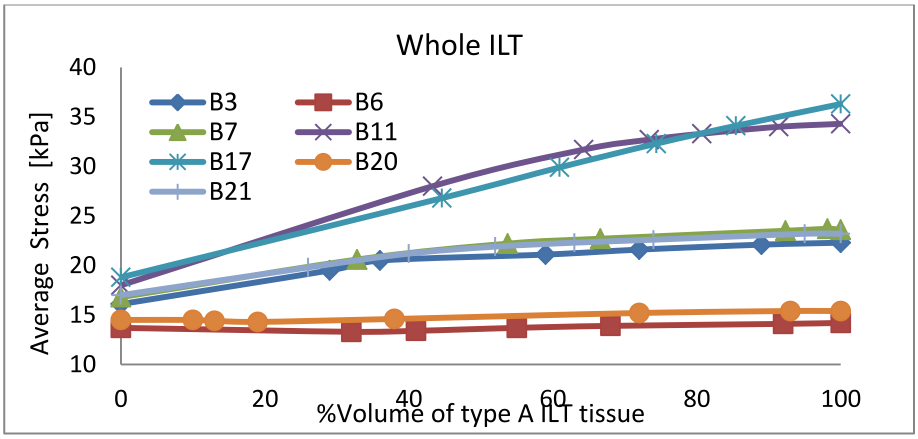

Figure 48. Average stress of the ILT for hypothetical heterogeneous ILT for 7 different AAA models.

In all 7 models it was found that the stiffer layer of the ILT bears most of the ILT load, see Figure 49, although. Again, the variation of the MPWS with the percentage of type A ILT was found to be very dependent on the ILT volume and ILT topology.

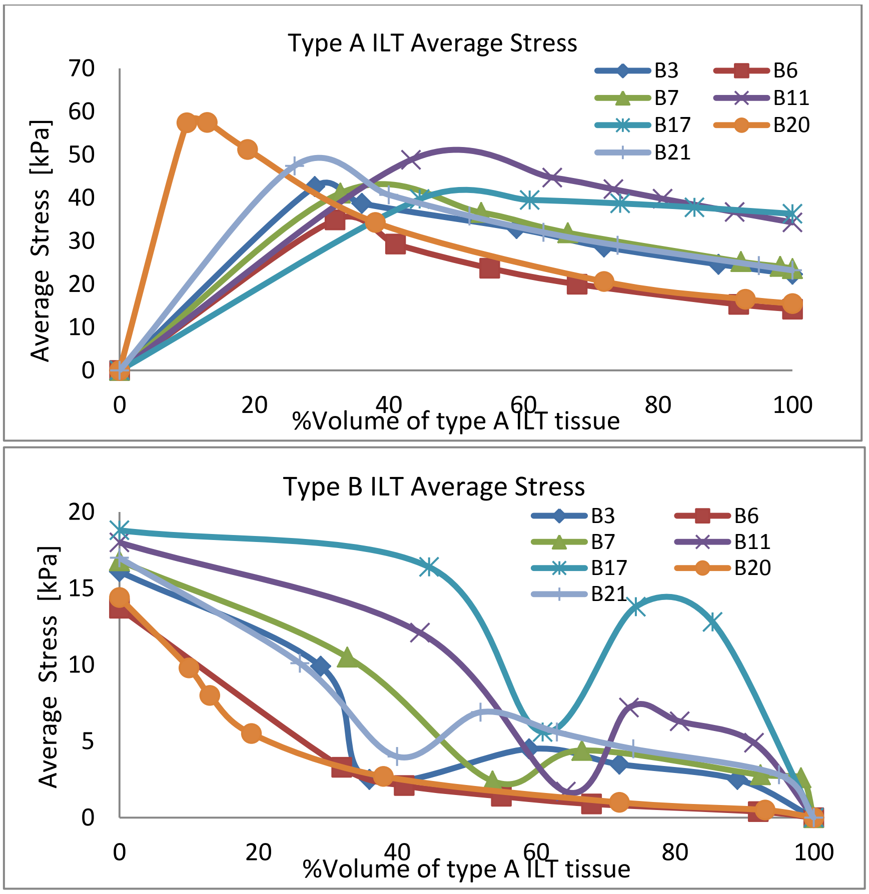

Figure 49. Average stress of Type A and Type B for hypothetical heterogeneous ILT for 7 different AAA models.

It is, however, interesting to note that it was always found a critical percentage of type A ILT for which the MPWS of the Type A ILT reached a maximum, whereas the more compliant type of ILT, type B ILT, reduces the value (even though this reduction may not be always monotonic as in the case of the arterial wall).

6.3. Discussion

The importance of the ILT on AAA mechanics has attracted the attention of researchers for a long time. Most studies have focused on characterizing the mechanical properties of the ILT under static and dynamic (fatigue) conditions (DiMartino et al., 2006; Gasser et al., 2008; Kazi et al., 2003; O´Leary et al., 2014; Vande Geest et al., 2006a), the association of ILT with hypoxia and aneurismal growth (Speelman et al., 2010; Stenbaek et al., 2000; Vorp et al., 2001).

In addition some studies investigated the effect of ILT on the wall stress (Di Martino & Vorp, 2003.; Gasser et al., 2010; Georgakarakos et al., 2009; Polzer et al., 2012; Polzer et al., 2011; Wang et al., 2001). In this regard, Di Martino and Vorp (Di Martino & Vorp, 2003.) studied the variation of ILT material properties on idealized geometries, but no conclusive studies are available on patient-specific geometries.

The present study used 21 patient-specific AAA cases to investigate the impact of ILT mechanical properties and topology on the PWS of patient specific AAA geometries under static conditions. Specifically state-of-the-art modeling assumptions were used, such as finite strains, anisotropy of the AAA wall and the zero-pressure configuration for all computations. ILT constitutions was represented through two extreme conditions: a firm and compact ILT tissue (type A), and a softer and more compliant ILT tissue (type B) (O´Leary et al., 2014). Finally, the influence of ILT heterogeneity on stress distributions was studied using idealized compositions of compact and soft ILT tissues.

The present study found a statistically significant influence of ILT's mechanical properties on the PWS and the MPWS, and therefore potentially also on AAA rupture risk. This is partially supported by the fact that variations in the PWS and MPWS are much stronger correlated with ILT volume than with the maximum AAA diameter. A finding that is in agreement with previous studies (Georgakarakos et al., 2009; Li et al., 2008; Speelman et al., 2010).

Consequently, for AAAs of similar diameter, ILT topology and composition seems to modulate the stress field in the AAA arterial wall. Clearly also other geometrical factors like AAA size (Elger et al., 1996; Georgakarakos et al., 2010a; Inzoli et al., 1993; Maier et al., 2010; Raut et al., 2013a; Rodriguez et al., 2008; Shum et al., 2011a), asymmetry (Elger et al., 1996; Hans et al., 2005; Rodriguez et al., 2008; Alastrué et al., 2006.; Shum et al., 2011a), wall curvature (Elger et al., 1996; Georgakarakos et al., 2010a; Inzoli et al., 1993; Raut et al., 2013a; Shum et al., 2011a), etc. influence wall stress , and to what extent ILT topology is linked to them could not be investigated in the present study.

In all cases with ILT (n=20), the location of the PWS coincided with the section of minimum ILT thickness, and PWS correlated with the minimum ILT thickness ($\rho<-0.73$ $p<0.001$). This suggests that ILT topology dictates the location of the PWS. Moreover, a remarkable correlation ($\rho >0.87$; $p<0.001$) was found between PWS and the ratio between the effective lumen diameter and the stress-carrying structure thickness, i.e. the minimum ILT thickness plus the local arterial wall thickness. This demonstrates that the PWS in these cases is mainly determined by membrane type of loading, i.e., following Laplace’s law. This result suggests that, in addition to maximum AAA diameter, particular attention should be paid to effective lumen diameter and minimum effective AAA thickness (wall + ILT thickness) when evaluating AAA risk.

Regarding the mechanical properties of the ILT, our results show that, for the same ILT geometry, a more compliant ILT leads to higher wall stress than a less compliant ILT. Consequently, a stiffer ILT is associated with a more pronounced reduction in the wall stress than a more compliant, ILT.

Note also that the aneurysm wall is remarkably weaker and thinner (Kazi et al., 2003; Vorp et al., 2001) behind (thick) ILT when compared to the ILT-free wall. While the formation of new thrombus is a fast process, remodeling of the wall is determined by collagen turn-over, i.e. at a half-life time of about two month (Nissen et al., 1978). Consequently, since the AAA wall might be stronger behind a newly formed (soft) ITL than behind an older fibrotic (stiff) ILT, the less pronounced stress reduction effect due to the soft thrombus should not directly be seen as an increased risk of AAA rupture. Moreover, our results indicate that the stress reduction in the wall when an ILT is present obeys to an overall increase in the AAA stiffness due to the presence of the ILT, which can be several times thicker than the wall, rather than a direct impact of the ILT's mechanical stiffness.

ILT heterogeneity markedly affected the stress field in the wall and ILT in our idealized study. While the mean stress in wall and the ILT varied monotonically as the percentage of the stiffer layer increases, a remarkable different behavior was found for the individual layers in the ILT. Most interestingly, the stiffer layer in a heterogeneous ILT was found to carry most of the load within the ILT. In fact, the simulations indicate that the mean stress in the stiffer layer may be larger than the mean stress in the wall. Since the strength of the luminal layer is considerably lower than the arterial wall (DiMartino et al., 2006; Gasser et al., 2008), these results suggest that failing of the luminal layer could occur in a heterogeneous ILT before the wall fails. Previous studies have suggested failure of the ILT tissue as a cause of AAA rupture (Georgakarakos et al., 2010b; Polzer et al., 2011).

Several limitations are associated with this study. By the moment of the study, we did not have access to patient-specific blood pressures and used mean population values instead. However, conclusions drawn regarding the influence of ILT mechanical properties and morphology on AAA biomechanics should be almost independent from this limitation. Not considering the poroelastic nature of the ILT is another study limitation (Ayyalasomayajula et al., 2010; Hinnen et al., 2005; Polzer et al., 2012).

A recent study reports that including the poroelastic description of a homogeneous ILT does not change the computed arterial wall stress that was predicted with hyperelastic descriptions (Polzer et al., 2012). However, this conclusion might not be directly applicable to inhomogeneous ILT composition.

Also with respect to the inhomogeneous ILT results, our study could only use idealized compositions of ILT. Despite the developed analysis framework could easily process patient-individual ILT compositions, this information was not available for the present study. In addition, since vascular tissue properties are spatial inhomogeneous, a refined model should at least incorporate the gradual variation of properties between normal arterial and diseased (aneurysmal) tissues.

Finally, it is also noted that our computations did not consider residual stresses (and strains) in the zero-pressure configuration. Although well documented for healthy tissue, to the authors' best knowledge no adequate experimental residual stress data for AAA has been reported.

In summary, the present work aimed at exploring the role played by the ILT on the stress distribution in AAAs using state-of-the-art modeling assumptions. The identified strong correlations of PWS with both, ILT volume and the minimum thickness of the ILT layer, underlined the importance played by ILT in the AAA wall stress distribution. Likewise, for all analyzed cases where the ILT was present, the location of the PWS coincided with the section of minimum ILT thickness, which demonstrated the significance played by ILT topology, i.e. geometrical configuration with respect to the arterial wall.

Finally, ILT heterogeneity, i.e. the spatial composition of soft and stiff thrombus tissue can also considerably influence the stress in the AAA helping to reveal possible failing mechanisms associated with the ILT tissue that may increase the risk of aneurysm rupture. Therefore, we recommended considering this information for a biomechanical analysis of AAA. The present study is limited to the identification of influential biomechanical factors, and how its findings translate to an AAA rupture risk assessment remains to be explored by clinical studies.

CONCLUSIONS

7. CONCLUSION

The main aim of this thesis was to deepen in the knowledge of the passive biomechanics of Abdominal Aortic Aneurysms; seeking on results that could help modify the current medical criteria for surgery, which is based mostly on the diameter and ILT growth, but leaving aside other geometric or tissue characteristics that had been shown to affect the biomechanical integrity of the aneurysmal wall either for good or worse.

The first achieved objective was the development of an algorithm, which allows a better estimation of the stress field on an AAA. The named “Zero Pressure Algorithm” allows to determine the unloaded geometry of an AAA so that using this geometry, the systolic pressure can be applied and more realistic stress field is found compared to what it has been done up to the date, that was to use a pressurized CT based geometry (pressurized by the diastolic pressure) and to apply the systolic pressure to this one.

The proposed algorithm was checked on three in-silico experiments, and rigorously tested using experiments. The performance of the algorithm to identify the Zero Pressure configuration was clearly demonstrated by both methodologies. In addition, the algorithm has been applied on almost 30 AAA models throughout this work, in all of them including the ILT, which has been usually neglected in other studies. The main advantages of the algorithm are that: it preserves the tissue volume globally thus guaranteeing the incompressibility; ZP geometry can be obtain in a reasonably number of iterations (less than 6 iteration in average) with an accuracy equal to the resolution of CT images. Although this algorithm was developed for AAA, it can be applied to a variety of biological structures under pressure, e.g. the heart, atria and brain aneurysms among others.

The main findings when applying the Zero Pressure Algorithm to 12 models of AAA was that the PWS was underestimated by 21% (SD 17%) and 14% (SD 14%) for isotropic and anisotropic models respectively and that the results suggest that the geometrical configuration of the ILT relative to the arterial wall may be a factor not only on ensuing peak wall stress, but also on its location within the lesion.

These findings opened a second line of investigation, which was to further investigate the role of the ILT, role that up to the date is very controversial. It is considered that the ILT generates a cushioning effect on the aneurismal wall stress, effect that may be compromised in fissured ILTs, however, a thick ILT layer is also known to weak the underlying AAA wall, and has also been suggested to increase AAA rupture risk. The aim of this second line was to investigate how ILT constitution and topology influence the magnitude and location of peak wall stress (PWS).

Through the results of 21 AAA models on which 2 ILT material models were considered: i) a Stiff thrombus and named Type A and ii) a more compliant thrombus named Type B, the following findings were encountered:

- No significant correlation between PWS and MPWS with AAA diameter were found, despite the PWS somehow increases with the diameter.
- A strong correlation between the MPWS and ILT volume was found, which indicate a significant influence of the ILT on wall stress.
- The topology of the ILT seem to play an important role on the PWS, as PWS were found to be located on ILT-free parts of the wall or on areas with minimum thickness.
- The PWS was found to be higher for the model using a softer (Type B) ILT material model. Consequently, a stiffer ILT is associated with a more pronounced reduction in the wall stress than a more compliant.
- The stress reduction in the wall when an ILT is present obeys to an overall increase in the AAA stiffness due to the presence of the ILT, which can be several times thicker than the wall, rather than a direct impact of the ILT’s mechanical stiffness.

Additionally, on those AAA with thick ILT, a heterogeneous spatial composition of soft and stiff thrombus tissue was considered. It was found that the stiffer layer in a heterogeneous ILT carries most of the load within the ILT; being the mean stress in the stiffer layer in some cases larger than the mean stress in the wall. These results suggest that the failing of the luminal layer could occur in a heterogeneous ILT before the wall fails, as previous studies have suggested as a cause of AAA rupture.

The work developed in this thesis has been published in two articles of the Annals of Biomedical Engineering (2013 and 2105) and two international conferences. An additional article is currently under review in the Journal of Biomechanical Engineering:

International Conferences:

- F Riveros, G Martufi, TC Gasser, JF Rodriguez. Influence of intraluminal thrombus topology on AAA passive mechanics. Computing in Cardiology Conference (CinC), 2013. ISBN 978-1-4779-0884-4.
- F Riveros, G Martufi, TC Gasser, JF Rodriguez. Influence of ILT mechanical behavior in abdominal aortic aneurysms passive mechanics. 11th World Congress on Computational Mechanics (WCCM XI)/5th European Conference on Computational Mechanics (ECCM V)/6th European Conference on Computational Fluid Dynamics (ECFD VI). July 20 - 25, 2014, Barcelona, Spain.

International Journals:

- F Riveros, S Chandra, E Finol, TC Gasser, JF Rodriguez. A pull-back algorithm to determine the unloaded vascular geometry in anisotropic hyperelastic AAA passive mechanics. Annals of Biomedical Engineering, Volume 41, Issue 4 (2013), Page 694-708. DOI:10.1007/s10439-012-0712-3
- F Riveros, G Martufi, TC Gasser, JF Rodriguez. On the impact of Intraluminal Thrombus mechanical behavior in AAA passive mechanics. Annals of Biomedical Engineering, (2015), *In press (Available online)*. DOI: 10.1007/s10439-015-1267-x.
- S Chandra, V Gnanaruban, F Riveros, JF Rodriguez, EA Finol. A Methodology for the Derivation of Unloaded Abdominal Aortic Aneurysm Geometry with Experimental Validation. Journal of Biomechancial Engineering, *In review.*

.

CONCLUSIONES

El principal objetivo de esta tesis era ahondar en el conocimiento de la biomecánica pasiva de Aneurismas Aórticos Abdominales; buscando resultados que puedan llegar a complementar el criterio médico de cirugía de reparación, el cual se basa principalmente en el diámetro del AAA y en la tasa de crecimiento del ILT, pero dejando a un lado otras características del tejido que han mostrado afectar a la integridad biomecánica de la pared arterial ya sea para bien o para mal.

El primer objetivo fue el desarrollar un algoritmo que permitiese una mejor estimación del campo de tensiones de una AAA. El llamado “Algoritmo Cero Presión” permite determinar la geometría despresurizada de un AAA, ta que, al usar esta geometría y aplicar la presión sistólica para encontrar un campo de tensiones más realista comparado con lo que se ha hecho hasta la fecha, que ha sido usar la geometría presurizada basada en imágenes de CT (usualmente sujetas a la presión diastólica), y a esta aplicarle directamente la presión sistólica.

El algoritmo propuesto fue validado con tres experimentos in-silico y rigurosamente probado por medios experimentales. La capacidad del algoritmo para identificar la configuración cero-presión fue claramente demostrado en ambas metodologías. Adicionalmente, el algoritmo ha sido aplicado en al menos 30 modelos de AAA durante esta tesis, en todos ellos incluyendo el ILT, el cual ha sido obviado en otros estudios. La principal ventaja de este algoritmo es que: toma en cuenta la anisotropía del tejido, preserva el volumen global del tejido por lo tanto garantizando la incompresibilidad; y que la geometría cero-presión se puede encontrar en un número razonable de iteraciones (menos de 6 en promedio) con una precisión igual a la resolución de las imágenes CT. Aunque este algoritmo fue desarrollado para AAAs, puede ser aplicado a una variedad de estructuras biológicas bajo presión, e.g. el corazón, aurículas y aneurismas cerebrales entre otros.

Los principales resultados al aplicar el algoritmo cero-presión a 12 modelos de AAAs fue que la PWS es desestimada en un 21% (desv. estándar

17%) y un 14% (desv. estándar 14%), para modelos de material de la pared arterial isótropos y anisótropos respectivamente, si se emplea la geometría CT en lugar de la geometría cero presión. Los resultados sugieren que la configuración geométrica del ILT relativa a la pared arterial puede ser un factor que no solo afecta la PWS, pero también su localización dentro de la lesión.

Estos resultados abrieron una segunda línea de investigación, la cual fue investigar en mayor detalle el papel del ILT, papel que hasta la fecha es controversial. Se considera que el ILT genera un efecto amortiguante sobre la tensión de la pared arterial, efecto que puede ser comprometido por la aparición de fisuras en el ILT. Por el contrario, un ILT grueso se sabe que debilita la pared arterial subyacente, y también ha sido sugerido que incrementa el riesgo de ruptura. El objetivo de esta segunda parte fue investigar como la constitución y topología del ILT influyen en la magnitud y localización de la PWS.

Un estudio en 21 AAAs en los cuales 2 modelos de material de ILT fueron considerados: i) Un trombo rígido denominado Tipo A y ii) un trombo más flexible denominado tipo B, arrojaron los siguientes resultados:

- No se encontró una correlación significativa entre la PWS y la MPWS y el diámetro del AAA, a pesar de que la PWS muestra una tendencia de incrementar con el diámetro
- Se encontró una fuerte correlación entre la MPWS y el volumen del ILT, lo cual indica la influencia que el ILT tiene sobre la tensión de la pared.
- La topología del ILT juega un papel importante en la PWS, ya que se ha encontrado que la PWS se localiza en lugares de la pared arterial sin ILT, o en áreas de la sección donde el espesor el ILT es mínimo.
- Se encontró que la PWS es mayor en aquellos modelos en los que el ILT se modeló con el material flexible (tipo B). En consecuencia, un ILT más rígido se asocia con una mayor reducción de la tensión de la pared arterial que con uno más flexible.
- La reducción de tensión en la pared cuando está presente el ILT obedece a un incremento total de la rigidez del AAA debido a la

presencia del ILT, cuyo espesor puede ser varias veces el espesor de la pared, y no a un impacto directo de la rigidez mecánica del tejido del ILT.

Adicionalmente, en aquellos AAAs con ILT de espesor considerable, se consideró un ILT heterogéneo compuesto una capa de trombo flexible y otra de trombo rígido. Se encontró que la capa rígida en un ILT heterogéneo absorbe la mayor parte de la carga entre todo el ILT; siendo la tensión media en la capa rígida en algunos casos mayor que la tensión media de la pared. Estos resultados sugieren que una ruptura en la pared luminal puede ocurrir en un ILT heterogéneo antes de que falle la pared arterial, siendo una causa posible de ruptura de AAA.

El trabajo desarrollado en esta tesis has sido publicado en dos artículos del Annals of Biomedical Engineering (2013 y 2015) y en dos conferencias internacionales. Un tercer artículo en el Journal of Biomechanical Engineering se encuentra actualmente en revisión:

Conferencias Internacionales:

- F Riveros, G Martufi, TC Gasser, JF Rodriguez. Influence of intraluminal thrombus topology on AAA passive mechanics. Computing in Cardiology Conference (CinC), 2013. ISBN 978-1-4779-0884-4.
- F Riveros, G Martufi, TC Gasser, JF Rodriguez. Influence of ILT mechanical behavior in abdominal aortic aneurysms passive mechanics. 11th World Congress on Computational Mechanics (WCCM XI)/5th European Conference on Computational Mechanics (ECCM V)/6th European Conference on Computational Fluid Dynamics (ECFD VI). July 20 - 25, 2014, Barcelona, Spain.

International Journals:

- F Riveros, S Chandra, E Finol, TC Gasser, JF Rodriguez. A pull-back algorithm to determine the unloaded vascular geometry in anisotropic hyperelastic AAA passive mechanics. Annals of Biomedical Engineering, Volume 41, Issue 4 (2013), Page 694-708. DOI:10.1007/s10439-012-0712-3
- F Riveros, G Martufi, TC Gasser, JF Rodriguez. On the impact of Intraluminal Thrombus mechanical behavior in AAA passive mechanics.

Annals of Biomedical Engineering, (2015), *In press (Available online)*. DOI: 10.1007/s10439-015-1267-x.

- S Chandra, V Gnanaruban, F Riveros, JF Rodriguez, EA Finol. A Methodology for the Derivation of Unloaded Abdominal Aortic Aneurysm Geometry with Experimental Validation. Journal of Biomechancial Engineering, *In review.*

APPENDIX A

8. APPENDIX A

This appendix presents the Maximum Principal Stress results for 21 AAAs models as reference in chapter 6.2 (On the impact of Intraluminal Thrombus mechanical behavior in AAA passive mechanics).

Results are presented for ILT using Type A (equation 7) and Type B (equation 8) material models and all AAAs modeled with the following characteristics:

- Aneurysmal wall tissue has been modeled as hyperelastic Anisotropic (Equation 6).
- The Pull Back algorithm has been applied to all models.
- Systolic pressure of 120 mm Hg to the ZP configuration

MODEL B1		
PWS Type A ILT (Pa)	PWS Type B ILT (Pa)	PWS ratio Type A/Type B
300	330	1.11

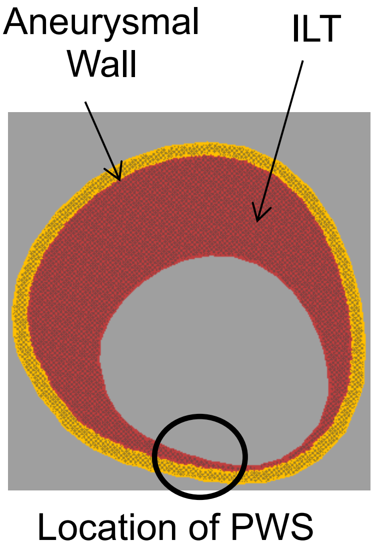
Aneurysmal Wall
ILT
Location of PWS

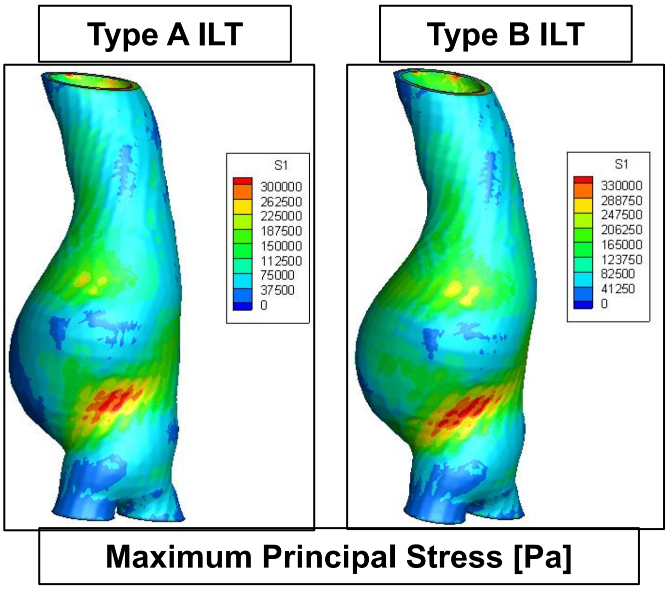
Type A ILT
Type B ILT
S1
300000
262500
225000
187500
150000
112500
75000
37500
0
S1
330000
288750
247500
206250
165000
123750
82500
41250
0
Maximum Principal Stress [Pa]

MODEL B2		
PWS Type A ILT (Pa)	PWS Type B ILT (Pa)	PWS ratio Type A/Type B
310	360	1.16

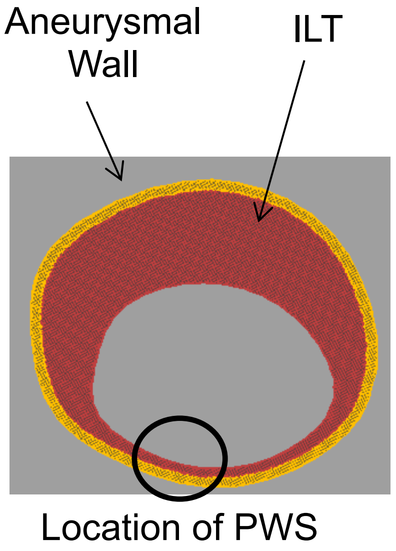
Aneurysmal Wall
ILT
Location of PWS

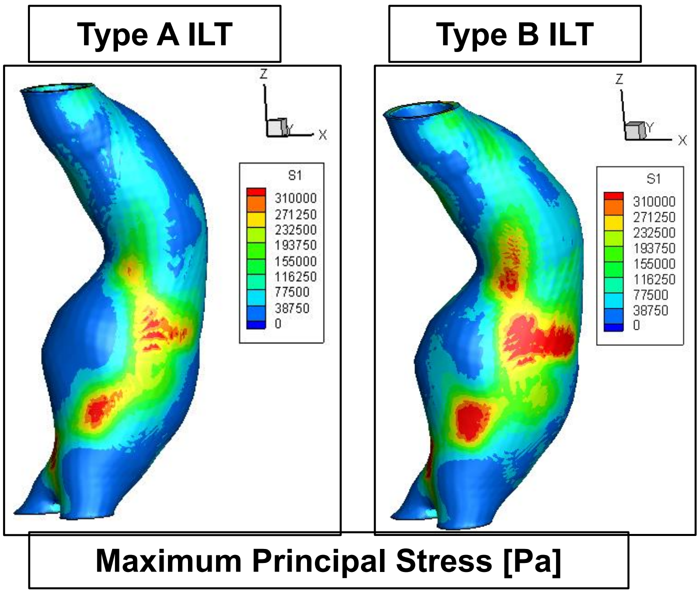
Type A ILT
Type B ILT
Z
X
Y
S1
310000
271250
232500
193750
155000
116250
77500
38750
0
Maximum Principal Stress [Pa]

MODEL B3		
PWS Type A ILT (Pa)	PWS Type B ILT (Pa)	PWS ratio Type A/Type B
450	480	1.07

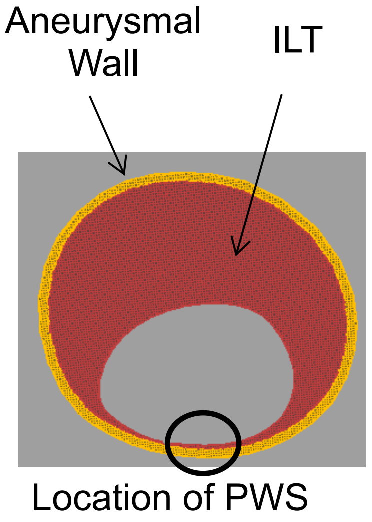
Aneurysmal Wall
ILT
Location of PWS

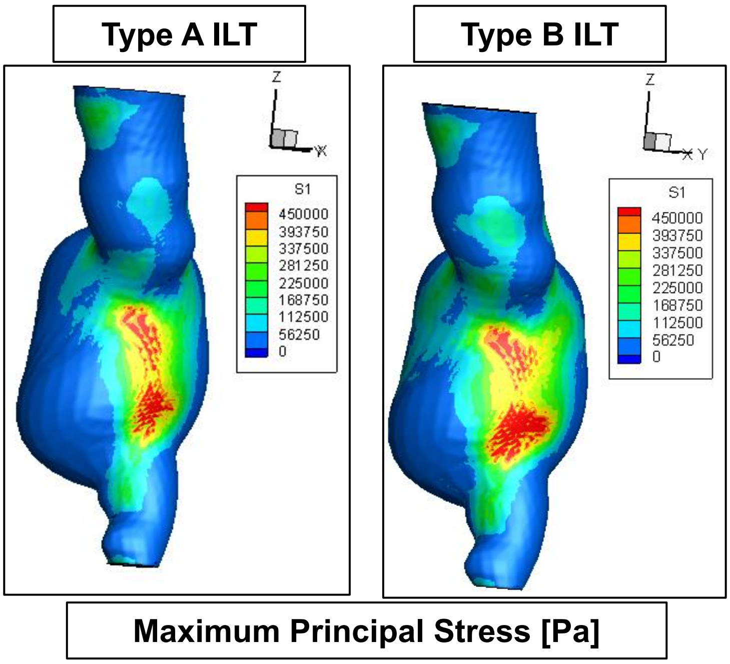
Type A ILT
Type B ILT
Z
X
Y
S1
450000
393750
337500
281250
225000
168750
112500
56250
0
Maximum Principal Stress [Pa]

MODEL B4		
PWS Type A ILT (Pa)	PWS Type B ILT (Pa)	PWS ratio Type A/Type B
200	320	1.60

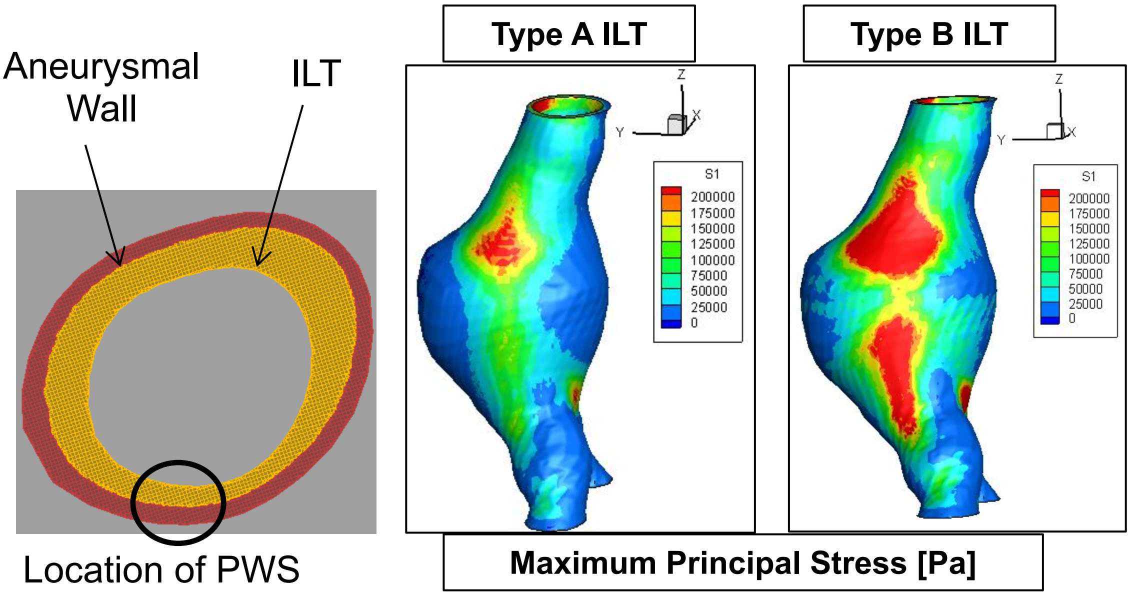
Aneurysmal Wall
ILT
Location of PWS
Type A ILT
Type B ILT
Z
Y
X
S1
200000
175000
150000
125000
100000
75000
50000
25000
0
Maximum Principal Stress [Pa]

MODEL B5		
PWS Type A ILT (Pa)	PWS Type B ILT (Pa)	PWS ratio Type A/Type B
300	440	1.47

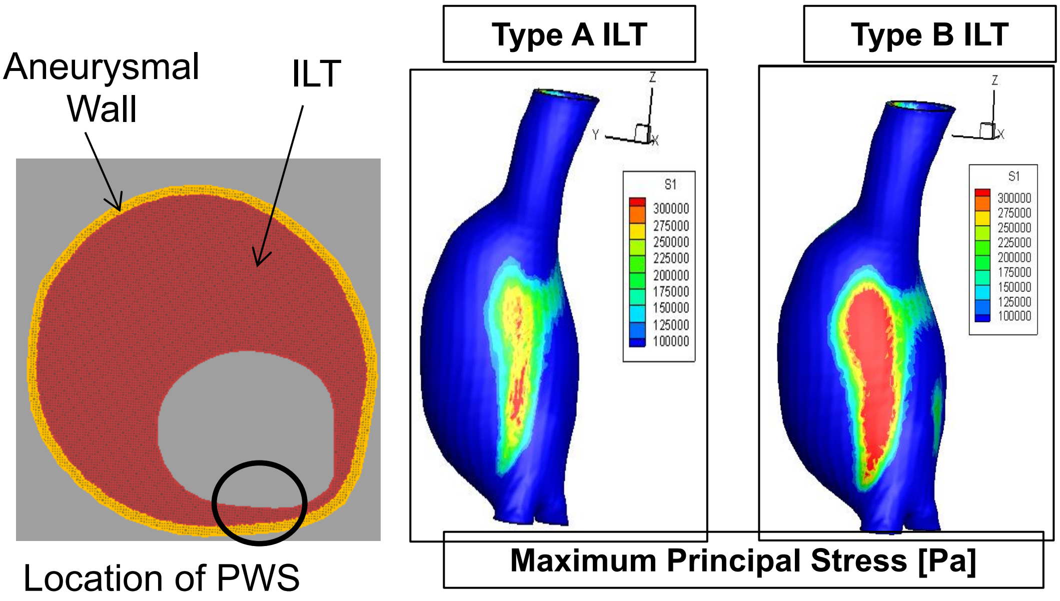
Aneurysmal Wall
ILT
Location of PWS
Type A ILT
Type B ILT
Z
Y
X
S1
300000
275000
250000
225000
200000
175000
150000
125000
100000
Maximum Principal Stress [Pa]

MODEL B6

PWS Type A ILT (Pa)	PWS Type B ILT (Pa)	PWS ratio Type A/Type B
310	390	1.26

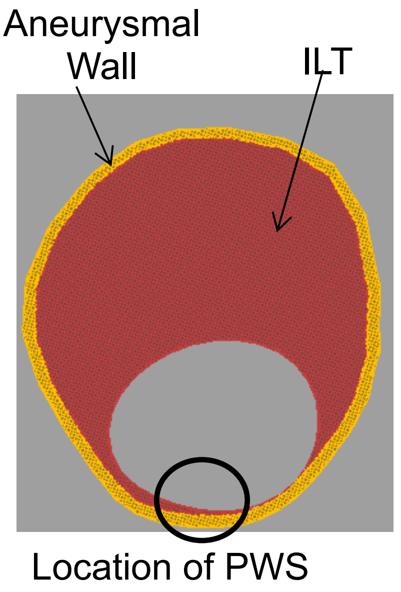
Aneurysmal Wall
ILT
Location of PWS

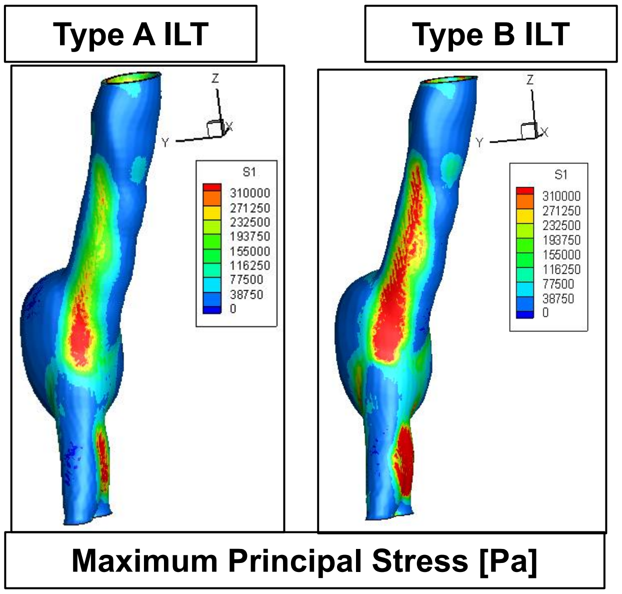
Type A ILT
Type B ILT
Z
Y
X
S1
310000
271250
232500
193750
155000
116250
77500
38750
0
Maximum Principal Stress [Pa]

MODEL B7

PWS Type A ILT (Pa)	PWS Type B ILT (Pa)	PWS ratio Type A/Type B
580	600	1.03

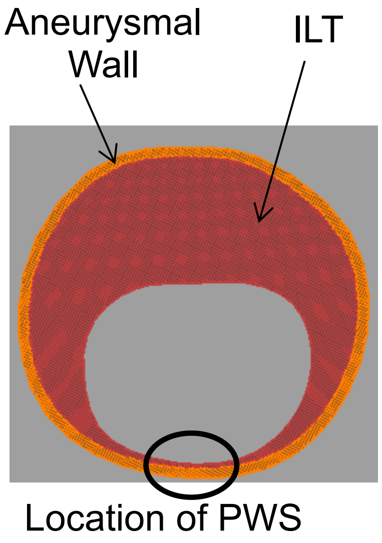
Aneurysmal Wall
ILT
Location of PWS

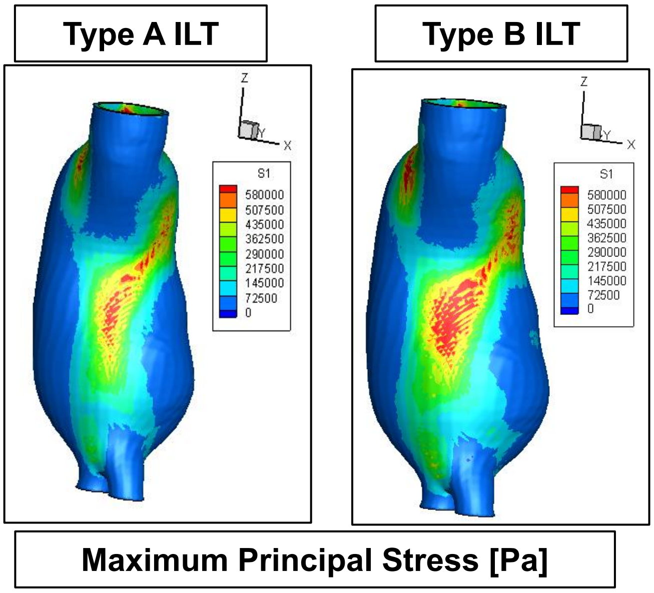
Type A ILT
Type B ILT
Z
Y
X
S1
580000
507500
435000
362500
290000
217500
145000
72500
0
Maximum Principal Stress [Pa]

MODEL B8		
PWS Type A ILT (Pa)	PWS Type B ILT (Pa)	PWS ratio Type A/Type B
250	320	1.28

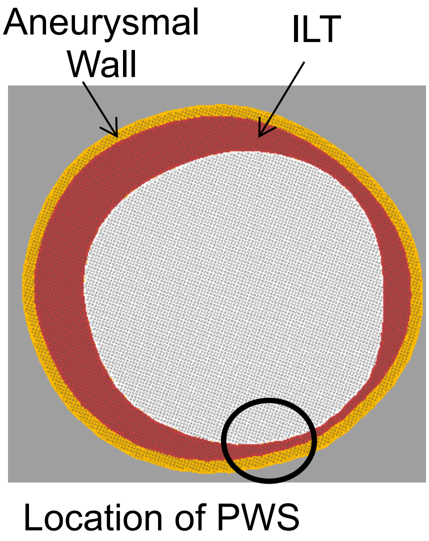
Aneurysmal Wall
ILT
Location of PWS

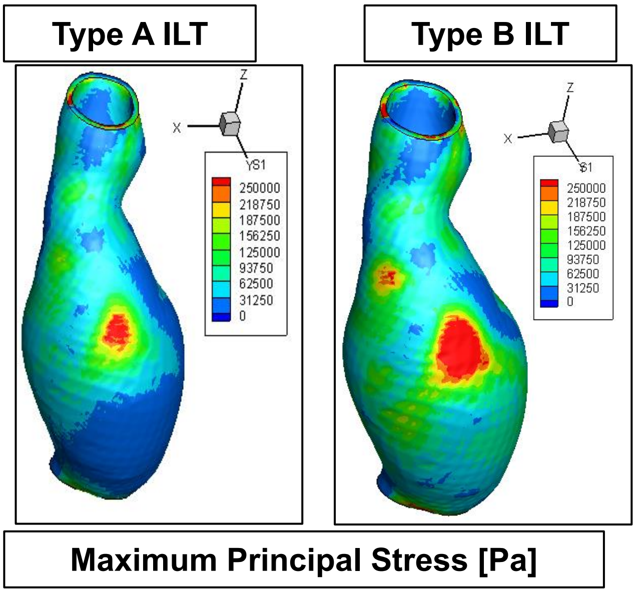
Type A ILT
Type B ILT
Z
X
S1
250000
218750
187500
156250
125000
93750
62500
31250
0
Maximum Principal Stress [Pa]

MODEL B9		
PWS Type A ILT (Pa)	PWS Type B ILT (Pa)	PWS ratio Type A/Type B
300	410	1.37

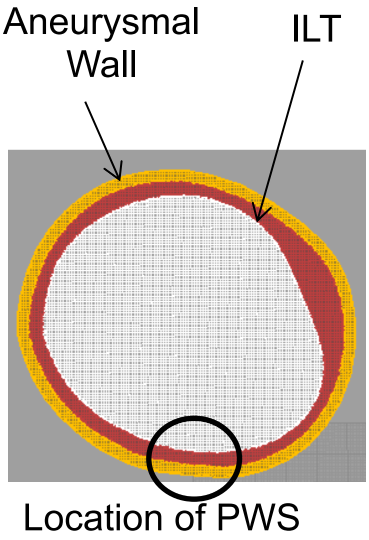
Aneurysmal Wall
ILT
Location of PWS

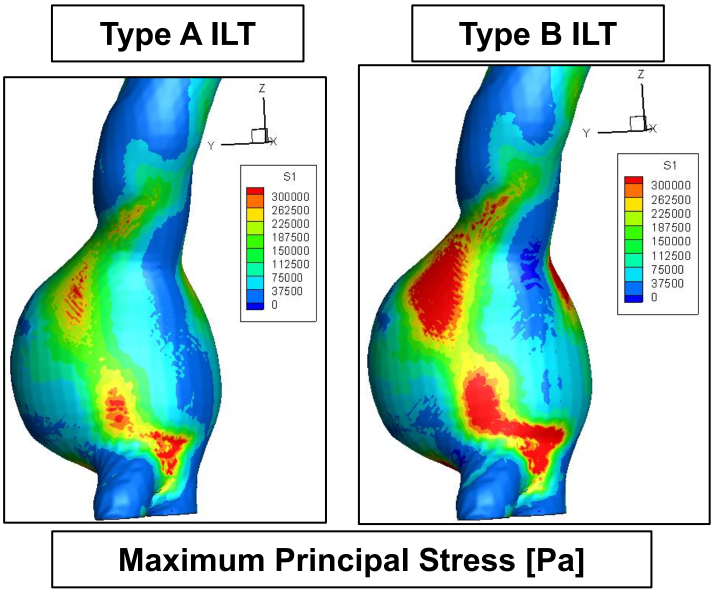
Type A ILT
Type B ILT
Z
Y
X
S1
300000
262500
225000
187500
150000
112500
75000
37500
0
Maximum Principal Stress [Pa]

MODEL B10		
PWS Type A ILT (Pa)	PWS Type B ILT (Pa)	PWS ratio Type A/Type B
480	570	1.19

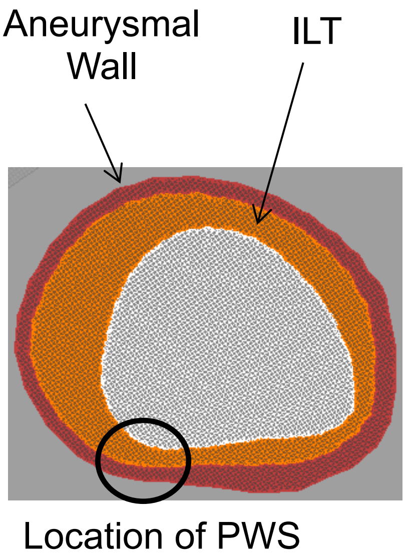
Aneurysmal Wall
ILT
Location of PWS

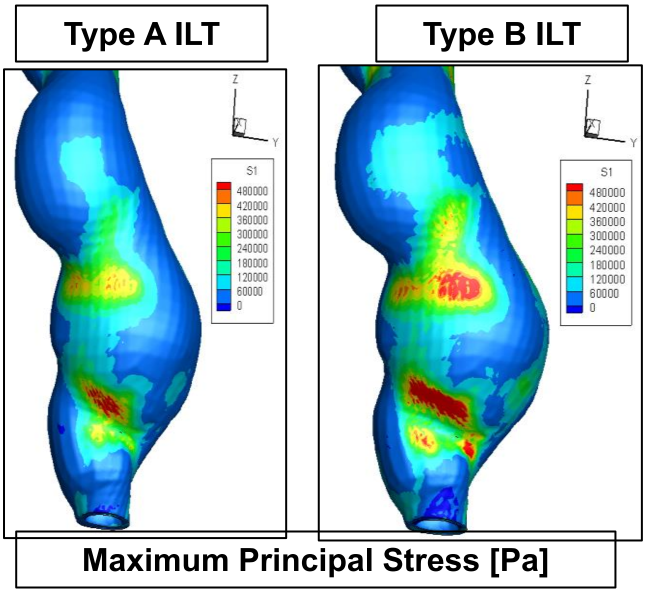
Type A ILT
Type B ILT
Z
Y
S1
480000
420000
360000
300000
240000
180000
120000
60000
0
Maximum Principal Stress [Pa]

MODEL B11		
PWS Type A ILT (Pa)	PWS Type B ILT (Pa)	PWS ratio Type A/Type B
440	500	1.14

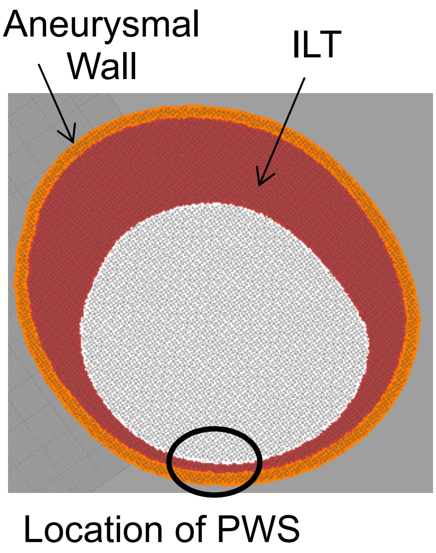
Aneurysmal Wall
ILT
Location of PWS

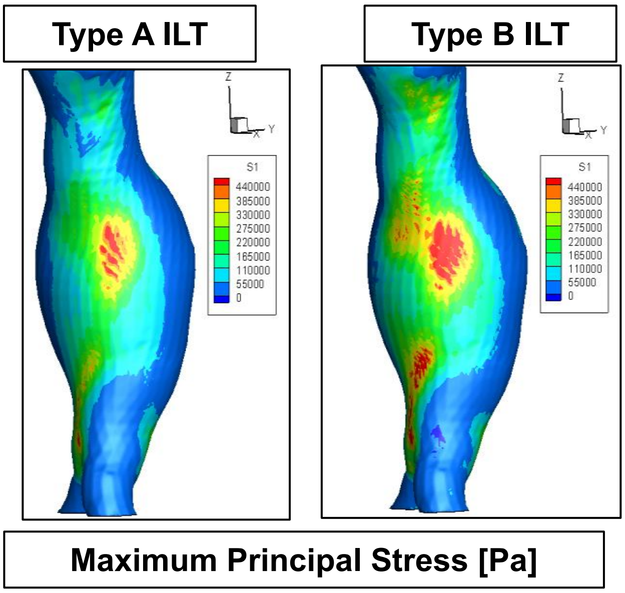
Type A ILT
Type B ILT
Z
Y
X
S1
440000
385000
330000
275000
220000
165000
110000
55000
0
Maximum Principal Stress [Pa]

MODEL B12

PWS Type A ILT (Pa)	PWS Type B ILT (Pa)	PWS ratio Type A/Type B
550	600	1.09

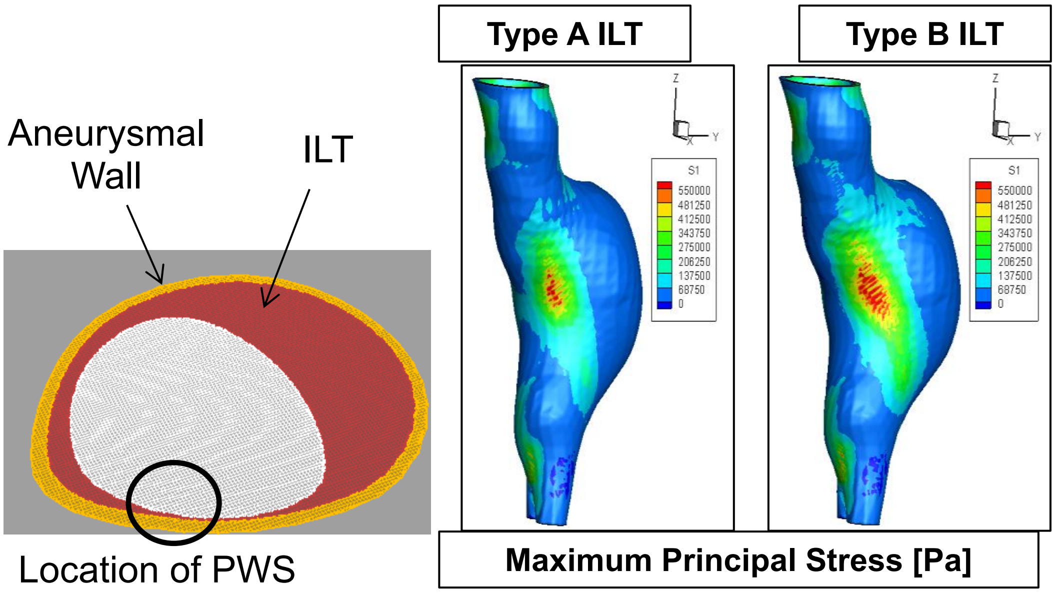
Aneurysmal Wall
ILT
Location of PWS
Type A ILT
Type B ILT
Z
Y
X
S1
550000
481250
412500
343750
275000
206250
137500
68750
0
Maximum Principal Stress [Pa]

MODEL B13

PWS Type A ILT (Pa)	PWS Type B ILT (Pa)	PWS ratio Type A/Type B
300	400	1.33

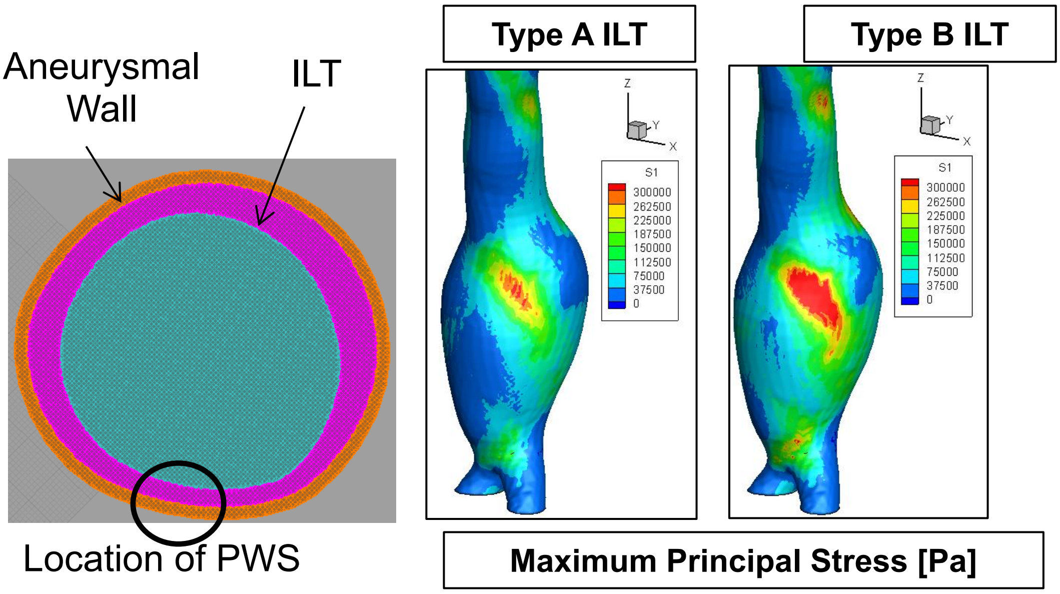
Aneurysmal Wall
ILT
Location of PWS
Type A ILT
Type B ILT
Z
Y
X
S1
300000
262500
225000
187500
150000
112500
75000
37500
0
Maximum Principal Stress [Pa]

MODEL B14		
PWS Type A ILT (Pa)	PWS Type B ILT (Pa)	PWS ratio Type A/Type B
500	620	1.24

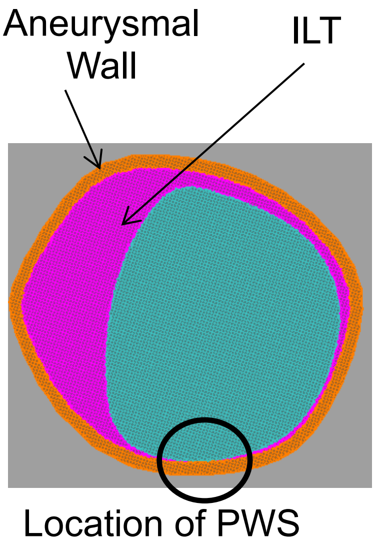
Aneurysmal Wall
ILT
Location of PWS

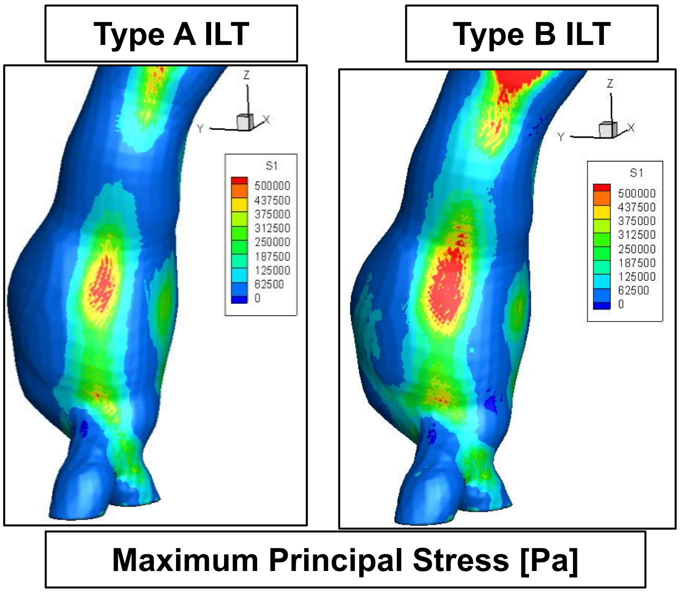
Type A ILT
Type B ILT
Z
Y
X
S1
500000
437500
375000
312500
250000
187500
125000
62500
0
Maximum Principal Stress [Pa]

MODEL B15		
PWS Type A ILT (Pa)	PWS Type B ILT (Pa)	PWS ratio Type A/Type B
370	500	1.35

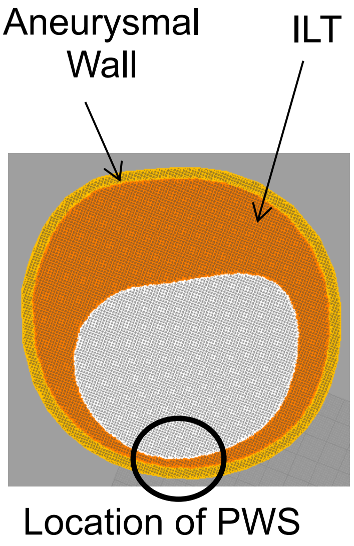
Aneurysmal Wall
ILT
Location of PWS

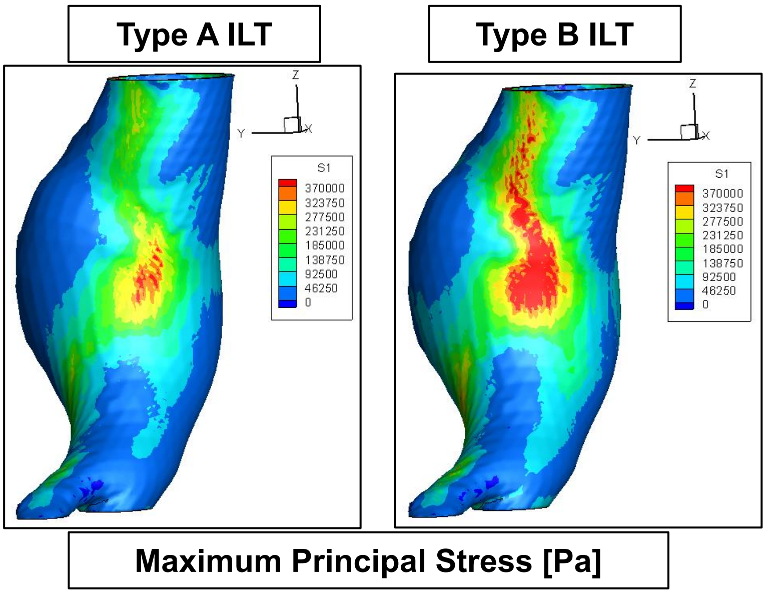
Type A ILT
Type B ILT
Z
Y
X
S1
370000
323750
277500
231250
185000
138750
92500
46250
0
Maximum Principal Stress [Pa]

MODEL B16		
PWS Type A ILT (Pa)	PWS Type B ILT (Pa)	PWS ratio Type A/Type B
540	600	1.11

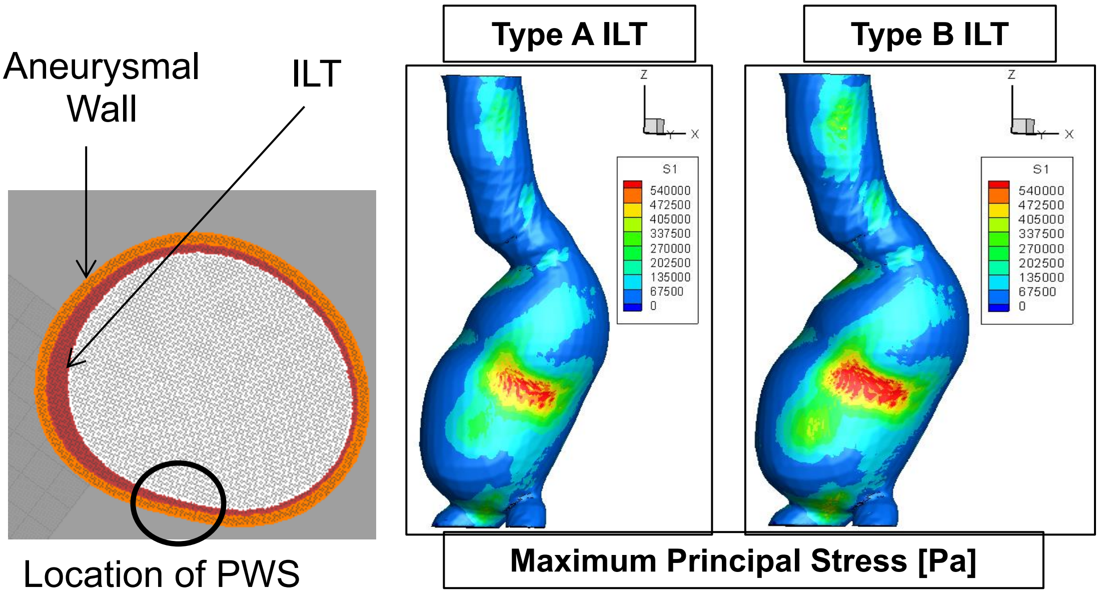
Aneurysmal Wall
ILT
Location of PWS
Type A ILT
Type B ILT
Z
Y
X
S1
540000
472500
405000
337500
270000
202500
135000
67500
0
Maximum Principal Stress [Pa]

MODEL B17		
PWS Type A ILT (Pa)	PWS Type B ILT (Pa)	PWS ratio Type A/Type B
290	480	1.66

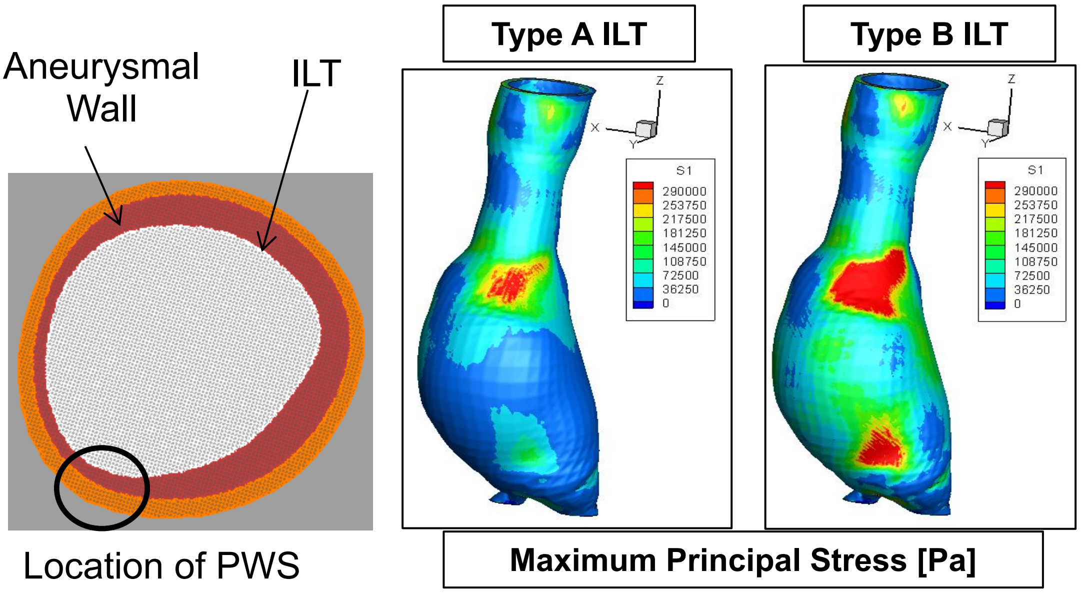
Aneurysmal Wall
ILT
Location of PWS
Type A ILT
Type B ILT
Z
X
Y
S1
290000
253750
217500
181250
145000
108750
72500
36250
0
Maximum Principal Stress [Pa]

MODEL B18		
PWS Type A ILT (Pa)	PWS Type B ILT (Pa)	PWS ratio Type A/Type B
700	700	1.00

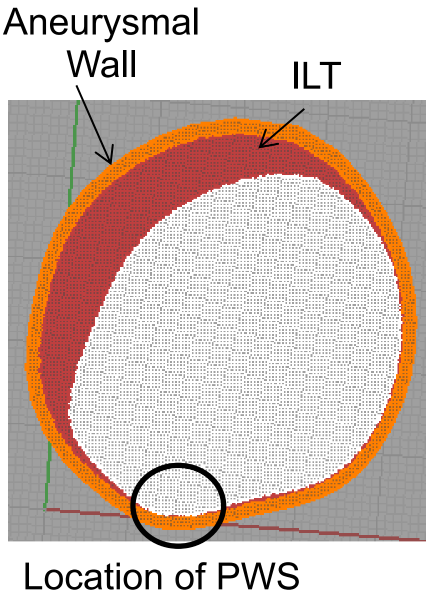
Aneurysmal Wall
ILT
Location of PWS

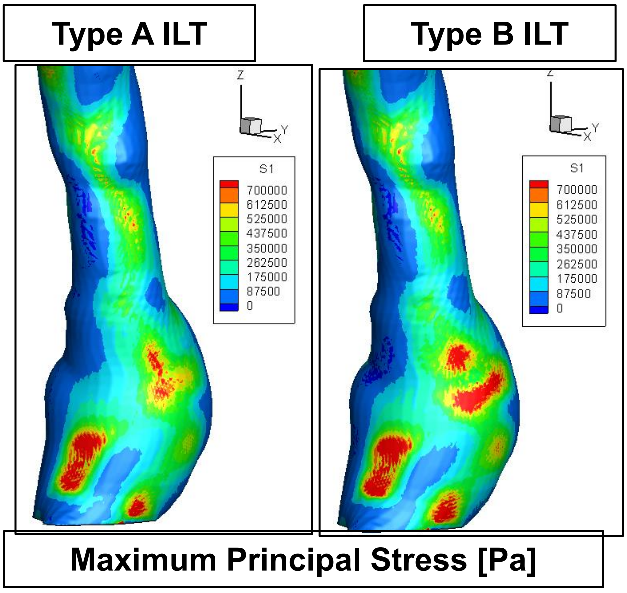
Type A ILT
Type B ILT
Z
Y
X
S1
700000
612500
525000
437500
350000
262500
175000
87500
0
Maximum Principal Stress [Pa]

MODEL B19		
PWS Type A ILT (Pa)	PWS Type B ILT (Pa)	PWS ratio Type A/Type B
850	850	1.00

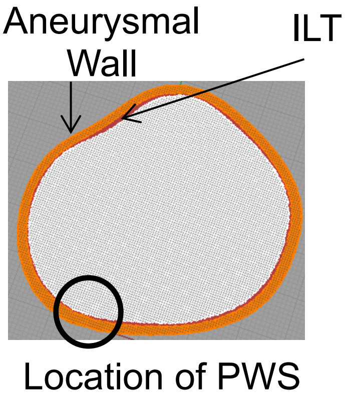
Aneurysmal Wall
ILT
Location of PWS

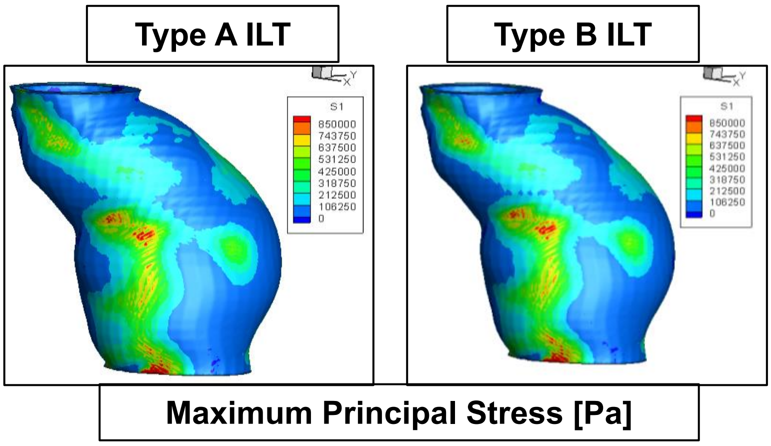
Type A ILT
Type B ILT
Y
X
S1
850000
743750
637500
531250
425000
318750
212500
106250
0
Maximum Principal Stress [Pa]

MODEL B20		
PWS Type A ILT (Pa)	PWS Type B ILT (Pa)	PWS ratio Type A/Type B
260	390	1.50

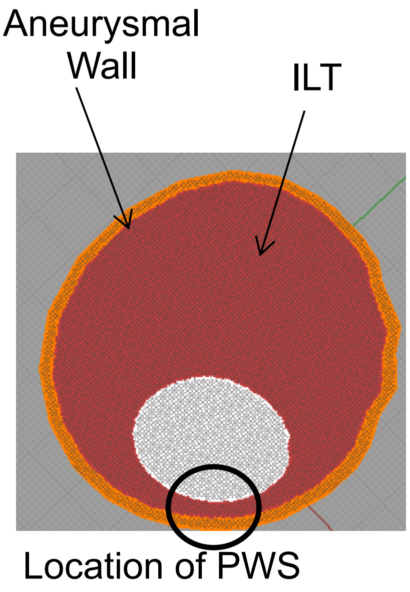
Aneurysmal Wall
ILT
Location of PWS

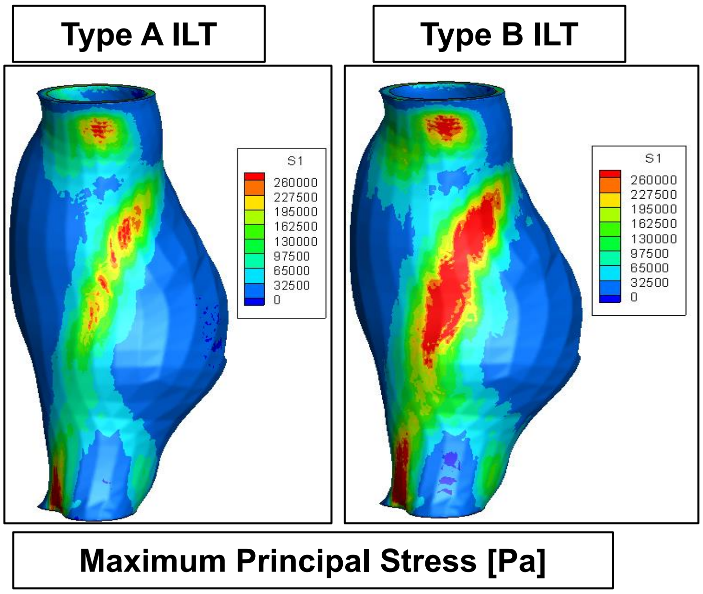
Type A ILT
Type B ILT
S1
260000
227500
195000
162500
130000
97500
65000
32500
0
S1
260000
227500
195000
162500
130000
97500
65000
32500
0
Maximum Principal Stress [Pa]

MODEL B21		
PWS Type A ILT (Pa)	PWS Type B ILT (Pa)	PWS ratio Type A/Type B
700	700	1.00

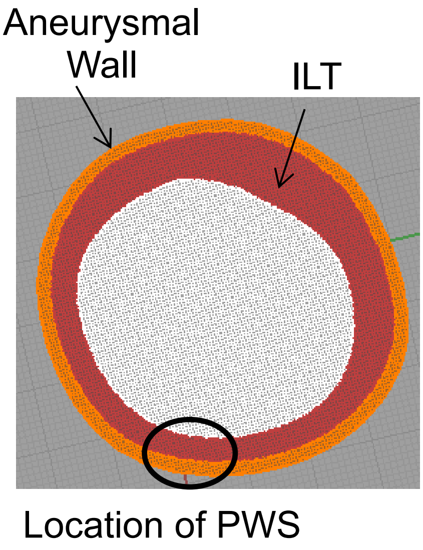
Aneurysmal Wall
ILT
Location of PWS

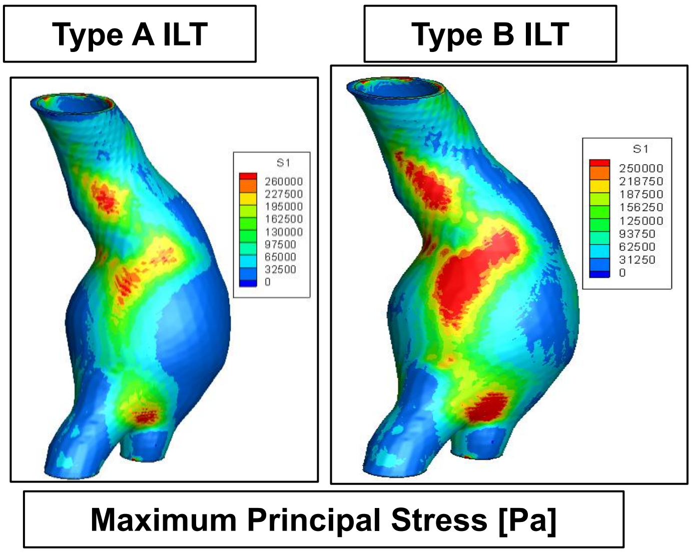
Type A ILT
Type B ILT
S1
260000
227500
195000
162500
130000
97500
65000
32500
0
S1
250000
218750
187500
156250
125000
93750
62500
31250
0
Maximum Principal Stress [Pa]

APPENDIX B

SARAVGVSTANAE ✝ ST
S

9. APPENDIX B

This appendix presents the results for 21 AAAs models as reference in chapter 6.2 (On the impact of Intraluminal Thrombus mechanical behavior in AAA passive mechanics) for the following ratio:

$$Ratio = \frac{Wall\ Principal\ Max\ Stress\ of\ AAA\ without\ ILT}{Wall\ Principal\ Max\ Stress\ of\ AAA\ with\ ILT}$$

Results are presented for ILT using Type A (equation 7) and Type B (equation 8) material models. For each model the Figure on the left shows a cut of the AAA showing the wall in blue and the ILT in Red.

MODEL B1	
Type A ILT (-)	Type B ILT (-)
40	2

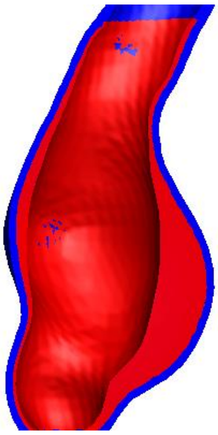

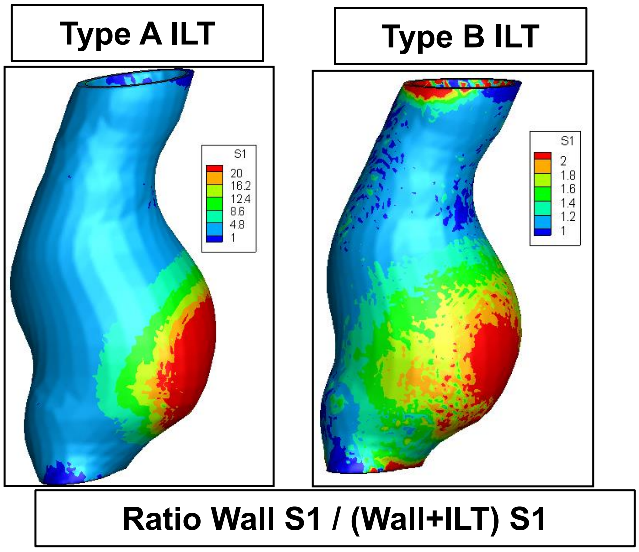
Type A ILT
Type B ILT
S1
20
16.2
12.4
8.6
4.8
1
S1
2
1.8
1.6
1.4
1.2
1
Ratio Wall S1 / (Wall+ILT) S1

MODEL B2

Type A ILT (-)	Type B ILT (-)
20	2.1

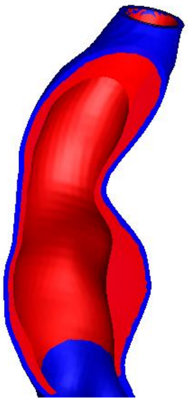

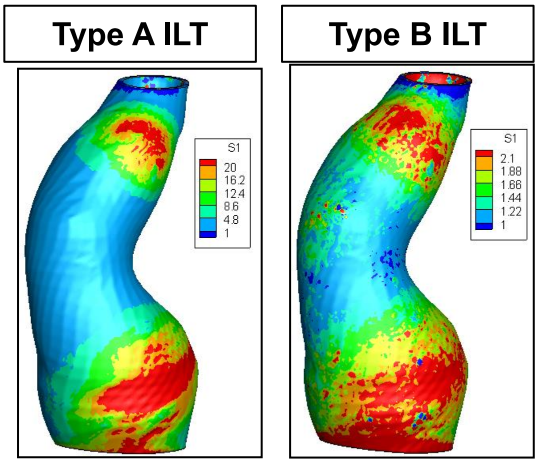
Type A ILT
Type B ILT
S1
20
16.2
12.4
8.6
4.8
1
S1
2.1
1.88
1.66
1.44
1.22
1

Ratio Wall S1 / (Wall+ILT) S1

MODEL B3

Type A ILT (-)	Type B ILT (-)
50	2.5

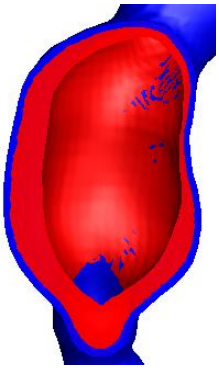

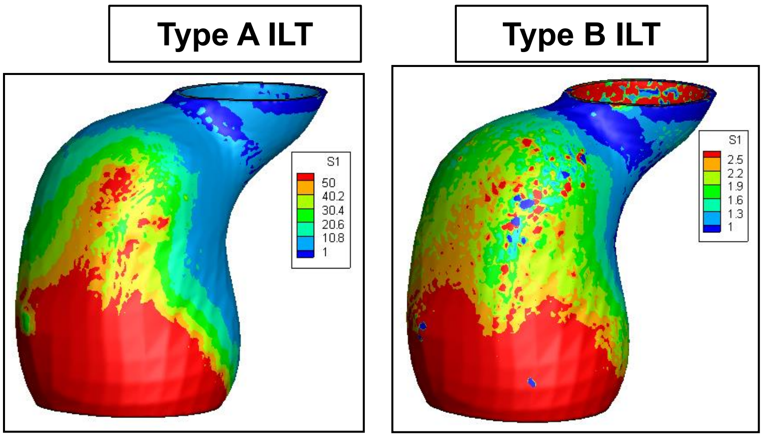
Type A ILT
Type B ILT
S1
50
40.2
30.4
20.6
10.8
1
S1
2.5
2.2
1.9
1.6
1.3
1

Ratio Wall S1 / (Wall+ILT) S1

MODEL B4

Type A ILT (-)	Type B ILT (-)
70	2

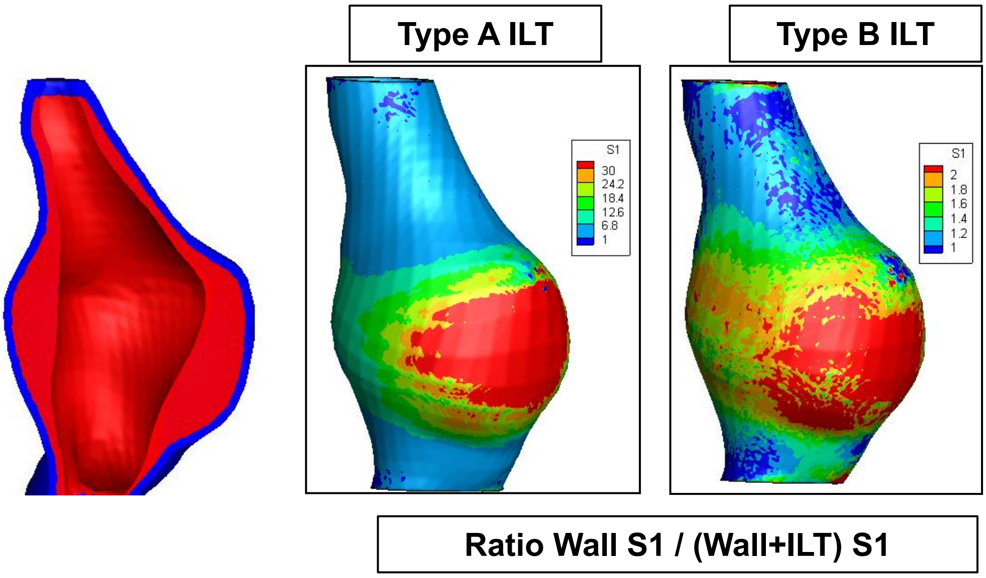
Type A ILT
Type B ILT
S1
30
24.2
18.4
12.6
6.8
1
S1
2
1.8
1.6
1.4
1.2
1
Ratio Wall S1 / (Wall+ILT) S1

MODEL B5

Type A ILT (-)	Type B ILT (-)
250	4.5

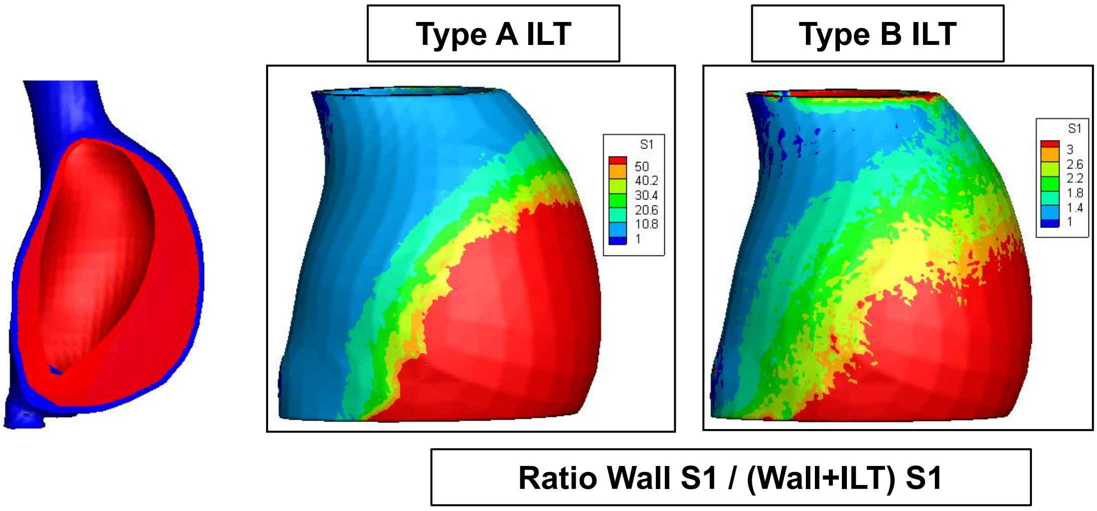
Type A ILT
Type B ILT
S1
50
40.2
30.4
20.6
10.8
1
S1
3
2.6
2.2
1.8
1.4
1
Ratio Wall S1 / (Wall+ILT) S1

MODEL B6	
Type A ILT (-)	Type B ILT (-)
1500	10

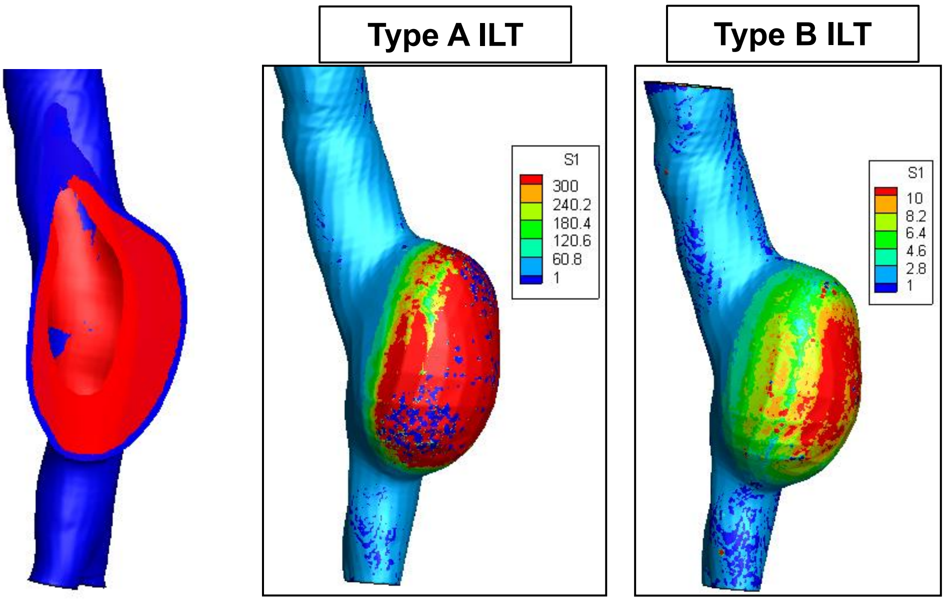
Type A ILT
Type B ILT
S1
300
240.2
180.4
120.6
60.8
1
S1
10
8.2
6.4
4.6
2.8
1

Ratio Wall S1 / (Wall+ILT) S1

MODEL B7	
Type A ILT (-)	Type B ILT (-)
100	2.4

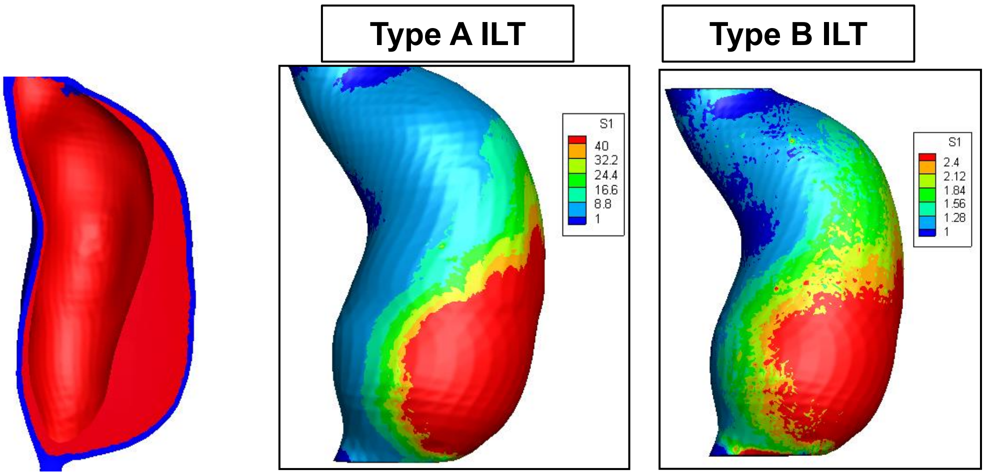
Type A ILT
Type B ILT
S1
40
32.2
24.4
16.6
8.8
1
S1
2.4
2.12
1.84
1.56
1.28
1

Ratio Wall S1 / (Wall+ILT) S1

MODEL B8	
Type A ILT (-)	Type B ILT (-)
8	1.5

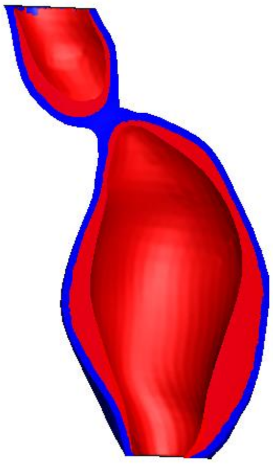

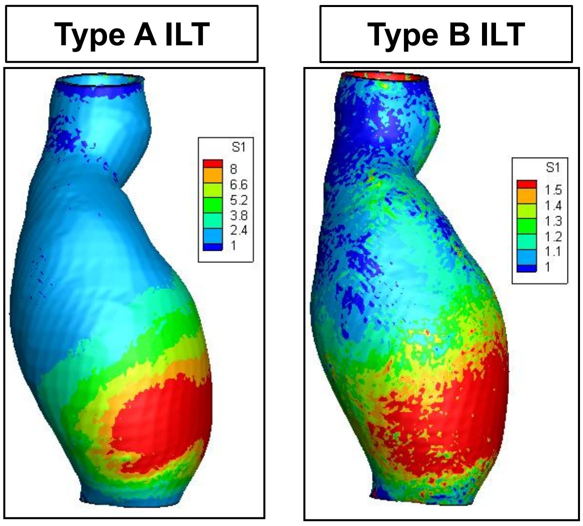
Type A ILT

Type B ILT

S1
8
6.6
5.2
3.8
2.4
1
S1
1.5
1.4
1.3
1.2
1.1
1

Ratio Wall S1 / (Wall+ILT) S1

MODEL B9	
Type A ILT (-)	Type B ILT (-)
1.7	1.15

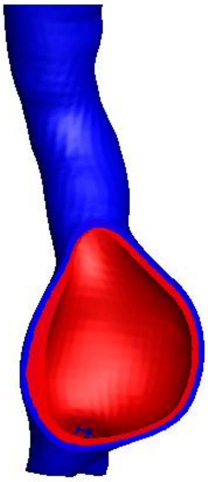

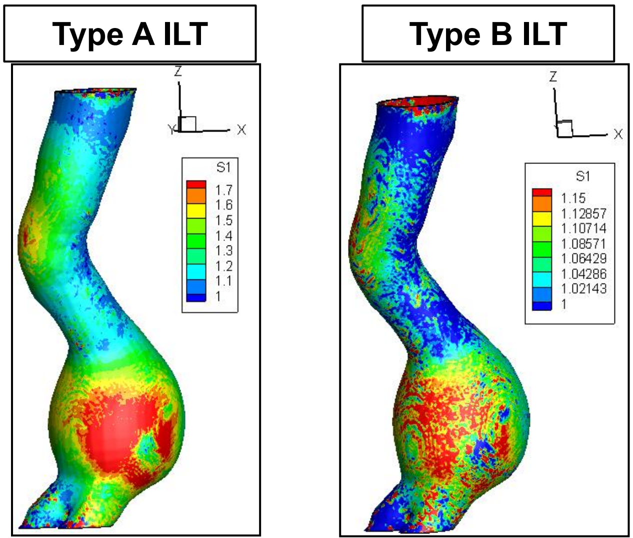
Type A ILT

Type B ILT

Z
Y
X
S1
1.7
1.6
1.5
1.4
1.3
1.2
1.1
1
Z
X
S1
1.15
1.12857
1.10714
1.08571
1.06429
1.04286
1.02143
1

Ratio Wall S1 / (Wall+ILT) S1

MODEL B10

Type A ILT (-)	Type B ILT (-)
4	1.3

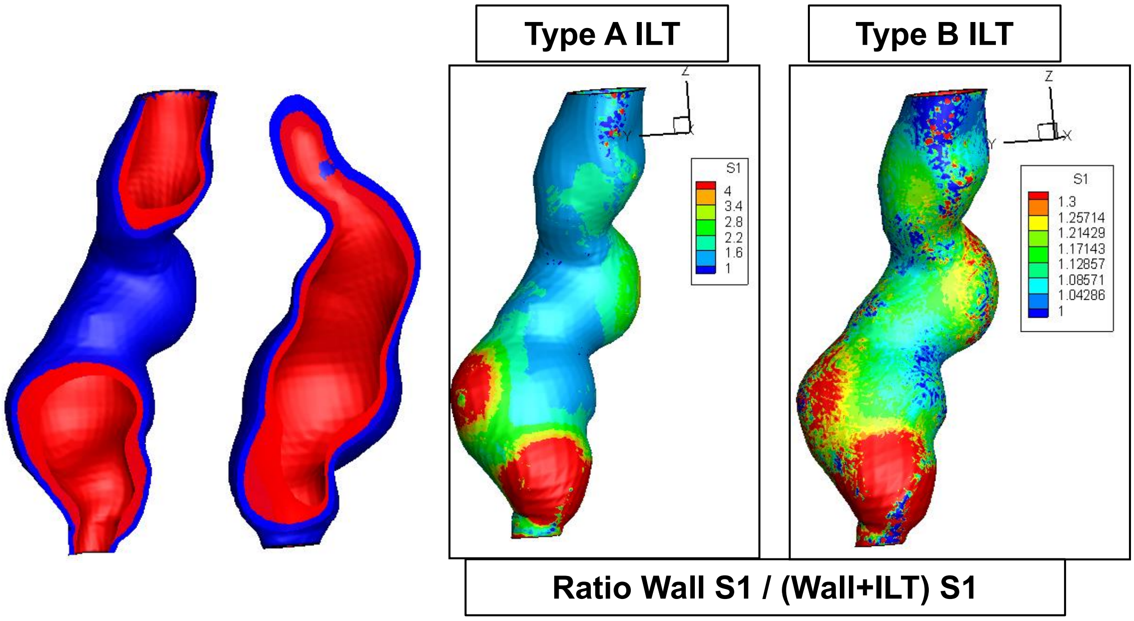
Type A ILT
Type B ILT
Z
Y
X
S1
4
3.4
2.8
2.2
1.6
1
Z
Y
X
S1
1.3
1.25714
1.21429
1.17143
1.12857
1.08571
1.04286
1
Ratio Wall S1 / (Wall+ILT) S1

MODEL B11

Type A ILT (-)	Type B ILT (-)
8	1.6

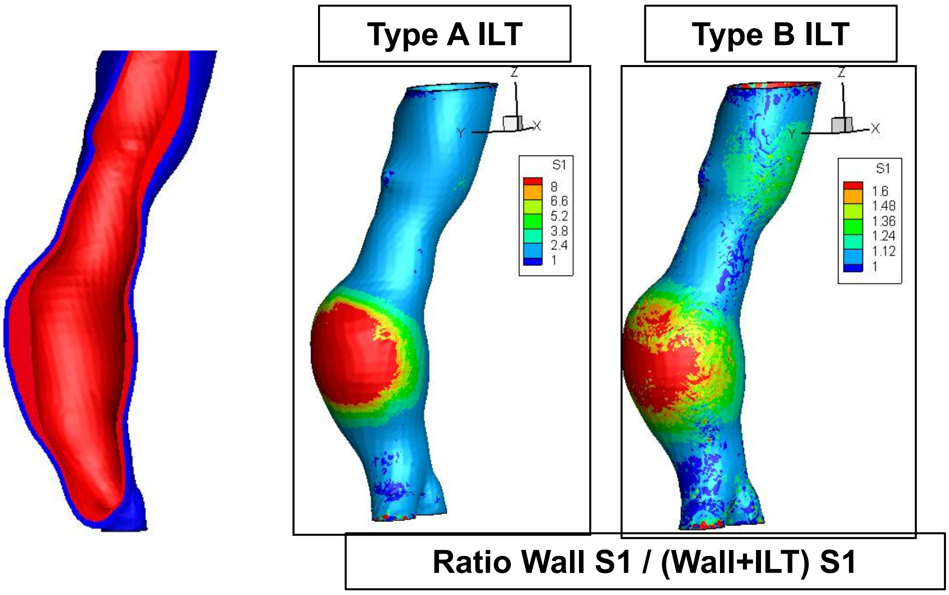
Type A ILT
Type B ILT
Z
Y
X
S1
8
6.6
5.2
3.8
2.4
1
Z
Y
X
S1
1.6
1.48
1.36
1.24
1.12
1
Ratio Wall S1 / (Wall+ILT) S1

MODEL B12

Type A ILT (-)	Type B ILT (-)
10	2

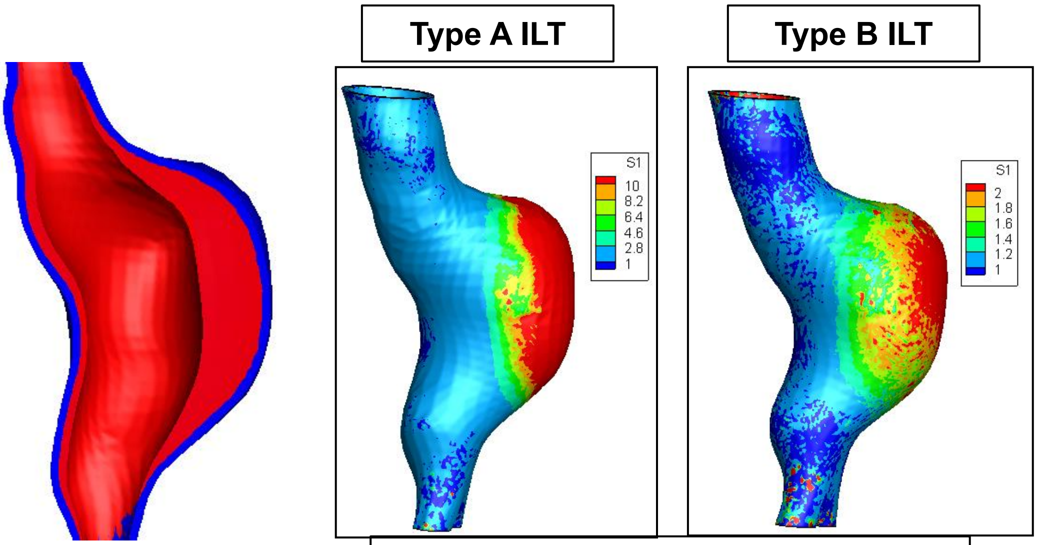
Type A ILT
Type B ILT
S1
10
8.2
6.4
4.6
2.8
1
S1
2
1.8
1.6
1.4
1.2
1

Ratio Wall S1 / (Wall+ILT) S1

MODEL B13

Type A ILT (-)	Type B ILT (-)
25	1.25

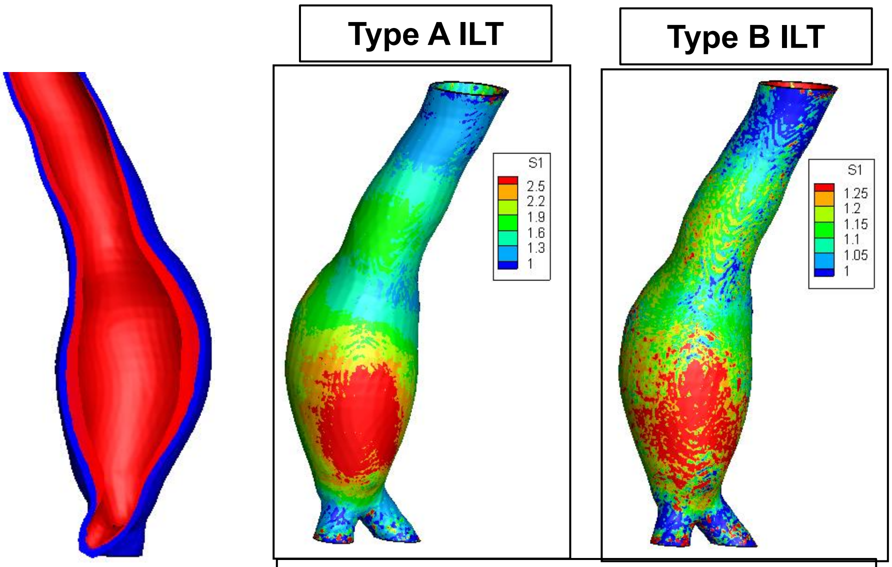
Type A ILT
Type B ILT
S1
2.5
2.2
1.9
1.6
1.3
1
S1
1.25
1.2
1.15
1.1
1.05
1

Ratio Wall S1 / (Wall+ILT) S1

MODEL B14

Type A ILT (-)	Type B ILT (-)
10	1.8

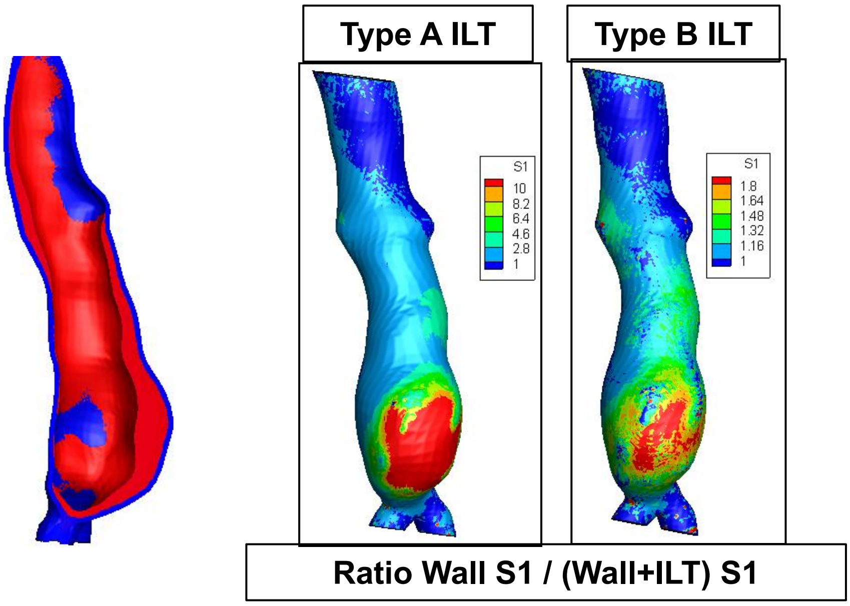
Type A ILT
Type B ILT
S1
10
8.2
6.4
4.6
2.8
1
S1
1.8
1.64
1.48
1.32
1.16
1
Ratio Wall S1 / (Wall+ILT) S1

MODEL B15

Type A ILT (-)	Type B ILT (-)
40	2

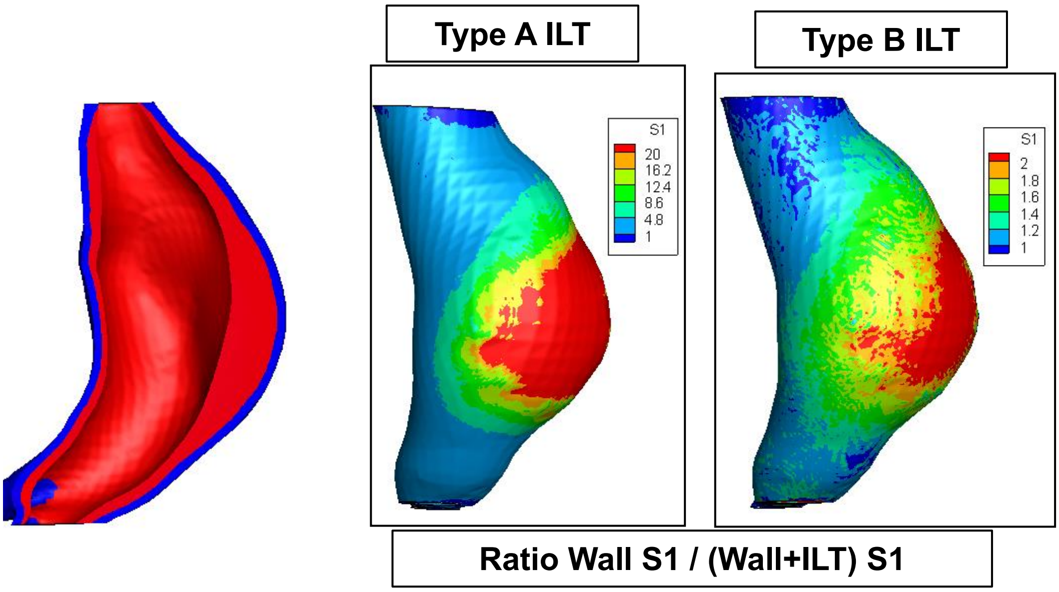
Type A ILT
Type B ILT
S1
20
16.2
12.4
8.6
4.8
1
S1
2
1.8
1.6
1.4
1.2
1
Ratio Wall S1 / (Wall+ILT) S1

MODEL B16	
Type A ILT (-)	Type B ILT (-)
2	1.2

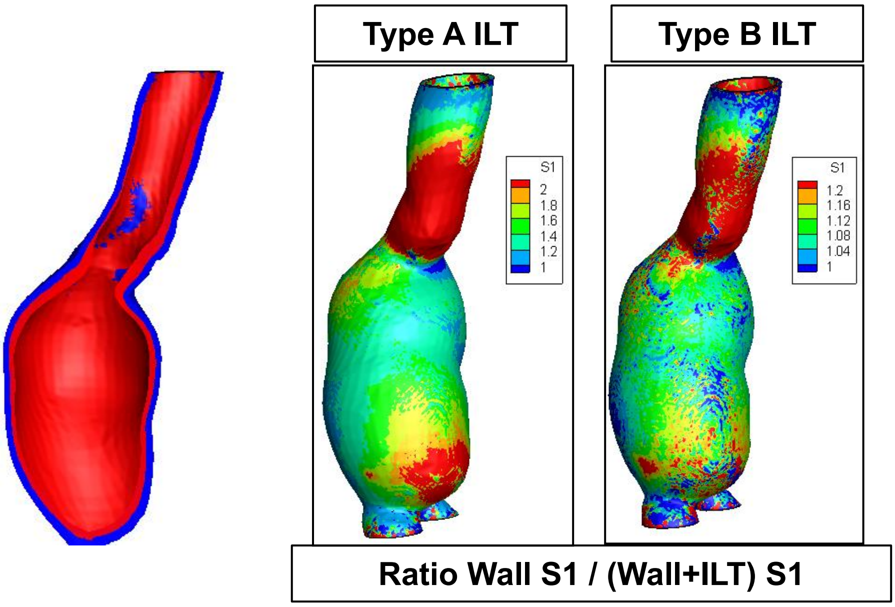
Type A ILT
Type B ILT
S1
2
1.8
1.6
1.4
1.2
1
S1
1.2
1.16
1.12
1.08
1.04
1
Ratio Wall S1 / (Wall+ILT) S1

MODEL B17	
Type A ILT (-)	Type B ILT (-)
9	1.65

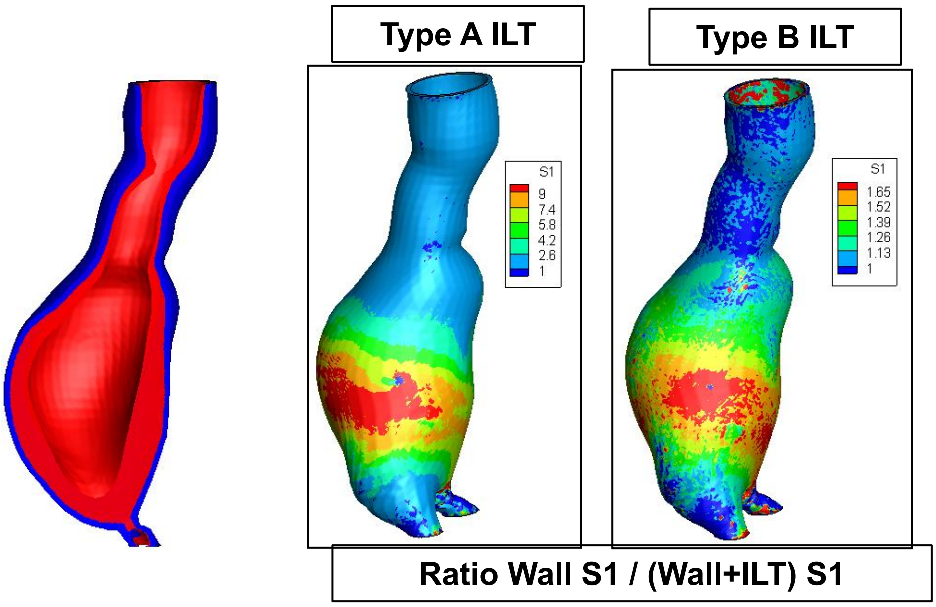
Type A ILT
Type B ILT
S1
9
7.4
5.8
4.2
2.6
1
S1
1.65
1.52
1.39
1.26
1.13
1
Ratio Wall S1 / (Wall+ILT) S1

MODEL B18

Type A ILT (-)	Type B ILT (-)
5	1.35

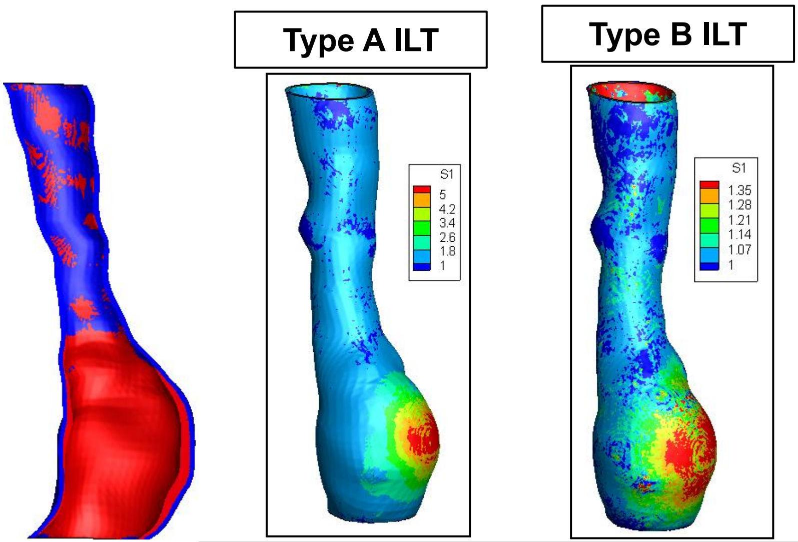
Type A ILT
Type B ILT
S1
5
4.2
3.4
2.6
1.8
1
S1
1.35
1.28
1.21
1.14
1.07
1

Ratio Wall S1 / (Wall+ILT) S1

MODEL B19

Type A ILT (-)	Type B ILT (-)
1.15	1.03

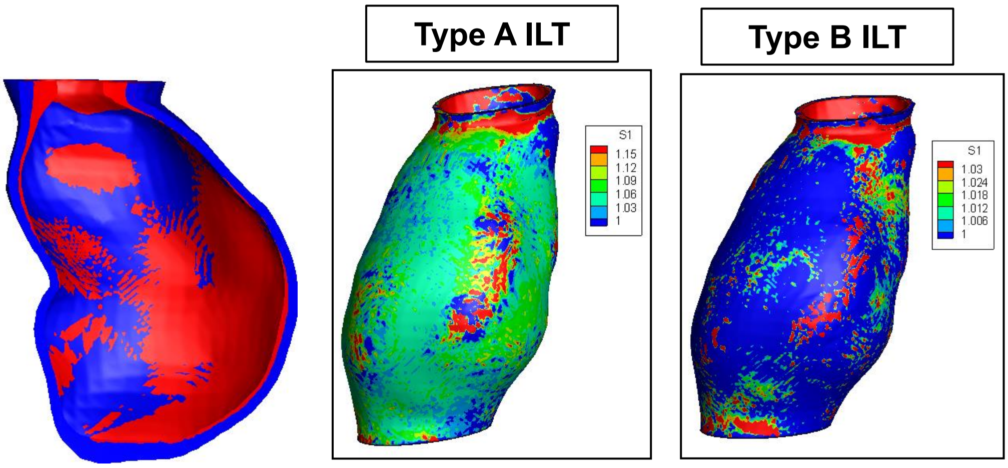
Type A ILT
Type B ILT
S1
1.15
1.12
1.09
1.06
1.03
1
S1
1.03
1.024
1.018
1.012
1.006
1

Ratio Wall S1 / (Wall+ILT) S1

MODEL B20	
Type A ILT (-)	Type B ILT (-)
1000	15

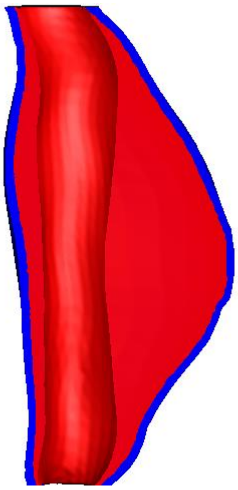

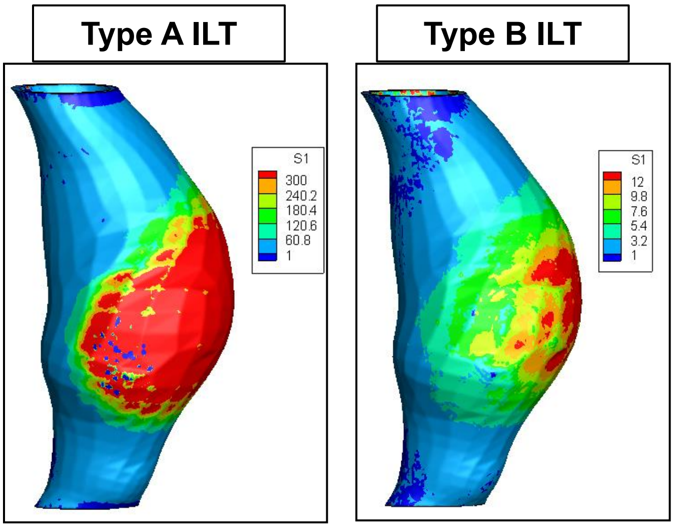
Type A ILT
Type B ILT
S1
300
240.2
180.4
120.6
60.8
1
S1
12
9.8
7.6
5.4
3.2
1

Ratio Wall S1 / (Wall+ILT) S1

MODEL B21	
Type A ILT (-)	Type B ILT (-)
120	3

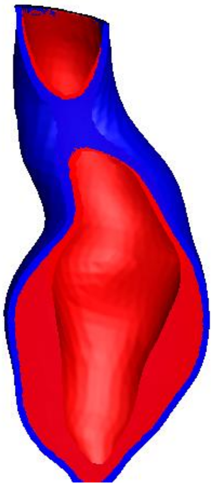

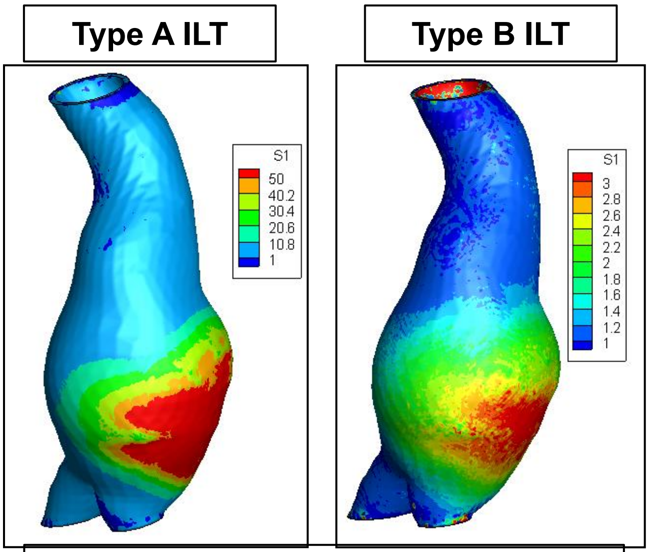
Type A ILT
Type B ILT
S1
50
40.2
30.4
20.6
10.8
1
S1
3
2.8
2.6
2.4
2.2
2
1.8
1.6
1.4
1.2
1

Ratio Wall S1 / (Wall+ILT) S1

APPENDIX C

10. APPENDIX C

This appendix presents the results for 7 models for which the ILT has been modeled as heterogeneous. ILT has been modeled using Type A (equation 7) material model and Type B (equation 8) material models, being Type A stiffer compared to Type B.

The ILT of the calculated models are shown in YELLOW for Type A ILT tissue and in BLUE for Type B ILT tissue.

MODEL B3

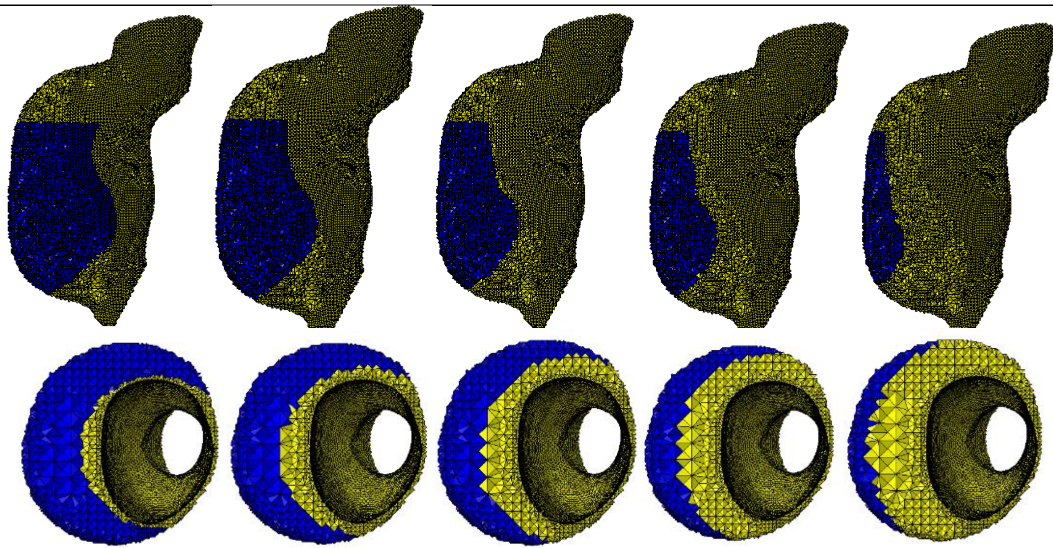

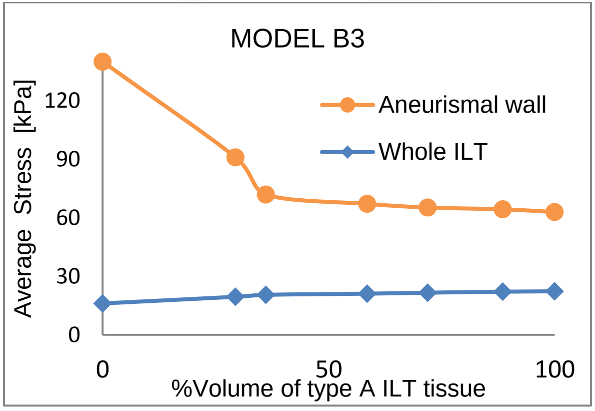

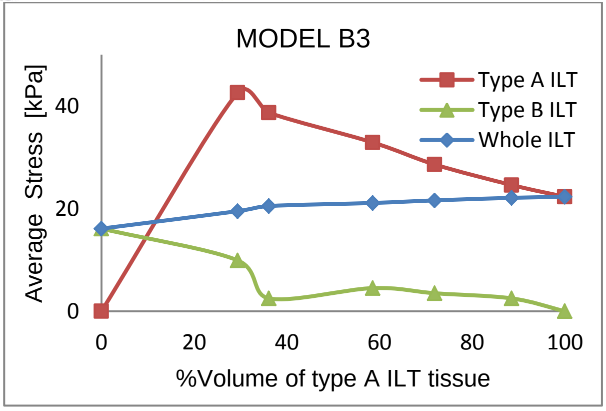

MODEL B6

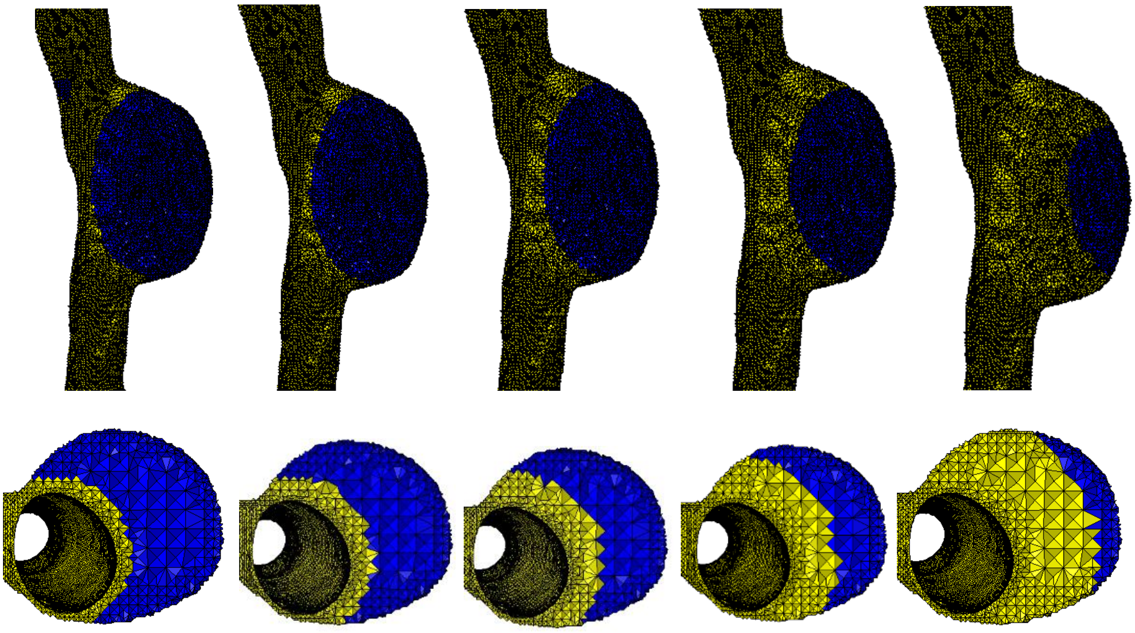

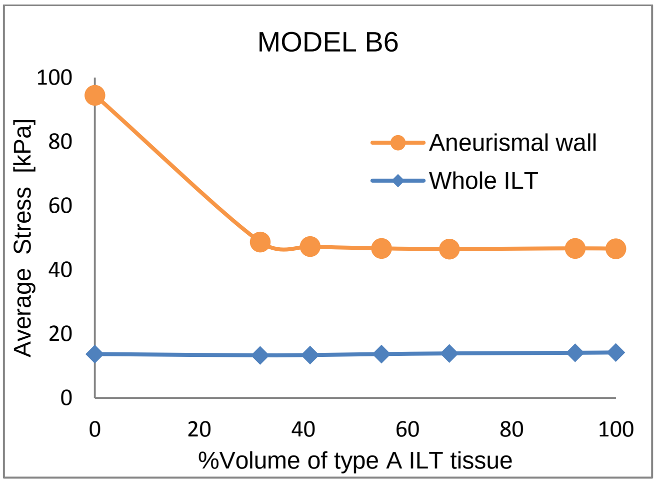
MODEL B6
Average Stress [kPa]
100
80
60
40
20
0
0
20
40
60
80
100
%Volume of type A ILT tissue
Aneurismal wall
Whole ILT

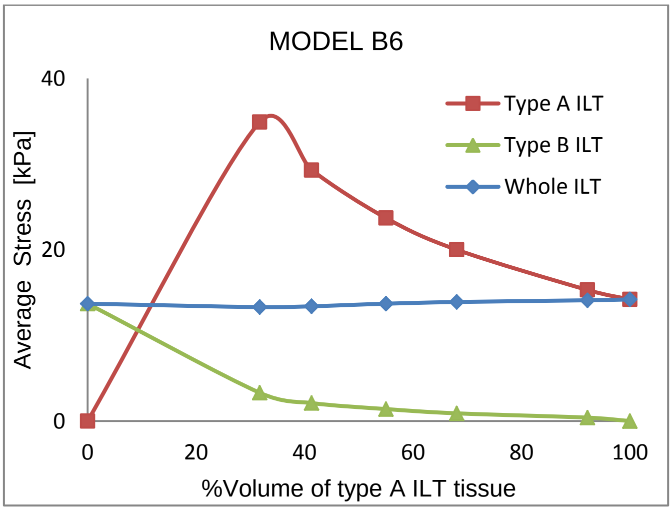
MODEL B6
Average Stress [kPa]
40
20
0
0
20
40
60
80
100
%Volume of type A ILT tissue
Type A ILT
Type B ILT
Whole ILT

MODEL B7

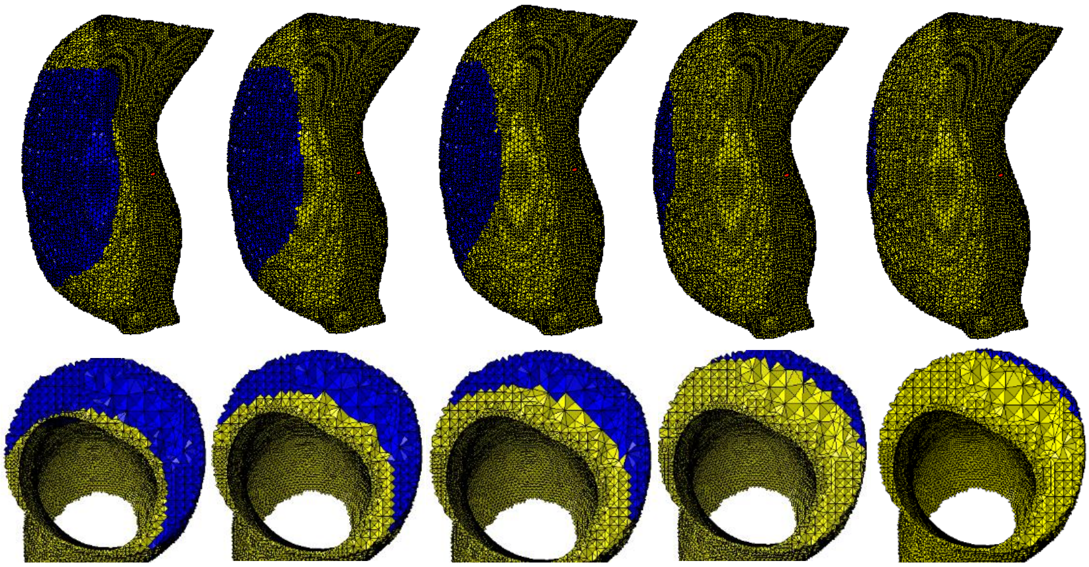

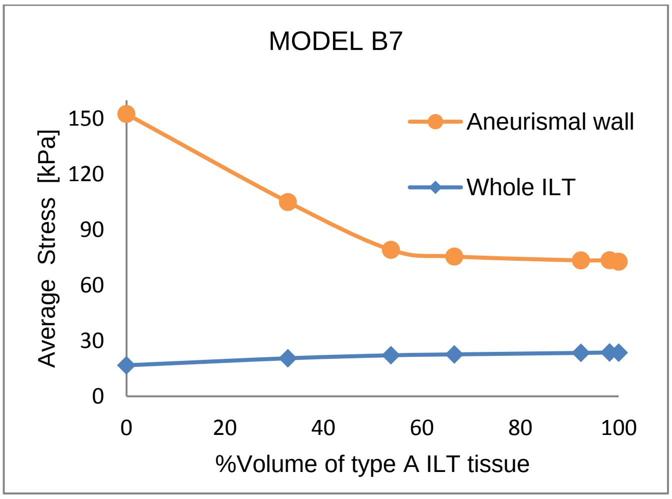
MODEL B7
Average Stress [kPa]
150
120
90
60
30
0
0
20
40
60
80
100
%Volume of type A ILT tissue
Aneurismal wall
Whole ILT

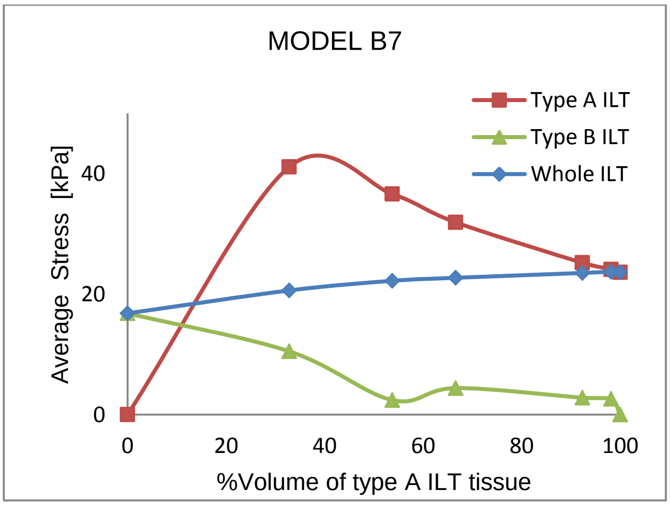
MODEL B7
Average Stress [kPa]
40
20
0
0
20
40
60
80
100
%Volume of type A ILT tissue
Type A ILT
Type B ILT
Whole ILT

MODEL B11

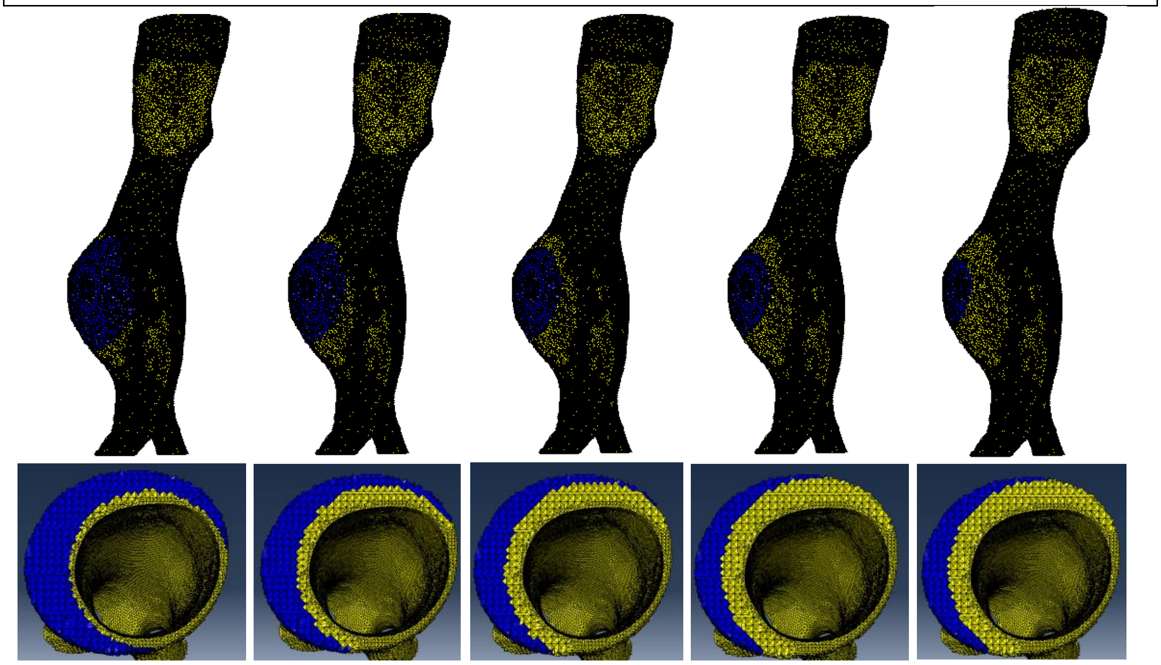

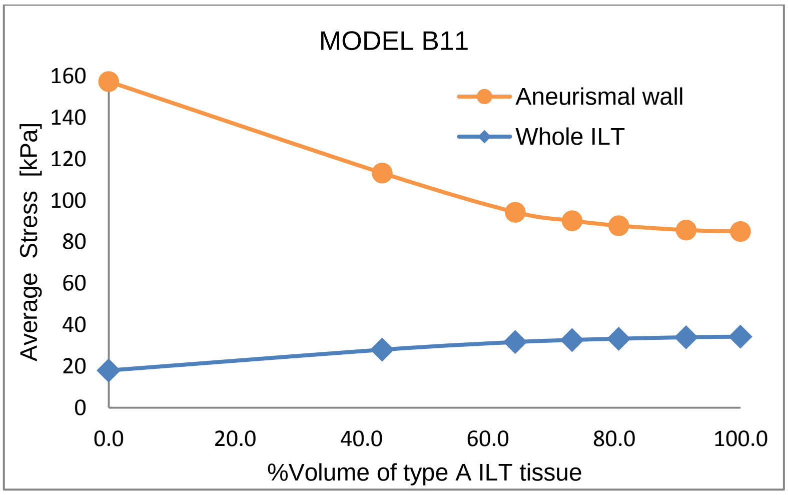
MODEL B11
Aneurismal wall
Whole ILT
Average Stress [kPa]
0
20
40
60
80
100
120
140
160
0.0
20.0
40.0
60.0
80.0
100.0
%Volume of type A ILT tissue

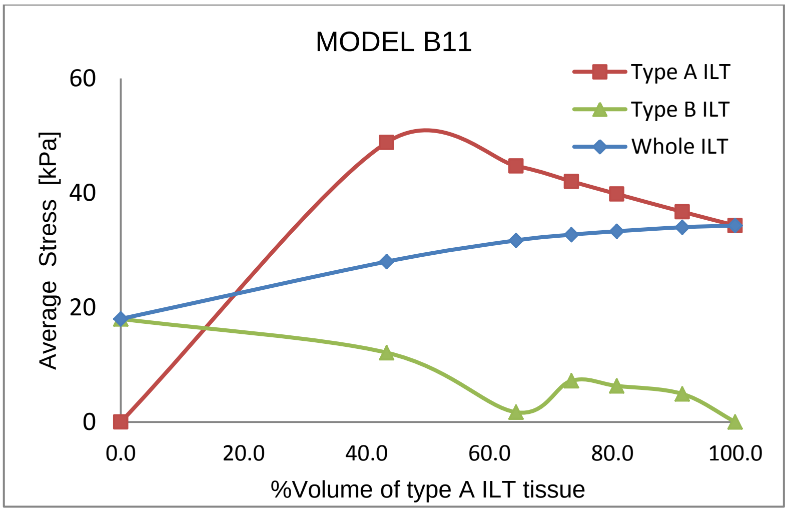
MODEL B11
Type A ILT
Type B ILT
Whole ILT
Average Stress [kPa]
0
20
40
60
0.0
20.0
40.0
60.0
80.0
100.0
%Volume of type A ILT tissue

MODEL B17

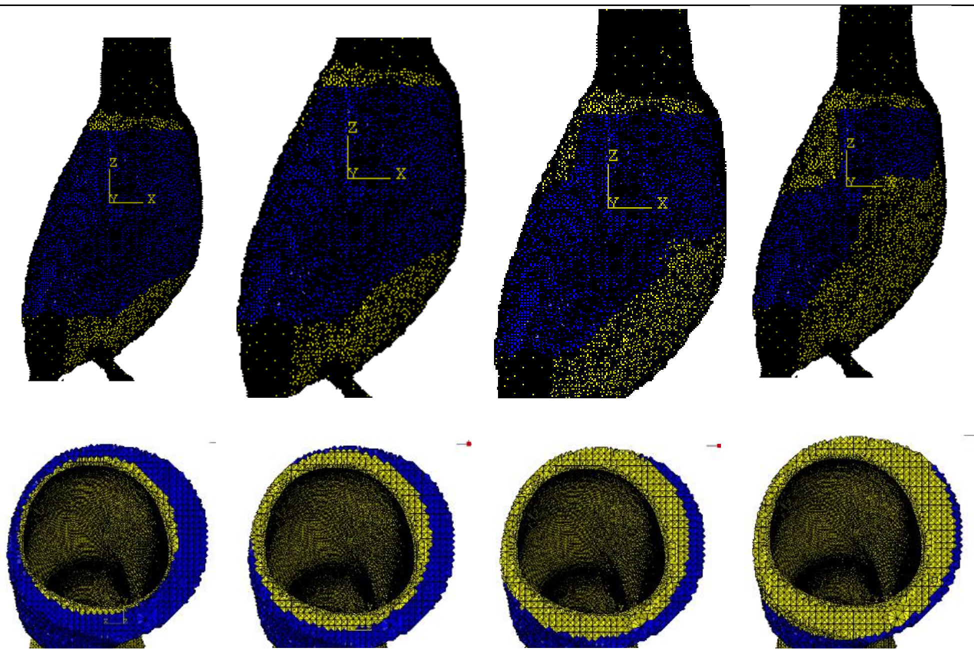
z
x
y

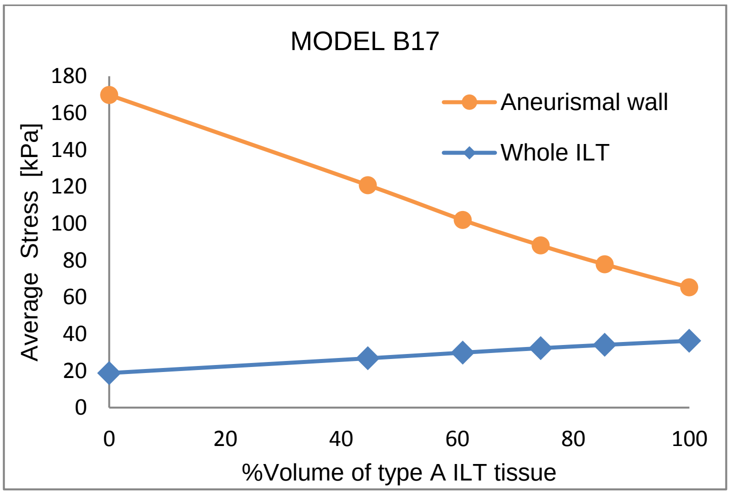
MODEL B17
Aneurismal wall
Whole ILT
Average Stress [kPa]
180
160
140
120
100
80
60
40
20
0
0
20
40
60
80
100
%Volume of type A ILT tissue

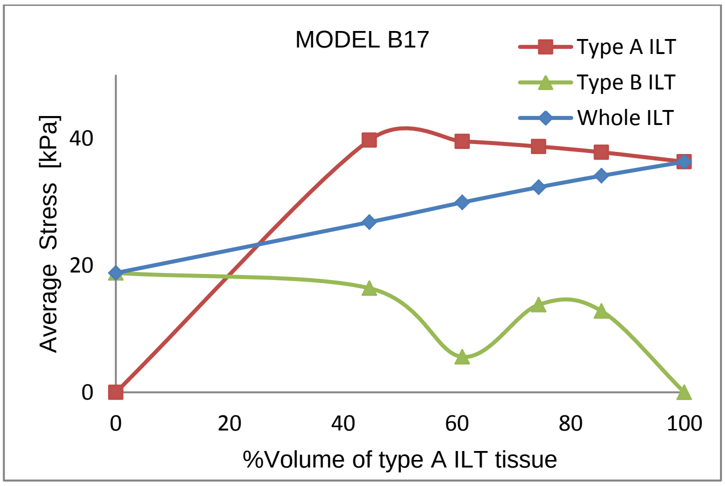
MODEL B17
Type A ILT
Type B ILT
Whole ILT
Average Stress [kPa]
40
20
0
0
20
40
60
80
100
%Volume of type A ILT tissue

MODEL B20

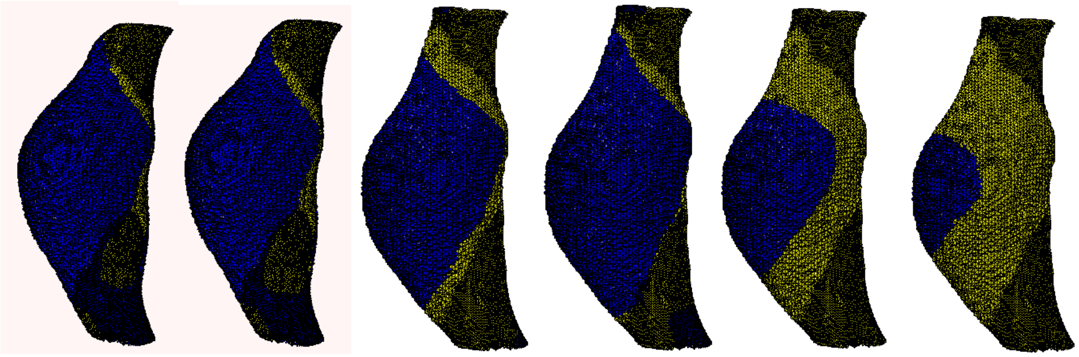

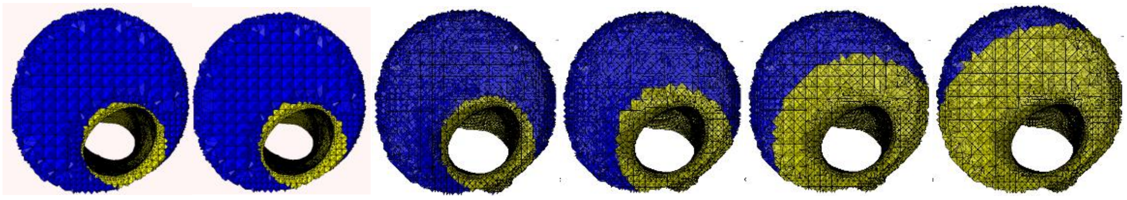

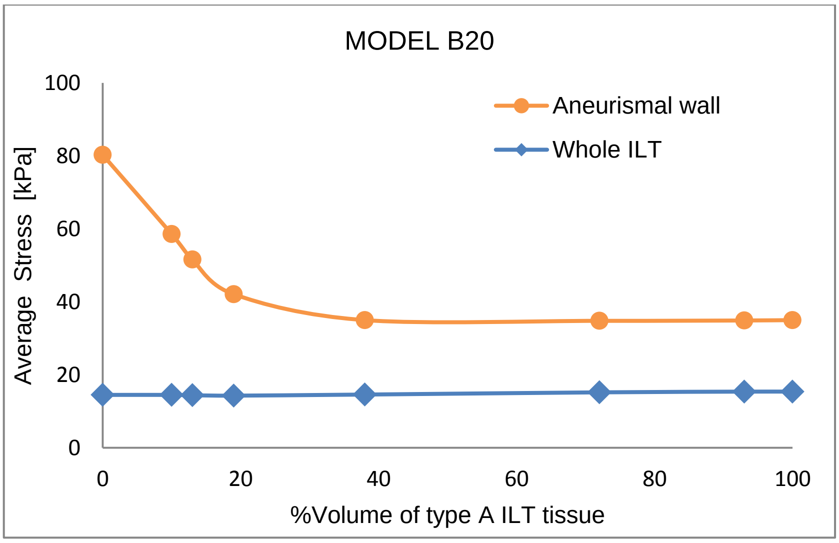
MODEL B20
Aneurismal wall
Whole ILT
Average Stress [kPa]
0
20
40
60
80
100
0
20
40
60
80
100
%Volume of type A ILT tissue

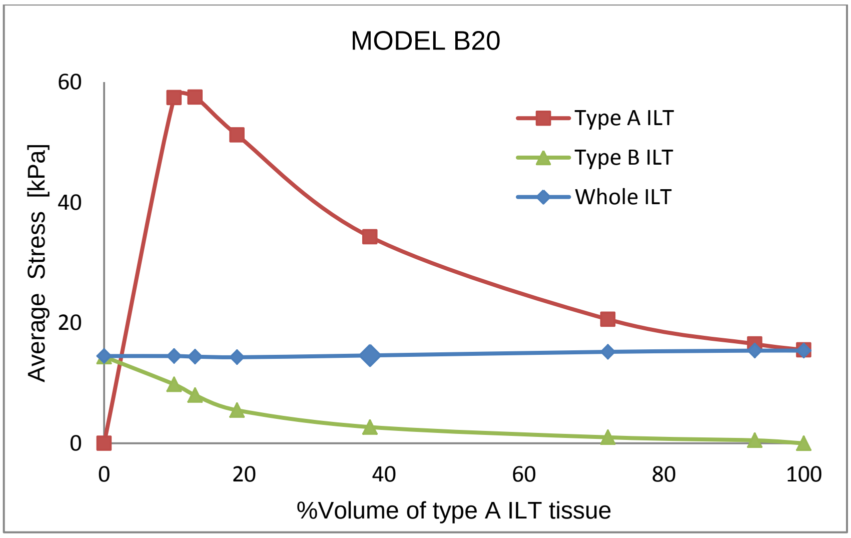
MODEL B20
Type A ILT
Type B ILT
Whole ILT
Average Stress [kPa]
0
20
40
60
0
20
40
60
80
100
%Volume of type A ILT tissue

MODEL B20

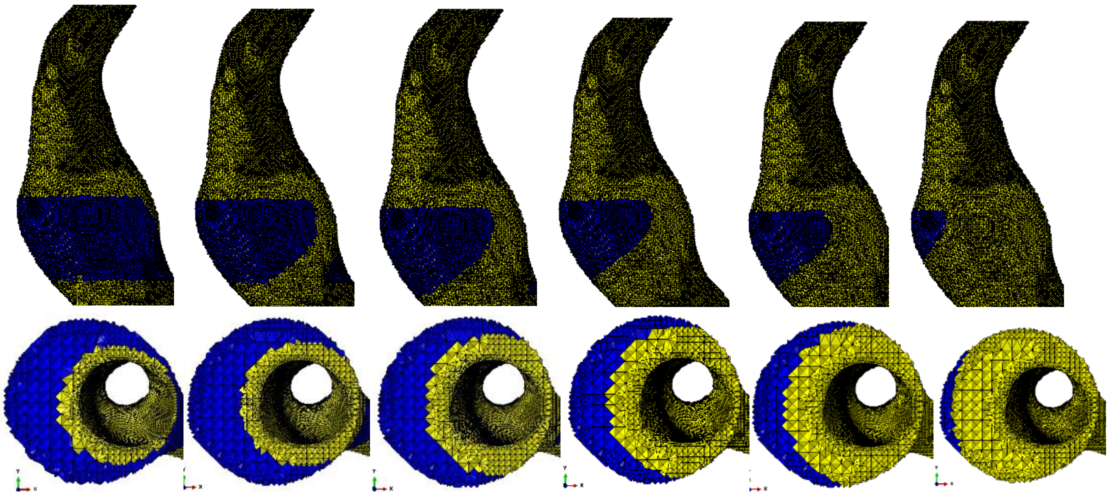

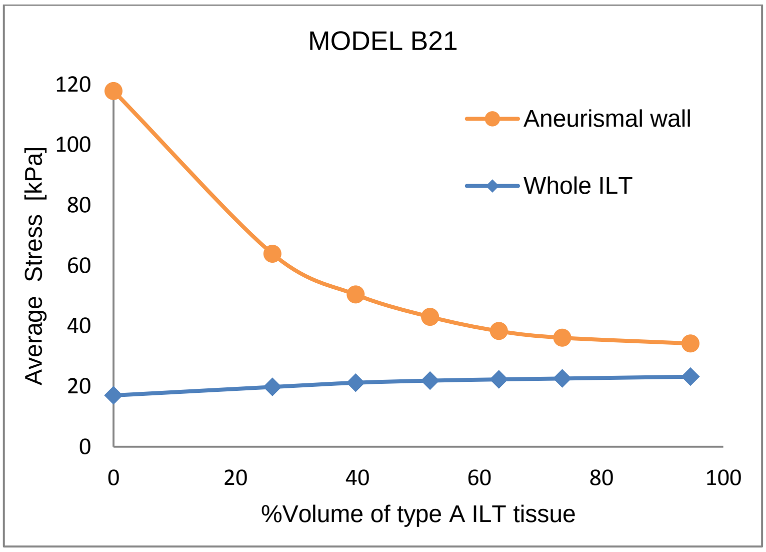
MODEL B21
Average Stress [kPa]
120
100
80
60
40
20
0
0
20
40
60
80
100
%Volume of type A ILT tissue
Aneurismal wall
Whole ILT

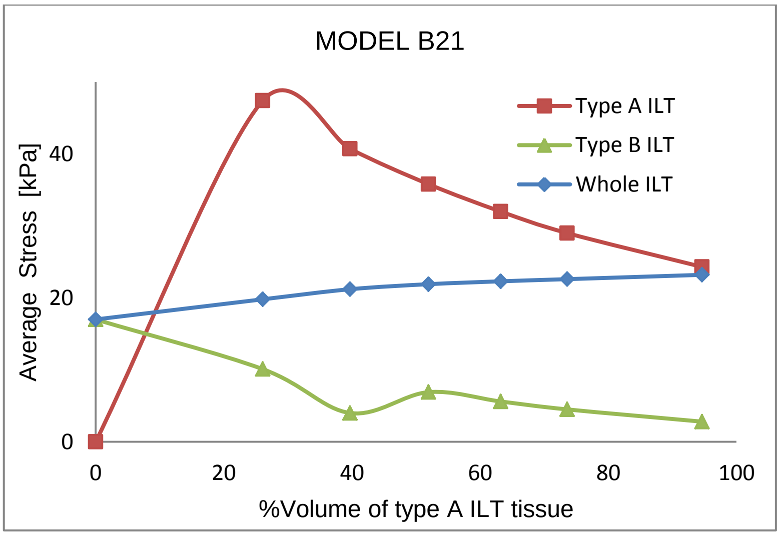
MODEL B21
Average Stress [kPa]
40
20
0
0
20
40
60
80
100
%Volume of type A ILT tissue
Type A ILT
Type B ILT
Whole ILT

APPENDIX D

ARAVGVSTANAE ✝ ST
S

11. APPENDIX D

This appendix presents the material user subroutine UHYPER implemented in ABAQUS for the hyperelastic isotropic material model of Equation 5:

$$W_{wall}^{iso} = \kappa(J-1)^2 + D_1\left(e^{D_2(\bar{I}_1-3)} - 1\right)$$

```
      SUBROUTINE UHYPER(BI1,BI2,AJ,U,UI1,UI2,UI3,TEMP,NOEL,
     1 CMNAME,INCMPFLAG,NUMSTATEV,STATEV,NUMFIELDV,FIELDV,
     2 FIELDVINC,NUMPROPS,PROPS)
C
      INCLUDE 'ABA_PARAM.INC'
C
      CHARACTER*80 CMNAME
      DIMENSION UI1(3),UI2(6),UI3(6),STATEV(*),FIELDV(*),
     2 FIELDVINC(*),PROPS(*)
C
      PARAMETER (ZERO=0.0D0,ONE=1.0D0, TWO=2.0D0, THREE=3.0D0)
C
      D1=PROPS(1)
      D2=PROPS(2)
      KAPPA=PROPS(3)
C
C
      U=D1*(exp(D2*(BI1-THREE))-ONE)+KAPPA*(AJ-ONE)**2
      UI1(1)=D1*D2*exp(D2*(BI1-THREE))
      UI1(2)=ZERO
      UI1(3)=TWO*KAPPA*(AJ-ONE)
      UI2(1)=D1*(D2**2)*exp(D2*(BI1-THREE))
      UI2(2)=ZERO
      UI2(3)=TWO*KAPPA
      UI2(4)=ZERO
      UI2(5)=ZERO
      UI2(6)=ZERO
      UI3(1)=ZERO
      UI3(2)=ZERO
      UI3(3)=ZERO
      UI3(4)=ZERO
      UI3(5)=ZERO
      UI3(6)=ZERO
      RETURN
      END
C
C      *******************************************
C
      SUBROUTINE  URDFIL(LSTOP,LOVRWRT,KSTEP,KINC,DTIME,TIME)
C
       INCLUDE 'aba_param.inc'
C
       DIMENSION TIME(2)
       DIMENSION ARRAY(513),JRRAY(NPRECD,513)
       EQUIVALENCE (ARRAY(1),JRRAY(1,1))
       CHARACTER(256) JOBDIR, JOBNAME
       CHARACTER(256) FILENAME1
       DIMENSION DATOS(4)
C
C FIND CURRENT INCREMENT.
C
        CALL GETOUTDIR(JOBDIR,LENJOBDIR)
        CALL GETJOBNAME(JOBNAME,LJOBNAME)
        FILENAME1=JOBDIR(:LENJOBDIR)//'/'//JOBNAME(:LJOBNAME)//'_U.dat'
        open(9,file=FILENAME1,position='append')
        CALL POSFIL(KSTEP,KINC,ARRAY,JRCD)
        DO K1=1,999999
         CALL DBFILE(0,ARRAY,JRCD)
         IF (JRCD .NE. 0) GO TO 110
         KEY=JRRAY(1,2)
C
         IF (TIME(2).GT.0.99) THEN
            if (KEY.EQ.107) then
C             The node number is extracted:
```

```
               DATOS(1)=JRRAY(3,2)
               DATOS(2) = ARRAY(4) ! ux
               DATOS(3) = ARRAY(5) ! uy
               DATOS(4) = ARRAY(6) ! uz
               write(9,211) DATOS(1),DATOS(2),DATOS(3), DATOS(4)
 211           FORMAT(F8.1,1X,F15.6,2X,F15.6,2X,F15.6)
             end if
          END IF
        END DO
 110    CONTINUE
C
        close(9)
C
C
       LOVRWRT=1
C
      RETURN
      END
```

APPENDIX E

12. APPENDIX E

This appendix presents the material user subroutine UANISOHYPER_INV implemented in ABAQUS for the hyperelastic anisotropic material model of Equation 6:

$$\begin{aligned} W_{wall}^{aniso} \quad = \quad & \kappa(\mathrm{J}-1)^2 + D_1\left(e^{D_2(\bar{I}_1-3)}-1\right) \\ & + \frac{k_1}{k_2}\left(e^{k_2(\bar{I}_4-1)^2}-1\right) \end{aligned}$$

```
C     SUBRUTINE FOR ANISOTROPIC HYPERELASTIC MATERIAL
      SUBROUTINE UANISOHYPER_INV (AINV, UA, ZETA, NFIBERS, NINV,
     1     UI1, UI2, UI3, TEMP, NOEL, CMNAME, INCMPFLAG, IHYBFLAG,
     2     NUMSTATEV, STATEV, NUMFIELDV, FIELDV, FIELDVINC,
     3     NUMPROPS, PROPS)
C
              INCLUDE 'ABA_PARAM.INC'
C
      CHARACTER*80 CMNAME
      DIMENSION AINV(NINV), UA(2),
     2     ZETA(NFIBERS*(NFIBERS-1)/2), UI1(NINV),
     3     UI2(NINV*(NINV+1)/2), UI3(NINV*(NINV+1)/2),
     4     STATEV(NUMSTATEV), FIELDV(NUMFIELDV),
     5     FIELDVINC(NUMFIELDV), PROPS(NUMPROPS)
C
C
      PARAMETER (ZERO=0.0D0,ONE=1.0D0, TWO=2.0D0, THREE=3.0D0)
C
      D1=PROPS(1)
      D2=PROPS(2)
      KAPPA=PROPS(3)
      K_1=PROPS(4)
      K_2=PROPS(5)
      I4_0=PROPS(6)
C
C     - I1
      BI1 = aInv(1)
      term_1 = BI1-THREE
C
C     - I3 (=J)
      AJ = aInv(3)
C
C     - I4(11)
      BI4 = aInv(4)
      term_4 = BI4-I4_0
C
      EXP_1=exp(D2*term_1)
      EXP_2=exp(K_2*term_4**2)
```

```
C
C      SE INICIALIZAN A CERO LOS TERMINOS
      UI1=0.0D0
      UI2=0.0D0
      UI3=0.0D0
C     ************************************
C      Strain Energy Density Function
      UA(1)=D1*(EXP_1-ONE)+ (K_1/K_2)*(EXP_2-1) + KAPPA*(AJ-ONE)**2
C
C     *********************************
C           DERIVADAS PRIMERAS
      UI1(1)=D1*D2*EXP_1
      UI1(3)=TWO*KAPPA*(AJ-ONE)
      UI1(4)=2*K_1*term_4*EXP_2
C
C      ********************************
C     DERIVADAS SEGUNDAS
C       d^2U/dI3^2
      UI2(1)=D1*(D2**2)*EXP_1
C       d^2U/dI3^2
      UI2(6)=TWO*KAPPA
C       d^2U/dI4^2
      UI2(10)=2*K_1*EXP_2*(1 + 2*K_2*term_4**2)
C
C
      RETURN
      END
C
C
C     ********************************************
C
      SUBROUTINE  URDFIL(LSTOP,LOVRWRT,KSTEP,KINC,DTIME,TIME)
C
       INCLUDE 'aba_param.inc'
C
       DIMENSION TIME(2)
       DIMENSION ARRAY(513),JRRAY(NPRECD,513)
       EQUIVALENCE (ARRAY(1),JRRAY(1,1))
       CHARACTER(256) JOBDIR, JOBNAME
       CHARACTER(256) FILENAME1
       DIMENSION DATOS(4)
C
C FIND CURRENT INCREMENT.
C
        CALL GETOUTDIR(JOBDIR,LENJOBDIR)
        CALL GETJOBNAME(JOBNAME,LJOBNAME)
        FILENAME1=JOBDIR(:LENJOBDIR)//'/'//JOBNAME(:LJOBNAME)//'_U.dat'
        open(9,file=FILENAME1,position='append')
        CALL POSFIL(KSTEP,KINC,ARRAY,JRCD)
        DO K1=1,999999
         CALL DBFILE(0,ARRAY,JRCD)
         IF (JRCD .NE. 0) GO TO 110
         KEY=JRRAY(1,2)
C
         IF (TIME(2).GT.0.99) THEN
            if (KEY.EQ.107) then
C             SE EXTRAE EXTRAE EL NUMERO DE NODO
              DATOS(1)=JRRAY(3,2)
              DATOS(2) = ARRAY(4) ! ux
              DATOS(3) = ARRAY(5) ! uy
              DATOS(4) = ARRAY(6) ! uz
             write(9,211) DATOS(1),DATOS(2),DATOS(3), DATOS(4)
 211         FORMAT(F8.1,1X,F15.6,2X,F15.6,2X,F15.6)
            end if
          END IF
        END DO
 110    CONTINUE
C
        close(9)
C
C
       LOVRWRT=1
C
      RETURN
      END
```

REFERENCES

13. REFERENCES

Abisi, S. et al., 2007. Cysteine protease activity in the wall of abdominal aortic aneurysms. *J Vasc Surg*, pp.46(6), pp. 1260-1266.

Ailawadi, G., Eliason, J.L. & Upchurch, G.R., 2003. Current concepts in the pathogenesis of abdominal aortic aneurysm. *Journal of vascular surgery : official publication, the Society for Vascular Surgery [and] International Society for Cardiovascular Surgery, North American Chapter*, pp.38(3), pp. 584-588.

Alastrué, V.A. et al., 2006. Numerical framework for patient-specific computational modelling of vascular tissue. *Commun. Numer. Meth. En.*, pp.6:1-30.

Ashton, H. et al., Nov 2002. Multicentre Aneurysm Screening Study Group. The Multicentre Aneurysm Screening Study (MASS) into the effect of abdominal aortic aneurysm screening on mortality in men: a randomised controlled trial. *The Lancet*, pp.Vol. 360, No. 9345, pp1531-9.

Ayyalasomayajula, A., Vande Geest, J.P. & Simon, B.R., 2010. Porohyperelastic Finite Element Modeling of Abdominal Aortic Aneurysms. *J. Biomech. Eng.*, pp.132:104502–104502.

Baek , S., Gleason, R.L., Rajagopal, K.R. & Humphrey, J.D., 2007. Theory of small on large: potential utility in computations of fluid-solid interactions in arteries. *Computer methods in Applied Mechanichs and Engineering*, pp.196-pp 3070-3089.

Baumgartner, I. et al., 2008. Cardiovascular risk profile and outcome of patients with abdominal aortic aneurysm in out-patients with atherothrombosis: Data from the Reduction of Atherothrombosis for Continued Health (REACH) Registry. *Journal of Vascular Surgery*, pp.48(4), pp. 808-814.

Bjorck, H.M. et al., 2009. Association of genetic variation on chromosome 9p21.3 and arterial stiffness. *Journal of internal medicine,* pp.265(3), pp. 373-381.

Brady, A.R. et al., 2004. Abdominal aortic aneurysm expansion: risk factors and time intervals for surveillance. *Circulation*, pp.110(1), pp. 16-21.

Brown, L.C. & Powell, J.L., 1999. Risk factors for aneurysm rupture in patients kept under ultrasound surveillance. UK small aneurysm trial participants. *Ann. Surg.*, pp.230(3):289-296 discussion 296-297.

Carlson, D.E., 1969. Inverse Deformation Results for Elastic Materials. *Z. Angew. Math. Phys.*, pp.20(2):261:263.

Chadwick, P., 1975. Application of an energy-momentum tensor in elastostatics. *J. Elasticity*, pp.5:249-258.

Chandra, S. et al., 2013. Fluid-structure interaction modeling of abdominal aortic aneurysms: the impact of patient specific inflow conditions and fluid/solid coupling. *Journal of biomechanical engineering, submitted.*.

Chandra, S. et al., June 26-29 2013. EXPERIMENTAL VALIDATION OF A COMPUTATIONAL ALGORITHM FOR THE ZERO PRESSURE GEOMETRY DERIVATION OF BLOOD VESSELS. *Proceedings of the ASME 2013 Summer Bioengineering Conference*.

Chen, Y.J., Chen, S.Y., Wang, J.T. & Hsueh, P.R., 2009. Mycotic aneurysm caused by gas-forming serotype K5 Klebsiella pneumoniae. *Int J Infect Dis*, pp.13(2), pp. e47-48.

Choke, E. et al., 2005. A review of biological factors implicated in abdominal aortic aneurysm rupture. *European Journal of Vascular and Endovascular Surgery*, pp.30(3), pp. 227-244.

Cronenwett , J.W., Krupski, W. & Rutherford, R., 5fh ed. ed. 2000. *Abdominal aortic and iliac aneurysms in vascular surgery*. Philadelphia: WB Saunders.

Darling, R.C., Messina, C.R., Brewster, D.C. & Ottinger, L.W., 1977. Autopsy Study of Unoperated Abdominal Aortic-Aneurysms - Case for Early Resection. *Circulation*, pp.56(3), pp. 161-164.

De Putter, S.B. et al., 2006. Patient-specific initial wall stress in abdominal aortic aneurysms with a backward incremental method. *J Biomech.*, pp.40:1081–1090.

Demiray, H., 1972. A note on the elasticity of soft biological tissues. *J. Biomech.*, pp.5:309–311.

Di Achielle, P., Celi, S., Di Puccio, F. & Forte, P., 2011. Anisotropic AAA: Computational comparison between four and two fiber family materials models. *Journal of Biomechanics*, pp.44- pp2418-2426.

Di Martino, E.S. et al., 2001. Fluid-structure interaction within realistic three-dimensional models of the aneurysmatic aorta as a guidance to assess the risk of rupture of the aneurysm. *Med Eng Phys*, pp.23(9), pp. 647-655.

Di Martino, E.S. et al., 1998. Biomechanics of abdominal aortic aneurysm in the presence of endoluminal thrombus: experimental characterisation and structural static computational analysis. *Eur. J. Vasc. Endovasc. Surg. Off. J. Eur. Soc. Vasc. Surg.*, pp.15:290–299.

Di Martino, E.S. & Vorp, D.A., 2003. Effect of variation in intraluminal thrombus constitutive properties on abdominal aortic aneurysm wall stress. *Ann. Biomed. Eng.*, pp.31 (7):804-809.

Dia, J. et al., 2009. Effect of blocking platelet activation with AZD6140 on development of abdominal aortic aneurysm in a rat aneurysmal model. *J Vasc Surg*, pp.49(3), pp. 719-727.

DiMartino, E.S. et al., 2006. Biomechanical properties of ruptured versus electively repaired abdominal aortic aneurysm wall tissue. *Journal of Vascular Surgery*, pp.43:570–576.

Dobrin, P.B., 1989. Pathophysiology and pathogenesis of aortic aneurysms. Current concepts. *The Surgical clinics of North America*, pp.69(4), pp. 687-703.

Dobrin, P.B. & Mrkvicka, R., 1994. Failure of elastin or collagen as possible critical connective tissue alterations underlying aneurysmal dilatation. *Cardiovasc Surg*, pp.2(4), pp. 484-488.

Doyle, B.J. et al., 2009. Vessel asymmetry as an additional diagnostic tool in the assessment of abdominal aortic aneurysms. *J Vasc Surg*, pp.49(2), pp. 443-454.

Doyle, B., Callanan, A. & McGloughlin, T., 2007. A comparison of modelling techniques for computing wall stress in abdominal aortic aneurysms. *Biomed. Eng. OnLine*, pp.6:38.

Doyle, B.J., Molony, D.S., Walsh, M.T. & McGloughlin, T.M., 2010. *Abdominal Aortic Aneurysms: New Approaches to Rupture Risk Assessment*. New York: Nova Science Publishers.

Elger, D.F., Blackketter, D.M., Budwig, R.S. & Johansen, K.H., 1996. The influence of shape on the stresses in model abdominal aortic aneurysms. *J Biomech Eng*, pp.118(3), pp. 326-332.

Elmore, J.R. et al., 2009. Identification of a genetic variant associated with abdominal aortic aneurysms on chromosome 3p12.3 by genome wide association. *J Vasc Surg*, pp.49(6), pp. 1525-1531.

Eskandari, M.K. et al., 2005. Enhanced abdominal aortic aneurysm in TIMP-1-deficient mice. *Journal of Surgical Research*, pp.123(2), pp. 289-293.

Fillinger , M.F. et al., 2004. Anatomic characteristics of ruptured abdominal aortic aneurysm on conventional CT scans: Implications for rupture risk. *J Vasc Surg*, pp.39(6), pp. 1243-1252.

Fillinger, M.F., Marra, S.P., Raghavan, M.L. & Kennedy, F.E., 2003. Prediction of rupture risk in abdominal aortic aneurysm during observation: Wall stress versus diameter. *J. Vasc. Surg. 37(4*, pp.pp.724-732.

Fillinger, M.F. et al., 2002. In vivo analysis of mechanical wall stress and abdominal aortic aneurysm rupture risk. *J. Vasc. Surg*, pp.36(3):589-597.

Finol, E.A. & Scotti, C.M., 2007. Compliant biomechanics of abdominal aortic aneurysms: A fluid-structure interaction study. *Comput Struct*, pp.85(11-14), pp. 1097-1113.

Finol, E.A., Scotti, C.M., Jimenez, J. & Muluk, S.C., 2008. Wall stress and flow dynamics in abdominal aortic aneurysms: finite element analysis vs. fluid-structure interaction. *Computer methods in biomechanics and biomedical engineering*, pp.11(3), pp. 301-322.

Fontaine , V. et al., 2002. Involvement of the mural thrombus as a site of protease release and activation in human aortic aneurysms. *The American journal of pathology*, pp.161(5), pp. 1701-1710.

Freestone, T. et al., 1995. Inflammation and matrix metalloproteinases in the enlarging abdominal aortic aneurysm. *Arteriosclerosis, thrombosis, and vascular biology*, pp.15(8), pp. 1145-1151.

Gasser, T.C., 2011. An irreversible constitutive model for fibrous soft biological tissue: A 3-D microfiber approach with demonstrative application to abdominal aortic aneurysms. *Acta Biomaterialia*, pp.7-pp2457-2466.

Gasser, T.C., 2012. Bringing vascular biomechanics into clinical practice. Simulation-based decisions for elective abdominal aortic aneurysms repair. in B. Calvo and E. Pena (edts). Patient-Specific Computational Modeling (Lecture Notes in Computational Vision and Biomech)i. *Springer Science and Busines Media Dodrecht.*.

Gasser, T.C. et al., 2010. Biomechanical rupture risk assessment of abdominal aortic aneurysms: Model complexity versus predictability of finite element simulations. *Eur. J. Vasc. Endovasc.*, pp.40: 176-185.

Gasser, T.C. et al., 2012. Spatial orientation of collagen fibers in the Abdominal Aortic Aneurysm's wall and its relation to wall mechanics. *Acta Biomaterialia*, pp.8(8): 3091-3103.

Gasser, T.C., Görgülü, G., Folkesson, M. & Swedenborg, J., 2008. Failure properties of intraluminal thrombus in abdominal aortic aneurysm under static and pulsating mechanical loads. *J. Vasc. Surg.*, pp.48:179–188.

Georgakarakos, E. et al., 2010a. The role of geometric parameters in the prediction of abdominal aortic aneurysm wall stress. *Eur J Vasc Endovasc Surg*, pp.39(1), pp. 42-48.

Georgakarakos, E. et al., 2010b. Peak wall stress does not necessarily predict the location of rupture in abdominal aortic aneurysms. *Eur. J. Vasc. Endovasc. Surg. Off.*, pp.39:302–304.

Georgakarakos, E. et al., 2009. The influence of intraluminal thrombus on abdominal aortic aneurysm wall stress. *Int. Angiol.*, pp.28:325–333.

Giannoglou, G. et al., 2006. Predicting the risk of rupture of abdominal aortic aneurysms by utilizing various geometrical parameters: revisiting the diameter criterion. *Angiology*, pp.57(4), pp. 487-494.

Govindjee, S. & Mihalic, P., 1996. Computational methods for inverse finite elastostatics. *Comput. Method Appl. M.*, pp.136:47-57.

Govindjee, S. & P.M., 1998. Computational methods for inverse deformations in quasi-incompressible finite elasticity. *Int. J. Numer. Meth. Eng*, pp.43:821-838.

Hans, S.S., Jareunpoon, O., Balasubramaniam, B. & Zelenock., G.B., 2005. Size and location of thrombus in intact and ruptured abdominal aortic aneurysms. *J. Vasc. Surg.*, pp.41: 584-588.

Harter, L.P., Gross, B.H., Callen, P.W. & Barth, R.A., 1982. Ultrasonic evaluation of abdominal aortic thrombus. *J. Ultrasound Med.*, pp.1:315–318.

Heng, M.S. et al., 2008. Peak wall stress measurement in elective and acute abdominal aortic aneurysms. *J. Vasc. Surg.*, pp.47: 17-22.

He, C.M. & Roach, M.R., 1994. The composition and mechanical properties of abdominal aortic aneurysms. *Journal of Vascular Surgery*, pp.20-pp6-13.

Hinnen, J.W., Koning, O.H.J., Visser, M.J.T. & Van Bockel, H.J., 2005. Effect of intraluminal thrombus on pressure transmission in the abdominal aortic aneurysm. *J. Vasc. Surg.*, pp.42:1176–1182.

Holzapfel, G.A., 2000. Nonlinear Solid Mechanics. A Continuum Approach for Engineering. *Chichester: John Wiley & Sons Ltd*, p.455 pp.

Holzapfel, G.A., Gasser, T.C. & Ogden, R.W., 2000. A new consitutive framework for arterial wall mechanics and a comparative study of material models. *Computational biomechanichs*, p.paper No 8.

Huber, T.S. et al., 2001. Experience in the United States with intact abdominal aortic aneurysm repair. *Journal of Vascular Surgery*, pp.33(2): p. 304-10; discussion 310-1.

Inzoli, F. et al., 1993. Biomechanical factors in abdominal aortic aneurysm rupture. *Eur. J. Vasc. Surg.*, pp.7:667–674.

Karkos, C. et al., 2000. Abdominal aortic aneurysm: the role of clinical examination and opportunistic detection. *Eur. J. Vasc. Endovasc. Surg.*, pp.19:299-303.

Kazi, M. et al., 2003. Influence of intraluminal thrombus on structural and cellular composition of abdominal aortic aneurysm wall. *J Vasc Surg*, pp.38(6), pp. 1283-1292.

Khanafer, K.M., Bull , J.L. & Berguer, R., 2009. Fluid-structure interaction of turbulent pulsatile flow within a flexible wall axisymmetric aortic aneurysm model. *Eur J Mech B-Fluid*, pp.28(1), pp. 88-102.

Kim, Y.H. et al., 2008. Hemodynamic analysis of a compliant femoral artery bifurcation model using a fluid structure interaction framework. *Annals of biomedical engineering*, pp.36(11), pp. 1753-1763.

Larsson, E. et al., 2011. Analysis of aortic wall stress and rupture risk in patients with abdominal aortic aneurysm with a gender perspective. *J. Vasc. Surg.*, pp.54(2):295-299.

Leung, J.H. et al., 2006. Fluid structure interaction of patient specific abdominal aortic aneurysms: a comparison with solid stress models. *Biomedical engineering online*, p.5.

Limet, R., Sakalihassan, N. & Albert, A., 1991. Determination of the expansion rate and incidence of rupture of abdominal aortic aneurysms. *J. Vasc. Surg.*, pp.14(4):540-548.

Li, Z.Y. et al., 2008. Impact of calcification and intraluminal thrombus on the computed wall stresses of abdominal aortic aneurysm. *Impact of calcification and intraluminal thrombus on the computed wall stresses of abdominal aortic aneurysm.*, pp.7:928–935.

Lu, J., Zhou, X. & Raghavan, M.L., 2007. Inverse elastostatic stress analysis in pre-deformed biological structures: demonstration using abdominal aortic aneurysms. *J. Biomech.*, pp.40:693-696.

Maier, A. et al., 2010. A comparison of diameter, wall stress, and rupture potential index for abdominal aortic aneurysm rupture risk prediction. *Ann. Biomed. Eng.*, pp.38: 3124-3134.

Martufi, G. et al., 2009. Three-dimensional geometrical characterization of abdominal aortic aneurysms: image-based wall thickness distribution. *ASME J. Biomech.*, pp.131(6): 061015.

McGloughlin, T.M. & Doyle, B.J., 2010. New approaches to abdominal aortic aneurysm rupture risk assessment: engineering insights with clinical gain. *Arterioscler Thromb Vasc Biol*, pp.30(9), pp. 1687-1694.

Mizowaki, T., Sueyoshi, E., Sakamoto, I. & Uetani, M., 2009. Expansion rate of nonaneurysmatic abdominal aorta: over 10 years of follow-up CT studies. *Comput Med Imaging Graph*, pp.33(1), pp. 17-22.

Mower, W.R., Baraff, L.J. & Sneyd, J., 1993. Stress Distributions in Vascular Aneurysms - Factors Affecting Risk of Aneurysm Rupture. *Journal of Surgical Research, 55(2)*, pp.pp. 155-161.

Mower, W.R., Quiñones, W.J. & Gambhir, S.S., 1997. Effect of intraluminal thrombus on abdominal aortic aneurysm wall stress. *J. Vasc. Surg.*, pp.26:602–608.

Nagashima, H. et al., 2004. Matrix metalloproteinase 2 is suppressed by trapidil, a CD40-CD40 ligand pathway inhibitor, in human abdominal aortic aneurysm wall. *J Vasc Surg*, pp.39(2), pp. 447-453.

Newman, A.B. et al., 2001. Cardiovascular disease and mortality in older adults with small abdominal aortic aneurysms detected by ultrasonography: the cardiovascular health study. *Ann. Intern. Med*, pp.134(3):182-190.

Nissen, R.G., Cardinale, G.J. & Udenfriend, S., 1978. Increased turnover of arterial collagen in hypertensive rats. *Proc. Natl. Acad. Sci.*, pp.75:451–453.

Norman, P.E..K.J.e.a., Norman, P.E., Jamrozik, K. & et al., 2004. Population based randomised controlled trial on impact of screening on mortality from abdominal aortic aneurysm. *Bmj*, pp.329(7477): 1259.

Nyilas, R.D., N.S.M.L, Leung, J. & Xu, X.Y., 2005. Towards a new geometric approach to access the risk of rupture of abdominal aortic aneurysms using patient specific modeling. *Summer Bioengineering ConferenceVail, CO.*.

O´Leary, S.A. et al., 2014. The biaxial mechanical behaviour of abdominal aortic aneurysm intraluminal thrombus: Classification of morphology and the determination of layer and region specific properties. *J. Biomech.*, pp.47:1430–1437.

Ogata, T. et al., 2005. The lifetime prevalence of abdominal aortic aneurysms among siblings of aneurysm patients is eightfold higher than among siblings of spouses: an analysis of 187 aneurysm families in Nova Scotia, Canada. *J Vasc Surg*, pp.42(5), pp. 891-897.

Papaharilaou, Y., Ekaterinaris, J.A., Manousaki, E. & Katsamouris, A.N., 2007. A decoupled fluid structure approach for estimating wall stress in abdominal aortic aneurysms. *J Biomech*, pp.40(2), pp. 367-377.

Pappu, S., Dardik, A., Tagare, H. & Gusberg, R.J., 2008. Beyond fusiform and saccular: a novel quantitative tortuosity index may help classify aneurysm shape and predict aneurysm rupture potential. *Ann Vasc Surg*, pp.22(1), pp. 88-97.

Parr, A. et al., 2011. Thrombus volume is associated with cardiovascular events and aneurysm growth in patients who have abdominal aortic aneurysms. *J. Vasc. Surg*, pp.53:28–35.

Polzer , S., Gasser, T.C., Swedenborg, J. & Bursa, J., 2011. The impact of intraluminal thrombus failure on the mechanical stress in the wall of abdominal aortic aneurysms. *Eur. J. Vasc. Endovasc. Surg. Off.*, pp.41:467–473.

Polzer, S. et al., 2012. Impact of poroelasticity of intraluminal thrombus on wall stress of abdominal aortic aneurysms. *BioMedical Enginnering Online*.

Powell, J.T. et al., 2007. Final 12-year follow-up of surgery versus surveillance in the UK Small Aneurysm Trial. *Br. J. Surg.*, pp.94: 702–708.

Raghavan, M.L., Baoshun, M.A. & Filinger, M.F., 2006. Non-invasive determination of zero-pressure geometry of arterial aneurysms. *Ann. Biomed. Eng.*, pp.34(9):1414-1419.

Raghavan, M.L. et al., 2006. Regional distribution of wall thickness and failure properties of human abdominal aortic aneurysm. *J Biomech.*, pp.39:3010-3016.

Raghavan, M.L., Ma, B & Habraugh, R.E., 2005. Quantified aneurysm shape and rupture risk. *J Neurosurg*, pp.102(2), pp. 355-362.

Raghavan, M.L. & Vorp, D.A., 2000. Toward a biomechanical tool to evaluate rupture potential of abdominal aortic aneurysm: identification of a finite strain constitutive model and evaluation of its applicability. *J. Biomech.*, pp.33(4): 475-482.

Raghavan, M.L., Webster, M.W. & Vorp, D.A., 1996. Ex vivo biomechanical behavior of abdominal aortic aneurysm: assessment using a new mathematical model. *Annals of Biomedical Engineering*, pp.24, 573-582.

Raut, S.S., Chandra, S., Shum, J. & Finol, E., 2013a. The role of geometric and biomechanical factors in abdominal aortic aneurysm rupture risk assessment. *Ann. Biomed. Eng*, pp.1:1459–1477.

Raut, S. et al., 2013b. Biological, Geometric and Biomechanical Factors Influencing Abdominal Aortic Aneurysm Rupture Risk: a Comprehensive Review. *Bentham Science Publishers*, pp.44-59.

Reeps, C. et al., 2008. Increased 18F-fluorodeoxyglucose uptake in abdominal aortic aneurysms in positron emission/computed tomography is associated with inflammation, aortic wall instability, and acute symptoms. *J Vasc Surg, 48(2)*, pp.pp. 417-423; discussion 424.

Rissland, P., Alemu, Y., Ricotta, J. & Blustein, D., 2009. Abdominal aortic aneurysm rysk of rupture: patient-specific FSI simulations using anisotropic model. *ASME J. Biomech.*, pp.131(3):031001.

Riveros, F. et al., 2012. A pull-back algorithm to determine the unloaded vascular geometry in anisotropic hyperelastic AAA passive mechanics. *Ann. Biomed. Eng.*, pp.41:694–708.

Rodriguez, J.F., Martufi, G., Doblare, M. & Finol, E.A., 2009. The effect of material model formulation in the stress analysis of abdominal aortic aneurysms. *Ann Biomed Eng.*, pp.37(11):2218-2221.

Rodriguez, J.F., Ruiz, C., Doblaré, M. & Holzapfel, G., 2008. Mechanical stesses in abdominal aortic aneurysms: influence of diameter, asymmetry, and material anisotropy. *ASME J. Biomech.*, pp.130(2):021023.

Sakalihasan, N., Limet, R. & Defawe, O.D., 2005. Abdominal aortic aneurysm. *Lancet.*, pp.365:1577–1589.

Sakalihasan, N. et al., 2002. Positron emission tomography (PET) evaluation of abdominal aortic aneurysm (AAA). *Eur J Vasc Endovasc Surg, 23(5)*, pp.pp. 431-436.

Samarth, S.R. et al., 2013. Biological, Geometric and Biomechanical Factors Influencing Abdominal Aortic Aneurysm Rupture Risk: a Comprehensive Review. *Bentham Science Publishers*, pp.3, 44-59.

Saratzis, A. et al., 2011. Abdominal aortic aneurysm: a review of the genetic basis. *Angiology*, pp.62(1), pp. 18-32.

Scotti, C.M. & Finol, E.A., 2007. Compliant biomechanics of abdominal aortic aneurysms: A fluid-structure interaction study. *Computers & Structures*, pp.85(11-14), pp. 1097-1113.

Scotti, C.M., Jimenez, J., Muluk, S.C. & Finol, E.A., 2008. Wall stress and flow dynamics in abdominal aortic aneurysms: finite element analysis vs. fluid-structure interaction. *Computer methods in biomechanics and biomedical engineering*, pp.11(3), pp. 301-322.

Scotti, C.M., Shkolnik, A.D., Muluk, S.C. & Finol, E.A., 2005. Fluid-structure interaction in abdominal aortic aneurysms: effects of asymmetry and wall thickness. *Biomedical engineering online*, pp.4, p. 64.

Senior, R.M., Griffin, G.L. & Mecham, R.P., 1980. Chemotactic activity of elastin-derived peptides. *The Journal of clinical investigation*, pp.66(4), pp. 859-862.

Shibamura, H. et al., 2004. Genome scan for familial abdominal aortic aneurysm using sex and family history as covariates suggests genetic heterogeneity and identifies linkage to chromosome 19q13. *Circulation*, pp.109(17), pp. 2103-2108.

Shield, R.T., 1967. Inverse Deformation Results in Finite Elasticity. *Z. angew. Math. Phys.*, pp.78: 490-500.

Shum, J. et al., 2010. Semi-automatic vessel wall detection and quantification of wall thickness in computed tomography images of human abdominal aortic aneurysms. *Med. Phys.*, pp.37(2): 638-648.

Shum, J. et al., 2011a. Quantitative assessment of abdominal aortic aneurysm geometry. *Ann. Biomed. Eng.*, pp.39(1): 277-286.

Shum, J., Xu, A., Chatnuntawech, I. & Finol, E.A., 2011b. A Framework for the Automatic Generation of Surface Topologies for Abdominal Aortic Aneurysm Models. *Ann. Biomed. Eng*, pp.39(1):249-259.

Silence , J., Collen, D. & Lijnen, H.R., 2002. Reduced atherosclerotic plaque but enhanced aneurysm formation in mice with inactivation of the tissue inhibitor of metalloproteinase-1 (TIMP-1) gene. *Circ Res*, pp.90(8), pp. 897-903.

Siwik, D.A., Pagano, P.J. & Colucci, W.S., 2001. Oxidative stress regulates collagen synthesis and matrix metalloproteinase activity in cardiac fibroblasts. *American journal of physiology. Cell physiology*, pp.280(1), pp. C53-60.

Smith, A., 2000. The folding of the human brain: From shape to function. *London: Guy´s, Kings and St Thomas´School of Medicine*.

Solberg, S., Forsdahl, S.H., Singh, K. & Jacobsen, B.K., 2010. Diameter of the infrarenal aorta as a risk factor for abdominal aortic aneurysm: the Tromso Study 1994-2001. *Eur J Vasc Endovasc Surg*, pp.39(3), pp. 280-284.

Speelman, L. et al., 2009. Initial stress and nonlinear material behavior in patient-specific AAA wall stress analysis. *J Biomech.*, pp.42(11):1713-1719.

Speelman, L. et al., 2010. The mechanical role of thrombus on the growth rate of an abdominal aortic aneurysm. *J. Vasc. Surg.*, pp.51:19–26.

Stenbaek, J., Kalin, B. & Swedenborg, J., 2000. Growth of thrombus may be a better predictor of rupture than diameter in patients with abdominal aortic aneurysms. *Eur. J. Vasc. Endovasc. Surg. Off. J. Eur. Soc. Vasc. Surg.*, pp.20:466–469.

Stringfellow, M.M., Lawrence, P.F. & Stringfellow, R.G., 1987. The influence of aorta-aneurysm geometry upon stress in the aneurysm wall. *The Journal of surgical research*, pp.42(4), pp. 425-433.

Summer, D.S., Hokanson, D.E. & Strandness, D.E., 1970. Stress-strain characteristics and colagen-elastin content of abdominal aortic aneurysms. *Surgery Gynecology and Obstetrics*, pp.130, 459-466.

Swanson, R.J., Littooy, F.N., Hunt, T.K. & Stoney, R.J., 1980. Laparotomy as a Precipitating Factor in the Rupture of Intra-Abdominal Aneurysms. *Archives of Surgery*, pp.115(3), pp. 299-304.

Thompson, S.G. et al., 2009. Screening men for abdominal aortic aneurysm: 10 year mortality and cost effectiveness results from the randomised Multicentre Aneurysm Screening Study. *Brit. Med. J.*, pp.338: b2307.

Thompson, M. & Cockerill, G., 2006. Matrix metalloproteinase-2: the forgotten enzyme in aneurysm pathogenesis. *Annals of the New York Academy of Sciences*, pp.1085, pp. 170-174.

Thubrikar, M.J., al-Soudi, J. & Robicsek, F., 2001. Wall stress studies of abdominal aortic aneurysm in a clinical model. *Ann. Vasc. Surg.*, pp.15(3):355-366.

Thubrikar, M.J. et al., 2003. Effect of thrombus on abdominal aortic aneurysm wall dilation and stress. *J. Cardiovasc. Surg. (Torino)*, pp.44:67–77.

Tierney, A.P., Callanan, A. & McGloughlin, T.M., 2012. Use of Regional Mechanical Properties of Abdominal Aortic Aneurysms to Advance Finite Element Modeling of Rupture Risk. *J. Endovasc. Ther.*, pp.19:100–114.

Truijers, M. et al., 2007. Wall stress analysis in small asymptomatic, symptomatic and ruptured abdominal aortic aneurysms. *Eur. J. Vasc. Endovasc. Surg.*, pp.33(4):401-407.

Vande Geest, J.P., Sacks, M.S. & Vorp, D.A., 2006a. A planar biaxial constitutive relation for the luminal layer of intra-luminal thrombus in abdominal aortic aneurysms. *J. Biomech.*, pp.39:2347–2354.

Vande Geest, J.P., Sacks, M.S. & Vorp, D.A., 2006b. The effects of aneurysm on the biaxial mechanical behavior of human abdominal aorta. *J. Biomech.*, pp.39 (7):1324-1334.

Vardulaki, K.A. et al., 2000. Quantifying the risks of hypertension, age, sex and smoking in patients with abdominal aortic aneurysm. *British Journal of Surgery*, pp.87(2): p. 195-200.

Venkatasubramaniam, A.K. et al., 2004. A Comparative Study of Aortic Wall Stress Using Finite Element Analysis for Rupture and Non-Ruptured Abdominal Aortic Aneurysms. *Eur. J. Vasc. Endovasc. Surg.*, pp.28:168-176.

Vilata, G., Vaquero, N.F. & Vilata, J.A., 2010. Quantitative indicator of abdominal aortic aneurysm rupture risk based on its geometric parameter parameters. *World Academy of Science, Engineering and Technology*, pp.(69), pp. 181-185.

Vorp, D.A., 2007. Biomechanics of abdominal aortic aneurysm. *Journal of Biomechanics*, pp.40, 1887-1902.

Vorp, D.A. et al., 2001. Association of intraluminal thrombus in abdominal aortic aneurysm with local hypoxia and wall weakening. *J. Vasc. Surg.*, pp.34:291–299.

Vorp, D.A., Raghavan, M.L. & Webster, M.W., 1998. Mechanical wall stress in abdominal aortic aneurysm: Influence of diameter and asymmetry. *J. Vasc. Surg.*, pp.27:632-639.

Vorp, D.A., Rajagopal, K.R., Smolinski, P.J. & Borovetz, H.S., 1995. Identification of elastic properties of homogeneous, orthotropic vascular segments in distension. *Journal of Biomechanics*, pp.28 (5),501–512.

Wang, D.H.J., Makaroun, M., Webster, M.W. & Vorp, D.A., 2001. Mechanical Properties and Microstructure of Intraluminal Thrombus From Abdominal Aortic Aneurysm. *J. Biomech. Eng.*, pp.123:536–539.

Wang, D.H.J., Makaroun, M.S., Webster, M.W. & Vorp, , 2002. Effect of intraluminal thrombus on wall stress in patient-specific models of abdominal aortic aneurysm. *J. Vasc. Surg.*, pp.36:598–604.

Wanhainen, A. et al., 2005. Risk factors associated with abdominal aortic aneurysm: a population-based study with historical and current data. *J Vasc Surg*, pp.41(3), pp. 390-396.

Wassef, M. et al., 2001. Pathogenesis of abdominal aortic aneurysms: a multidisciplinary research program supported by the National Heart, Lung, and Blood Institute. *J Vasc Surg*, pp.34(4), pp. 730-738.

Wiernicki, I. et al., 2010. Haptoglobin 2-1 phenotype predicts rapid growth of abdominal aortic aneurysms. *J Vasc Surg.*.

Xenos, M. et al., 2010. Patient-based abdominal aortic aneurysm rupture risk prediction with fluid structure interaction modeling. *Annals of biomedical engineering*, pp.38(11), pp. 3323-3337.

Xu, X.Y. et al., 2010. High levels of 18F-FDG uptake in aortic aneurysm wall are associated with high wall stress. *Eur J Vasc Endovasc Surg*, pp.39(3), pp. 295-301.